2018-06-27

Computational Insights into the Structures, Mechanisms, and Chemical Properties of Metal Complexes, Enzymes, and Bio-molecules

Thomas Paul
University of Miami, smallzphd@gmail.com

Recommended Citation

Paul, Thomas, "Computational Insights into the Structures, Mechanisms, and Chemical Properties of Metal Complexes, Enzymes, and Bio-molecules" (2018). *Open Access Dissertations*. 2114.
https://scholarlyrepository.miami.edu/oa_dissertations/2114

UNIVERSITY OF MIAMI

COMPUTATIONAL INSIGHTS INTO THE STRUCTURES, MECHANISMS, AND CHEMICAL PROPERTIES OF METAL COMPLEXES, ENZYMES, AND BIO-MOLECULES

By

Thomas J. Paul

A DISSERTATION

Submitted to the Faculty
of the University of Miami
in partial fulfillment of the requirements for
the degree of Doctor of Philosophy

Coral Gables, Florida

August 2018

UNIVERSITY OF MIAMI

A dissertation submitted in partial fulfillment of
the requirements for the degree of
Doctor of Philosophy

COMPUTATIONAL INSIGHTS INTO THE STRUCTURES, MECHANISMS, AND CHEMICAL PROPERTIES OF METAL COMPLEXES, ENZYMES, AND BIO-MOLECULES

Thomas J. Paul

Approved:

____
Rajeev Prabhakar, Ph.D.
Professor of Chemistry

____
Francisco M. Raymo, Ph.D.
Professor of Chemistry

____
Orlando Acevedo, Ph.D.
Associate Professor of Chemistry

____
Guillermo Prado, Ph.D.
Dean of the Graduate School

____
John Reilly, Ph.D.
Associate Professor and Chair of Chemistry
Florida Gulf Coast University

PAUL, THOMAS J. (Ph.D., Chemistry)
Computational Insights into the Structures, Mechanisms, and Chemical Properties of Metal Complexes, Enzymes, and Bio-molecules (August 2018)

Abstract of a dissertation at the University of Miami.

Dissertation supervised by Professor Rajeev Prabhakar.
No. of pages in text. (137)

In this thesis, we have focus on the following three projects: (1) the inhibition of amyloid beta aggregation, (2) structural and mechanical properties of amyloid peptides, and (3) complex biological systems of molecular recognition pertaining to hydrolysis. In the first project, we have looked at the inhibition of early and late forms of Aß peptides using heparin derived disaccharides, small molecules, and a Rhenium centered photoluminescence probe. We have determined and characterized the most relevant binding sites of these complexes to both the monomeric and fibrillar forms of the Aß peptide. Currently, the aggregation of biomolecules has been implicated in a large number of neurological diseases. Furthermore, we have been able to develop models of larger Aß aggregates that clearly represent mature fibril structures based on mechanical property measurements. Our results were compared to experimentally determined values and were found to be in excellent agreement. Lastly, three complex systems of hydrolysis were investigated. Among them, the three transient species associated with the mechanistic cycle of GpdQ were determined as well as the effect of primary and secondary shell residues on the active site conformations. Additionally, binding sites on human serum albumin were identified and characterized based on experimental mass-

spec data for ZrK, and the effect of the addition of an ATCUN binding domain on the antimicrobial peptide (Buforin) and its binding to DNA was investigated.

Dedicated to my family; Rachel, Embry, and Theo you allowed me to follow my dream and supported me through it all. No words can describe how much I love you.

ACKNOWLEDGEMENTS

I am deeply grateful for all of the love and support that I have received from the people at the University of Miami, especially the department of chemistry. First, I would like to thank and extend my sincerest gratitude to my advisor, Dr. Rajeev Prabhakar. Without his help and guidance, I feel I would have never made it to the end. His constant motivation and support were paramount in my success here. Under his guidance, I have had the opportunity to learn a completely new and foreign section of chemistry, computational chemistry, where I was able to study complex biological systems that really challenged me. He encouraged me to meet problems head on and gave me the freedom to grow as an independent scientist. His friendliness and approachable demeanor made my five years in the program enjoyable and quick. Thank you for believing in me.

I would also like to thank Dr. Francisco Raymo and Dr. Orlando Acevedo for being on my committee. They have provided valuable insight into my research projects and have given me new ideas to progress them. I would also like to thank Dr. Burjor Captain for all of the help and guidance you have provided me throughout my five years. I would also like to thank Dr. Angel Marti, Dr. Igor Lednev, Dr. Alfredo Angeles-Boza, Dr. Gerhard Schenk, Dr. Tatjana Parac-Vogt, Dr. Alexander Shekhtman, and Dr. Vamsi Yadavalli and their group members for their valuable collaborations. We have published many great papers together in well-known journals. I also would like to thank Dr. Tegan Eve for his mentorship and help during my teaching assistantship. I really enjoyed teaching and feel I matured as an instructor, which was returned to me in the way of three consecutive “best teaching assistant” awards. Last but not least, I would like to thank Dr. John Reilly, my undergraduate advisor, who saw something in me even when I did not.

By working in your research lab my future path became clear and accessible. I could not have come this far without your help and mentorship.

I would like to thank my lab mates past and present, Mehmet Ozbil, Tingting Zhang, Zach Hoffmann, Gaurav Sharma, Vindi Mahesha, and Qiaoyu Hu (Joy) for all of their help. We have shared more time within the same place as anyone else I know. Thank you for the insightful conversations, cooperation, and support which I will never forget.

Finally, I would like to extend my sincerest gratitude and admiration to my family, which grew after coming here. Rachel you are my heart and soul, without your support none of this would have been possible. Words alone cannot describe the love and debt I owe you, but I look forward to the years it will take to pay you back. To my boys, Embry and Theo, you are my motivation for everything. Everything I do and have done is to prove to you that I am a worthy father. Thank you for letting me be your Dad.

“If I have seen further than others, it is by standing upon the shoulders of giants.”

- **Sir Isaac Newton**

TABLE OF CONTENTS

Page

LIST OF FIGURES

LIST OF TABLES

Chapter 1. Introduction

Alzheimer's disease (AD) is a neurological disorder that affects more than 5 million Americans. Furthermore, the amount of people developing this disease has steadily increased, placing great strain on our already weakened healthcare system. On average, in the United States, a person develops AD every 67 seconds.[1] To date the actual cause of the disease is not well understood, but strides are being made in this area of research. This deadly disease is characterized by the accumulation of amyloid plaques and fibrils in the brain.[1] The major components of amyloid plaques are individual peptide sequences consisting of 40-42 amino acids (Aβ) produced from the cleavage of the amyloid precursor protein (APP).[2-3] This task is completed by two specialized enzymes β-site APP-cleaving enzyme-1 (BACE1) which cleaves the C-terminus fragment and γ-secretase which subsequently cleaves the fragment produced from BACE1.[4] After cleavage, the Aβ40-42 peptides tend to aggregate forming fibrils and later plaques within the brain.[5] Therefore, one main area of interest in treating AD is the development of the therapeutic approaches that can decrease the amount of Aβ40-42 peptides that are naturally produced.

For the inhibition of the fibril formation, this task could be accomplished by employing low molecular weight (LMW) glycoaminoglycans (GAGs) such as enoxaparin, which have been shown to reduce Aβ load within the brain.[4] The natural form of heparin, a linear sulfated polysaccharide chain, can potentially disrupt the production of Aβ peptides.[5] Heparin does have the potential to disrupt β-secretase processing of APP and was first reported to do so by Leveugle et al. in 2007.[6-7] However, in recent studies levels of BACE1 in cell cultures have been shown to decrease rather than the functioning of either specialized enzyme.[4] In contrast, Scholefield et al. reported that a more highly sulfated analog of heparin (HS) like GAGs can inhibit BACE1 activity and further decrease the production of Aβ peptides within cell cultures.[8] GAGs may regulate APP processing by β-secretase and may enhance Aβ fibrillogenesis, but also might prevent the persistence of toxic forms of Aβ oligomers by blocking the cell surface so repeating units cannot further oligomerize.[5]

Within Aβ40-42 peptides, charged amino acid residues between region 1-11 are critical for Aβ pro-inflammatory response.[5, 9-11] Therefore, inhibiting the activity within this region could be useful in slowing the progress AD. In binding to this site, heparin can prevent more than 70% of Aβ peptide binding to heparan sulfated proteoglycans (HSPG) and may also block cell surface adhesion of Aβ monomer units.[5, 9, 12-14] Both effects could protect neurons and vascular endothelial cells against the toxic effects of Aβ aggregation.[5, 9, 13-14] It has also been demonstrated that GAGs significantly attenuate the toxic effect of Aβ on neuronal PC12 cells.[15-17] In addition, GAG association with Aβ may prevent further aggregation or induce a different kind of aggregation altogether.[5, 9, 15] Furthermore, GAGs might cover the aggregate form of Aβ so that it cannot interact efficiently within cells to produce a toxic response.[5, 9, 15-18] Heparin and its sulfated forms are a candidate for such a therapeutic treatment.[5, 9, 12-17] Another potential therapeutic treatment using small molecule has gained much interest in recent years.[19-21] These small molecules are capable of targeting and modulating the reactivities of Aß.[22] Among them, L2-B (N^1, N^1 –dimethyl-N^4-(pyridine-2-ylmethyl)benzene-1,4-diamine) was recently developed by the Lim lab and was shown to regulate metal-Aß species, along with antioxidant activity, and its efficacy both *in vivo* and *in vitro* has been demonstrated.[22] However, it has not been determined how molecular formulas and properties effect the reactivity and binding to the Aß surface. Therefore, the elucidation of these binding events is advantageous to scientists within this field of study. Additionally, looking at in from the opposite perspective, must effort has been made to determine the mechanical properties of such molecules and to exploit them for novel biomaterial applications. These studies have shown that a biomolecule that has been labeled detrimental to human health could actually be used to improve our lives, highlighting the "Silver Lining" of these molecules.

Biomaterials are part of an exciting field of study that has grown steadily over the past 50 years and encompasses aspects of medicine[23], biology[24], chemistry[25-26], and materials science[27]. Their uses range from scaffolds used in growing cells[28] to bio-implants that regulate fertility in cattle[29]. In medical applications, biomaterials are rarely used as isolated materials, but are more commonly integrated into devices or implants that perform very specific tasks.[23] Amyloid beta (Aβ) peptides are promising biomolecules that are capable of forming various variety of materials under diverse conditions.[25-26, 30-33] Their stability,[34-35] biocompatibility,[36] accurate self-assembly,[37] and easy functionalization[38] provide an excellent set of material properties that can be exploited for the aforementioned applications.[39-40] Driven by intermolecular forces such as hydrogen bonds, electrostatic and hydrophobic interactions, and π-π stacking, they can self-assemble molecule by molecule to produce supramolecular architectures (fibrils). This process proceeds through the formation of a natively unfolded intermediate to produce energetically stable, highly ordered, and β-sheet-rich fibrils.[41] The fibrils possess characteristic morphologies (hollow cylinders, twisted, and flat ribbons) ~100 Å in diameter and have variable lengths up to several micrometers.[42-46, 25, 44]

The fibrils formed by small fragments of Aβ peptides possess high mechanical strength, elasticity, thermochemical stability, and self-healing.[26, 47-50] These properties compare very favorably to most proteinaceous and non-proteinaceous materials.[51] They are most likely related to their macromolecular nature and in particular, to the physical and chemical constraints imposed by the individual amino acid residues. However, due to their heterogeneity, high-resolution molecular structures of low molecular weight Aβ amyloid oligomers cannot be easily determined because they are non-crystalline solid materials which are not amenable to X-ray crystallography and liquid state NMR.[52-58] Additionally, due to the fast rate of aggregation, structural determination of the early aggregates by using these experimental techniques is extremely difficult. Despite the availability of a sizeable amount of data, there are no systematic studies to elucidate the roles of amino acid sequence and structure pertaining to the fundamental material properties such as great strength, sturdiness, and elasticity.

Structurally, amyloid fibrils are mostly polymorphic, and typically appear as unbranched filaments that are a few nanometers in diameter, reaching up to a micrometer in length.[26] In addition, mature fibril structures have been shown to consist of one or more protofibrils which can adopt morphologies that range from twisted rope like structures to flat tapes.[25, 59] X-ray diffraction studies indicate amyloidgenic fibrils have a common core-like structure consisting of a dense network of hydrogen bonds stabilizing an elongated stack of β-strands, which are perpendicular to the fibril axis.[60] Peptides of alternating hydrophilic and hydrophobic amino acid residues have a tendency to adopt a similar β-sheet core structure.[30, 61] Examples of peptides that adopt this morphology include: insulin, polyglutamine (polyQ), and β-lactoglobulin.[62]

Apart from their fundamental biological significance, amyloidgenic fibrils possess mechanical properties comparable to the most robust natural polymers (spider silk) and in some cases are comparable to the strongest known materials, such as steel.[25] Due to their mechanical rigidity and strength, amyloidgenic fibrils are extremely favorable for novel applications as biomaterials. Moreover, mechanical and structural properties which prove to be so damaging in amyloid diseases such as Alzheimer's, also make them attractive candidates for novel biomaterials. Currently, atomic force microscopy based indentation experiments can provide quantitative measurements of local elastic environments and also allow for the imaging of individual fibrils by applying forces that range from pico to nanonewtons.[63] Recent studies have shown Young's modulus values range from megapascals[64-65] to gigapasccals[25-26, 66], depending on the specific experimental conditions (experimental approach and specific loading conditions). However, there is a lack of qualitative mechanical characterization at the atomic scale and a large variation in the measured moduli.[63] Therefore, the model used to extract the mechanical properties of these fibrils must be validated by some other means. To this end, we propose a novel approach that utilizes a duel in-silico method that combines molecular dynamics and strain-stress tests to compare with experimentally calculated modulus using atomic force microscopy experiments. The interplay between theoretical and experimental groups can provide platforms for designing better and more accurate experimental parameters, where one could obtain a more finite value for the elastic moduli of these fibrils. An approach that utilizes a more realistic fibrous structure taking into consideration key mechanical material parameters such as, torsional modulus, bending rigidity, and Young's modulus.

Peptides and proteins have a variety of functions: as enzymes that accelerate vital chemical reactions, as regulatory molecules whose binding to other peptides or proteins inhibits or activates their function, as detectors of signals through binding of small molecules, peptides or proteins, and as selective channels that enable or facilitate transport through cellular membranes.[67] In all of these roles, peptides and/or proteins bind small molecules, nucleic acids, and other protein partners forming a transient complex through noncovalent interactions.[67] These interactions are often very specific in that a particular protein binds only to one or a few other molecules in the cell however, more recently, proteins have been identified that are more promiscuous and have the ability to bind a large range of substrate such as Glycerophosphodiesterase (GpdQ) and Human serum albumin (HSA). Consequently, detailed characterization of protein interactions with their binding partners is of paramount importance in a quantitative and integrative biology which aims to understand biological systems in terms of their molecular components. With the ultimate goal of characterize the thermodynamic and kinetic behavior of components of living systems in sufficient detail that the response of those systems to stimuli (natural substrates or drugs) can be modeled with sufficient accuracy that the behavior of the system may be predicted or modified as desired.[67]

Biological systems of hydrolysis, both peptide and phosphoester, have been studied in great detail within this thesis. Hydrolysis has been involved in a wide range of biological and industrial applications ranging from proteomics[68] to the production of free fatty acids.[69] In our body, peptide hydrolysis is achieved using specialized enzymes known as proteases (cleave peptide bonds of proteins and large peptides) or peptidases (break peptide bonds of short peptides). These enzymes constitute about 60% of all enzymes that are used today in textile, food, leather, paper, and ethanol production industries. [70] However, due to the inherent stability of proteins (peptide bonds are their linkage), the hydrolysis half-life for the uncatalyzed reaction is estimated to be between 350-600 years under physiological conditions.[71] Due to this kinetic inertness, peptide bond cleavage is a very challenging task where only a few reagents are able to catalyze this reaction.[72] Phosphoester hydrolysis is another process central to all life on Earth, as phosphodiester bonds make up the backbones of stands of nucleic acid. In DNA and RNA, the phosphodiester bond is the linkage between the 3' carbon atom of one sugar to the 5' carbon atom of another. One potential application of this cleaving technique would be the treatment of infectious diseases, both in animals and humans. All living organisms, including viruses and bacteria, carry DNA or RNA molecules. Catalysts that can cut DNA or RNA sequence specifically (targeting one particular phosphodiester bond over another) could in principle be used to attack viruses or bacteria without harming the host.

In this thesis, a plethora of computational techniques such as quantum mechanics (QM), quantum mechanics molecular mechanics (QM/MM), and molecular dynamics (MD) have been used to study the (i) inhibition of Aß aggregates, (ii) method development for mechanical property determination and characterization of Aß aggregates, and (iii) molecular recognition of three complex systems of hydrolysis. The systems of hydrolysis pertain to either peptide or phosphoester cleavage by a natural enzyme, synthetic metal complex, and a system that employs both.

Chapter 2. Background Information

Computer simulation techniques have become a very powerful instrument used to address the many-body problem in statistical physics, physical chemistry, and biophysics.[73] Although the theoretical description of very complex systems from the view point of statistical physics is well defined, paired with the detailed microscopic information obtained through experimentation, it is often only possible to study specific details of those systems using simulations. However, simulations need specific inputs parameters that characterize the whole system that are either determined through theoretical calculation or provided by experimental data. These simulations are often used both to solve theoretical models beyond certain approximations and to provide a hint to experimentalists for future investigation. In the case of large experimental groups or facilities it is often required to prove the potential outcome of a study using computer simulations. In this way, the field of computer simulations has developed into a very important branch of science, one that helps theorists and experimentalists to go beyond their inherent limitations.[73]

2.1. Molecular Dynamics Simulations

The traditional simulation methods can be divided into two classes of stochastic and deterministic simulations, which are largely covered by the Monte Carlo (MC) and molecular dynamics (MD) methods, respectively. MD methods are governed by the system's Hamiltonian and consequently, Hamilton's equations of motion are integrated to move particles to new positions and to get new velocities at those new positions. This is an advantage over MC simulations, since not only is the configuration space sampled but the whole phase space is as well, which gives additional dynamical information about the system. However, both methods are complementary in that they lead to the same averages of static quantities, given that the system under consideration is sampled at sufficiently long time lengths so that all points within a given space are statistically represented and the same statistical ensemble is used.[73]

$$\dot{p_i} = -\frac{\partial H}{\partial q_i} \quad , \quad \dot{q_i} = \frac{\partial H}{\partial p_i} \qquad (1)$$

MD simulations programs require three basic ingredients: (i) a model of the interactions between atoms, molecules, surfaces etc. is needed. It is often assumed that the particles of interest interact in a pairwise manor, which is considered exact for particles with fixed partial charges. This assumption greatly reduces the computational cost required to implement the model into a program. (ii) An integrator is needed, which propagates particle positions and velocities with respect to time (from t to $t + \delta t$). The time step δt has to been chosen properly to guarantee the stability of the integrator, i.e. there should be no drift in the system's energy. (iii) A statistical ensemble has to be chosen where the thermodynamics properties such as pressure, temperature, and the number of particles must be controlled. The typical choice of an ensemble is MD is the microcanonical ensemble (NVE), where the total number of particles, volume, and energy are conserved throughout the simulation, since the system's Hamiltonian without external potential is a conserved quantity. Nevertheless, there are other extensions to the Hamiltonian which allow for simulating different statistical ensembles such as NVT and NPT. Primarily the isothermal-isobaric ensemble (NPT) has been applied throughout my study which maintains a constant number of particles, pressure, and temperature. This ensemble plays an important role in chemistry as chemical reactions are usually carried out under constant pressure condition.[74] These steps define the MD simulation and with these in hand one can obtain exact results with numerical precision. However, these results are on correct when compared to theoretical predictions and experimental findings. If the simulation results differ greatly from the *real system* properties, the model must be refined. These initial parameters can come from either neutron diffraction measurements, NMR data, or from first principle investigations like quantum *ab initio* calculations or combinations of. This process can be understood as an adaptive refinement method which leads to an approximation of a model of the *real world* at least for certain properties.

2.2. Molecular Dynamics Time Scales

Microscopic simulations are limited by their accessible time- and length-scales coverable. With quantum simulation methods, based on the fast motions of electrons, typically in the picosecond range, MD simulations in the nanosecond range, and Brownian dynamics in the microsecond range, it is clear that the more detailed a simulation technique operates, the smaller is the accessibility of long time and length scales. Classical molecular dynamics approximates the electronic distributions in a rather coarse-grained approach by either fixing partial charges or by adding an approximate model for polarization effects. In both cases, the time scale is determined based on the intermolecular collisions, rotational motions, and intramolecular vibrations, which are orders of magnitude slower than electron motions.

Classical molecular dynamics methods are currently applied to a large class of problems, for example properties of liquids[75-78], defects in solids[79-80], surface properties[81-

[84], molecular clusters[85-87], polyelectrolytes[88-91], and biomolecules[92-101]. Due to this large area of application many different types of simulation code have been developed by many groups. Examples are AMBER/Sander[102-103], CHARMM[104], NAMD[105], GROMACS[106-109], and LAMMPS[110]. Within this thesis, all molecular dynamics simulations were carried out in GROMACS, utilizing either the GROMOS53a6[111] or AMBER03[112-113] force-fields.

2.3. Molecular Interactions in Molecular Dynamics and Force-Fields

Molecular dynamics simulations consist of the numerical, step-by-step, solution of the classical Newtonian equations of motion, which may be written

$$m_i r_i = f_i \qquad\qquad f_i = -\frac{\partial}{\partial r_i} U \qquad (2)$$

Firstly, we need to be able to calculate the forces f_i acting on the atoms, and these are usually derived from a potential energy $U(r^N)$, where $r^N = (r_1, r_2 \ldots . r_N)$ represents the complete set of 3N atomic coordinates. The part of the potential energy $U_{\text{non-bonded}}$ representing non-bonded interactions between atoms is traditionally split into 1-body, 2-body, and 3-body….terms:

$$U_{non-bonded}(r^N) = \sum_i u(r_i) + \sum_i \sum_{j>i} v(r_i, r_j) + \ldots\ldots \qquad (3)$$

The $u(r)$ term represents an external applied potential field or the effects of the container walls; which is usually dropped for fully periodic systems. Also, it is usual to concentrate on the pair potential and neglect three-body interactions. In most simulations, the simplest model that represents the essential physics within the system is a sufficient model. The most commonly used form is the Lennard-Jones potential, with two parameters: σ, the diameter, and ε, the well depth.

$$v^{LJ}(r) = 4\epsilon\left[(\frac{\sigma}{r})^{12} - (\frac{\sigma}{r})^{12}\right] \tag{4}$$

If electrostatic charges are present, the appropriate Coulomb potentials are added.

$$v^{Coulomb}(r) = \frac{Q_1Q_2}{4\pi\epsilon_0 r} \tag{5}$$

Where Q_1 and Q_2 are the charges and ε_0 is the permittivity of free space. The correct handlings of long-range forces are essential in many different types of molecular simulations. For molecules we must also consider intramolecular bonding, with the simplest terms as follows:

$$U_{intramolecular} = \frac{1}{2}\sum_{bonds} k_{ij}^{r}(r_{ij} - r_{eq})^2 \tag{6a}$$

$$+ \frac{1}{2}\sum_{bend\ angles} k_{ijk}^{\theta}\,(\theta_{ijk} - \theta_{eq})^2 \tag{6b}$$

$$+ \frac{1}{2}\sum_{torsion\ angles}\sum_{m} k_{ijkl}^{\emptyset,m}(1 + \cos(m\emptyset_{ijkl} - \gamma_m)) \tag{6c}$$

The bonds will typically involve the separation $r_{ij} = |r_i - r_j|$ between adjacent pairs of atoms in a molecular framework and is assumed to be harmonic in nature Eq. (6a) with a specified equilibrium separation. The bend angles are between successive bond vectors and therefore involve three atom coordinates. Usually the bend term is taken to be quadratic in the angular displacement from the equilibrium value and the torsion angles are defined in terms of three connecting bonds, hence the use of four coordinates as shown in Eq. (6c). A simulation package force-field will specify the precise form of Eq. (5) and the various strength parameters k and other constants therein. Many molecular mechanics force-fields, aimed at improving the prediction of structures and properties typically include many cross-terms (e.g. stretch-bend): MM3[114] and MM4[115] are examples. Quantum mechanical calculations may provide a platform to determine the "best" molecular force-field. Additionally, comparison of simulation results with thermophysical properties and vibration frequencies is invaluable in force-field development and refinement. A separate and more current family of force fields, such as AMBER[116], CHARMM[117] and OPLS[118] are geared more to larger molecules (proteins, polymers) in condensed phases; their functional form is simpler, closer to that of Eq. (5), and their parameters are typically determined by quantum chemical calculations combined with thermophysical and phase coexistence data.

2.3. Molecular Docking

Typically, the goals of molecular docking are to identify ligands that bind to a specific receptor or binding site and the identification of its preferred, energetically most favorable binding conformations. In order to accomplish this task, molecular docking tools can be used to generate a set of different ligand binding conformations which use a scoring function to estimate their binding affinities in order to determine the best binding mode. Autodock[119] uses a computationally inexpensive hybrid force-field that contains terms based on molecular mechanics as well empirical terms. The prediction of absolute binding energies may be less accurate compared to other approaches, purely force-field methods, however this semi-empirical approach is considered well-suited for the relative rankings. The Autodock semi-empirical force-field includes intramolecular terms, a desolvation model, and also considers directionality in hydrogen bonds. The conformational entropy is calculated as the sum of the torsional degrees of freedom which are user defined. Water molecules are not model explicitly, but pair-wise atomic terms are used to estimate the water's contribution (dispersion/repulsion, hydrogen bonding, electrostatics, etc.), where weights are added for calibration. Firstly, it calculates the energy of the ligand and receptor in the unbound state, then calculates the energy of the protein-ligand complex. The difference between the two is then taken as shown in Eq. (7).

$$\Delta G = (V_{bound}^{L-L} - V_{unbound}^{L-L}) + (V_{bound}^{P-P} - V_{unbound}^{P-P}) + (V_{bound}^{P-L} - V_{unbound}^{P-L} + \Delta S_{conf}) \quad (7)$$

Where *P* refers to the protein, *L* refers to the ligand, *V* is the pair-wise evaluations mentioned earlier and ΔS_{conf} denotes the loss of conformational entropy upon binding. [120]

2.4. Binding Free Energies Utilizing the Lambda Dynamics Approach

Free energy simulations are fundamental to understanding the thermodynamic properties of various biologically important phenomena[121-122] such as; estimation of hydration free energies of ions[123-124] and small molecules[125-126], protein-ligand affinities[127], and protein stability. [128-129] Drug potency is often correlated to binding affinities to a target receptor and the use of theoretical tools which can reliably estimate the binding free energy can facilitate the design of novel therapeutics.[128, 130-131] The difference in free energy between two states of a system can be determined using a coupling parameter approach in concert with a thermodynamic integration (TI) as shown in formula (8).

$$\Delta F_{AB} = \int_{\lambda_A}^{\lambda_B} \langle \frac{\partial H(\lambda)}{\partial \lambda} \rangle \, d\lambda' \tag{8}$$

In this approach, the Hamiltonian H is made a function of the coupling parameter, λ. The λ-dependence of the Hamiltonian defines the pathway that connects the two states A and B. To solve Eq (8), one needs to evaluate the ensemble average at a number of discrete λ-points by preforming separate simulations for each chosen λ. There are two types of nonbonded interactions that can be transformed during free energy calculations, namely, Coulombic and van der Waals interactions. However, special treatment must be used when turning off these interactions. First Coulombic terms are turned off prior to the van der Waals terms so that no oppositely-charged atoms will interact at very close distances which would result in unstable configurations and unreliable energies. Furthermore, using a thermodynamic cycle, the relative binding energies of two ligands can be described by the difference in free energy associated with the chemical change of one ligand into the other in the bound and solvated environments.[132] This approach has been described in more detail in previous works.[132-134]

2.5 Parameterizing Non-Standard Molecules for Molecular Dynamics

Many of the studies presented in this thesis required the parameterization of non-standard molecules before molecular dynamics could be performed. Typical force-fields have well defined parameters for amino acids (proteins) and nucleic acids (DNA). However, they fall short if you are interested in simulating something more exotic, such as metal complexes (polyxoxmetalate ZrK) or small molecules like L2-B (N^1,N^1-dimethyl-N^4-(pyrindin-2-ylmethyl)benzene-1,4-diamine)). Therefore, quantum chemistry techniques have to be exploited to calculate the parameters of these complex non-standard molecules. All bonded terms such as; bonds, angles, dihedrals (torsion angles), and impropers (out of plane bending) must be described as well as the charges per atom. When considering bonds two quantities are required, the length of the bond and the force constant associated with it. Similarly, to define angles, the angle between three atoms must be defined as well as a force constant. For dihedrals, six coefficients (C0-C5) reflect the degrees of freedom with respect to the principle dihedral angle while impropers are typically used to define planar regions within a molecule that are locked at 180^0 during the simulations. Additionally, non-bonded terms must be either taking for literature or calculated manually. The non-bounded terms (van der Waals and electrostatic) are typically described using 12-6 Lennard-Jones potentials (Eq. 4) and Coulombic potentials (Eq. 5), respectively. Non-bonded terms are the hardest to obtain (typically through quantum software), however currently there are published routes that give a good approximation of these terms.[135-136] An example is given below where I parameterize ZrK (polyoxometalate). The X-ray structure of ZrK after including a hydroxyl nucleophile was fully optimized without any geometrical constraint employing DFT functional B3LYP[28] and Lanl2dz[137] basis set as implemented in the Gaussian 09[138] program. It is noteworthy that ZrK and POMs in general are very complex molecules to treat using molecular mechanics. The RESP charges for ZrK were calculated and used to form a topology file using antechamber,[139-140] an in-built tool in AMBER.[141] The set of Lennard-Jones parameters for the W and O atoms of the ZrK framework were taken from previous works [142-143] while the parameters for Zr were taken from the UFF force field.[144] The ZrK metal cluster was treated as a semi-rigid body during the simulations where the oxygen and tungsten cage was held together using a matrix, a distance restrains with high energetic penalty (≥ 1000 kJ/mol), for conformational deviations.

Chapter 3: Inhibition of Amyloid Beta Aggregation

In this chapter inhibition of amyloid beta aggregation using glycoaminoglycans (GAGs), small drug like molecules (i.e. N^1,N^1-dimethyl-N^4-(pyrindin-2-ylmethyl)benzene-1,4-diamine)), and a photoluminescence metal probe $[Re(CO)_3(dppz)(Py)]^+$ will be discussed in detail. Combined molecular docking and molecular dynamics simulations have provided the platform to study the binding of these distinct molecules to the surface of both monomeric and fibril forms of the Aβ40 peptide. The inhibition of these early aggregates has been reported as a potential way of halting or prolonging the onset of neurological diseases such as Alzheimer's and Parkinson's.

3.1 Design of Heparin Based Molecules for the Inhibition of Aβ40 Aggregation

The development of heparin analogs for the treatment of Alzheimer's disease will require several key criteria to be met, such as; (1) the low molecular weight heparin analogs must be able to cross the brain barrier,[5-7] (2) possess high binding affinity for Aβ peptides,[4] (3) and provide specificity for binding to only certain proteins within a cell line.[4, 6-7] Thus, structural information regarding the exact binding sites on either monomer and/or fibril forms of Aβ40-42 peptides must be elucidated. Nurcombe et al. reported that the specificity of sulfated heparin for binding to fibroblast growth factor receptors is controlled primarily through its sulfation pattern.[145] However, it is not well understood how the amount of sulfated groups an orientation present on the GAGs will affect its binding. Furthermore, fine tuning the amount and orientation of the sulfated groups present could further provide specificity for binding.[5] With the wide variety of GAGs which possess different molecular weights, charge densities, degrees of saturation, and types of saccharide units, the amount of possible motifs are enormous.[5] However, structures of complexes between Aβ-GAGs and the information regarding the nature of the interactions are not available. In this study, we have combined molecular docking and molecular simulations techniques to study interactions of both monomeric and fibrilliar forms of Aβ40 with a variety of chemically distinct GAG molecules (Figures 3.1 and 3.7). Our results will help to develop novel low molecular weight GAG compounds that could be used as a therapeutic treatment for Alzheimer's disease.

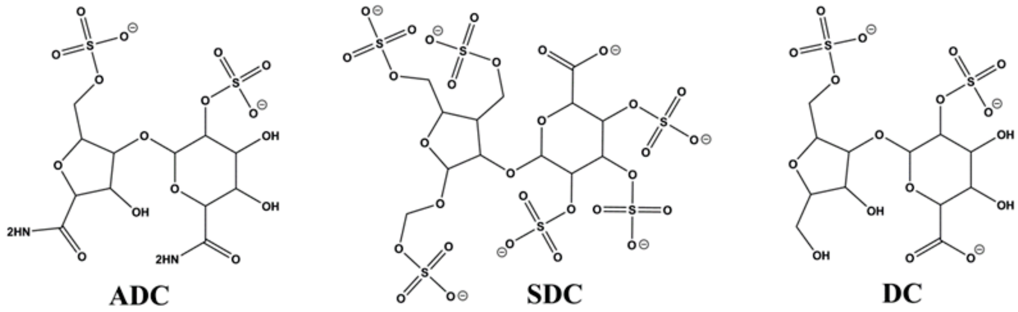
ADC **SDC** **DC**

Figure 3.1. Atomic representation of heparin analogues used within this study ADC, SDC, DC.

3.2. Docking of ADC, SDC, and DC to the Aβ40 Fibril and Monomer

Docking of ADC, SDC, DC to the Aβ40 fibril showed two major binding sites (A and B in figure 3.2). The first site (site A) was on the top of the fibril in the region of His14-Lys16. This binding site was generated by the interactions between the negatively charged sulfates attached to ADC, SDC, and DC and the positively charged amino acid residues on the fibril's surface. For example, the carboxylate and sulfate groups of both ADC and SDC formed hydrogen bonds with His14 and Lys16 residues of the Aβ40 fibril. Similar interactions were observed for DC, where it formed hydrogen bonding interactions with three Lys16 residues. Additionally, ADC, SDC, DC were found to bind to the side of the Aβ fibrils within the hairpin region (site B). Binding to this site has the potential to inhibit the aggregation of Aβ fibrils; therefore, this binding site has been specifically focused on in our studies. The presence of a bound heparin molecule could reduce the formation of oligomers by blocking the site of adhesion making it impossible for another monomer unit to bind, thus halting aggregation.

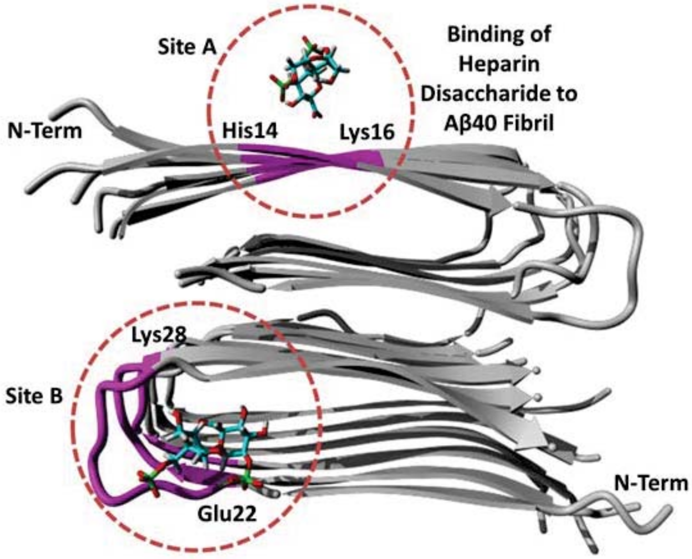

Figure 3.2. Docking results showing site A formed between residues His14-Lys16 and site B formed between Glu22-Lys28

Furthermore, ADC, SDC, DC were docked to the Aβ40 monomer in order to elucidate the possible binding interactions between the earliest stage of Aβ40 aggregation and our heparin analogues. All three analogues studied bind to the N-terminus region of the monomer and interact strongly with polar amino acid Arg5, as well as, neutral residue His6. The electrostatic potential map shown in Figure 3.3 shows a very large positively charge region (blue lobe) that could accommodate binding of these negatively charged species.

3.3. ADC Interactions with Both Monomeric and Fibril Forms of the Aβ40 Peptide

The ADC molecule shows binding to the N-terminus region of the Aβ40 monomer (Figure 3.4a), between residues Ala1 and His6.

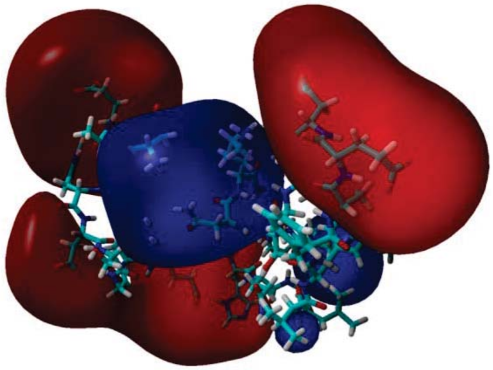

Figure 3.3. Electrostatic potential map of the Aβ40 monomer showing negatively charged regions in red and positive regions in blue.

Strong hydrogen bonding interactions between the sulfated group present on ADC and polar residues Asp1 and Arg5 at distances of 2.13 and 1.97 Å respectively were observed. Furthermore, His6 shows a hydrogen bonding interaction with the terminal amine of ADC at a distance of 1.77 Å. The binding energy computed for this complex was -18.4 kJ/mol, which indicates strong electrostatic and hydrophobic interactions (Table 3.1). MD simulations were also run with ADC binding to both A and B sites of the Aβ40 fibril (Figure 3.4b). Site A was stabilized by many hydrogen bonds originating from polar and charged amino acid residues His14 and Lys16, respectively. Moreover, ADC interacts through a host of hydrogen bonding interactions with polar residues located at site B (Glu22-Lys28) of the Aβ40 fibril. The amine present on ADC displays strong hydrogen bonding with the negatively charged oxygen of Glu22 at a distance of 2.23 Å.

Additionally, ADC interacts with multiple Lys28 residues on separate monomers within the fibril through hydrogen bonding (distances ≤ 2.5 Å). The binding energy calculated for this complex is -28.6 kJ/mol (Table 3.1), which is more negative (indicative of better binding or increased interactions) when compared to the binding of ADC to the peptide form.

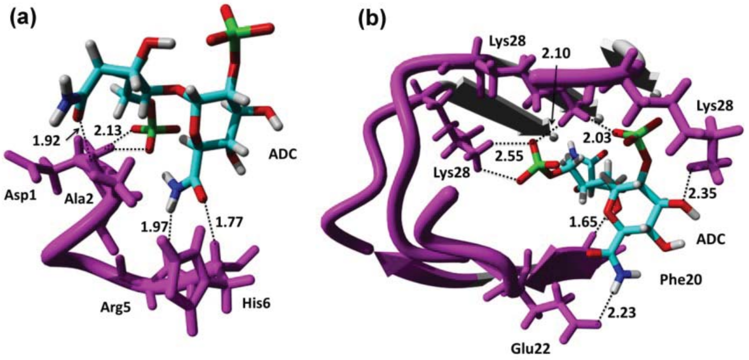

Figure 3.4. (a) ADC (amide disaccharide) binding to the monomer form of Aß40 peptide. (b) ADC binding to the fibril form of the Aß40 peptide. Zoomed views with residues and distances labeled.

3.4. SDC Interactions with Both Monomeric and Fibril Forms of the Aβ40 Peptide

The supersulfated form (SDC) of the heparin disaccharide interacts with the Aβ40 monomer through its N-terminus region as well. This result was not surprising when considering a less negative species ADC also interacted within the same region. The SDC is stabilized within this pocket by three electrostatic interactions with the NH_3 present (Asp1) at distances of 2.06, 2.35, 3.32 Å. Positive residue Arg5 also shows two strong hydrogen bonds with a sulfate group of SDC at distances of 2.30 and 2.44 Å. These strong interactions kept SDC in place over the course of the MD simulation. The binding energy calculated for this complex indicates stable binding energies within this site (-20.2 kJ/mol, Table 3.1). This is slightly better than the previous case with ADC. However, this trend was expected due to an increase in negative charge for the SDC with compared with the ADC (more sulfate groups were added).

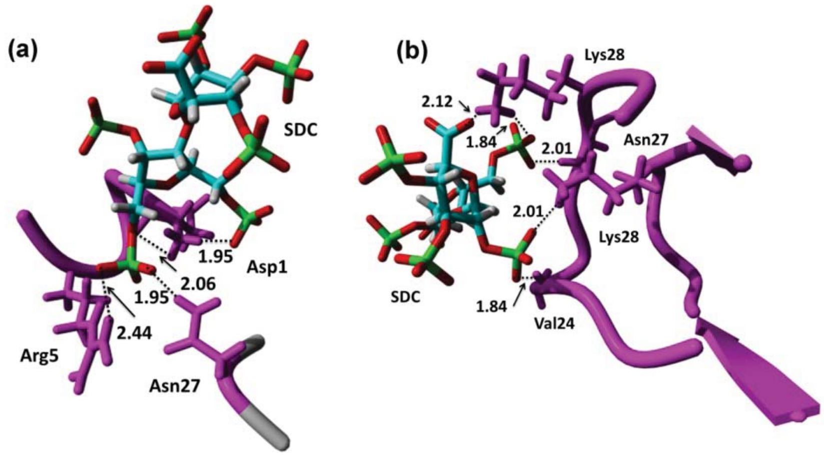

Figure 3.5. (a) SDC (super sulfated disaccharide) binding to the monomer form of Aß40 peptide. (b) ADC binding to the fibril form of the Aß40 peptide. Zoomed views with residues and distances labeled.

This increase in negative charge would cause the SDC to bind faster to the Aβ40 aggregate's surface. SDC also interacted strongly with both site A and B of the fibril (Figure 3.5b). MD simulations of site A reveal a large number of hydrogen bonding interactions originating from polar and charged amino acid residues His14 and Lys16, respectively. All hydrogen bonds are within 3.0 Å, which indicates moderate to strong hydrogen bonding between the fibril's surface and the sulfate groups present on SDC. Interestingly, only three of the six sulfate groups interact with the fibrils surface, most likely due to steric clashes or strain and electrostatic repulsion that would arise from the charged groups being too close together. For the site B, again there were multiple hydrogen bonding interactions that were responsible for the binding of the ligand to the fibril (Figure 3.5b). One sulfate group exhibited hydrogen bonding with Asn27 and Lys28. Another sulfate group interacted with Val24 and the Lys28 of the neighboring monomer at distances of 1.84 and 2.01, respectively. The carboxylate group present on SDC also interacted with Lys28 at a distance of 2.12 Å. The binding energy calculated for this complex indicates stable binding energies within this site (-28.8 kJ/mol, Table 3.1). Since inhibition of the generation of higher order Aβ40 oligomers has been proposed as one of the promising strategies to prevent AD, the interactions of only the fibril form have been investigated with the remaining GAG molecules.

3.5. DC Interactions with the Fibril Form of the Aβ40 Peptide

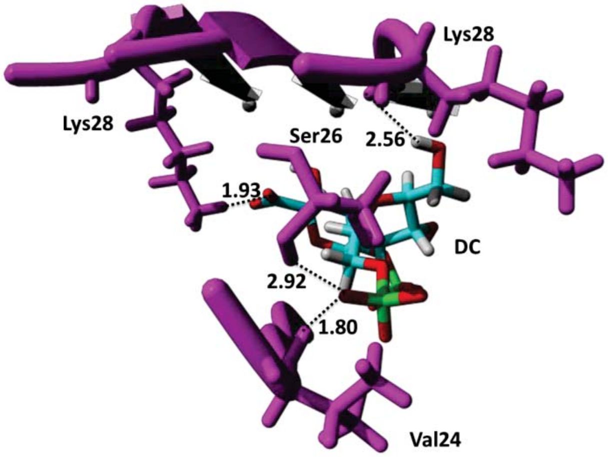

Figure 3.6. DC interacting with binding site B from Aß40 fibrils. Zoomed view of the hairpin region between residues Glu22-Lys28 of the Aß40 fibril.

At site A, the lysyl side chain of Lys16 of Aβ40 interacted with the negatively charged oxygen located within a sulfate group of DC. Interestingly, only one sulfate group present on DC was not interacting with the fibril. The binding pocket was further stabilized by His14, showing a strong hydrogen bond with a sulfate group at a distance of 1.96 Å. Furthermore, down the fibril, Lys16 associated with a hydroxyl present on the ring of the heparin analogue.

System	E_{elec}	$\Delta G_{desol\ A}$	$\Delta G_{desol\ B}$	ΔG_{elec}	$\Delta G_{nonpolar}$	$\Delta G_{binding}$
ADC + monomer	-48.2	12.4	25.3	-10.5	-7.9	-18.4
ADC + fibril	-81.0	34.8	39.7	-6.5	-15.9	-22.4
SDC + monomer	-74.2	36.4	26.0	-11.8	-8.4	-20.2
SDC + fibril	-103.7	43.6	40.2	-19.9	-8.9	-28.8
DC + fibril	-60.2	36.8	22.6	-1.0	-15.9	-16.9

Table 3.1. Shows the relative binding energies calculated with separate energy contributions determined. All energy values are shown in kJ/mol

In many of our simulations, binding to different sections of the fibril caused the DC molecule to shift up the top binding site. However, interactions at site B of the fibril remained intact throughout the simulation. At this site, DC exhibited several hydrogen bonding interactions as detailed in Figure 3.6. One sulfate group of DC interacted with Val24 and Ser26 residues in the hairpin region at distances of 1.80 and 2.00 Å, respectively. Additional interactions observed included hydrogen bonding between the carboxylate group of DC and a Lys28 residue and between a hydroxyl group of DC and another Lys28 residue. These strong hydrogen bonding interactions were sufficient to keep DC bound to this site over the course of a MD simulation. DC shows the weakest binding energy when comparing the three complexes studied, but was expected. With increasing negative charge present within the heparin analogues the binding energy also increases, this is not surprising as the negative charges of the heparin analogues would be attracted to the positively charged residues on the aggregates surface, whether on the side or tops of these fibrils. However, binding to the side of the fibrils surface could block the addition of more peptide units thereby restricting or modulating the aggregation of these critical peptides.

3.6. Variants (V1, V2, V3 and V4) and Their Interactions with Both Monomeric and Fibril Forms of the Aβ40 peptide

In addition to the three models described ADC, SDC, and DC, four more analogues were studied to see the effect of modifying the functional group present within our standard DC molecule. These four analogues are shown in Figure 3.7. In the first variant studied (V1), the hydroxyl functional groups were deprotonated while the carboxylic acid (COO^-) groups were protonated.

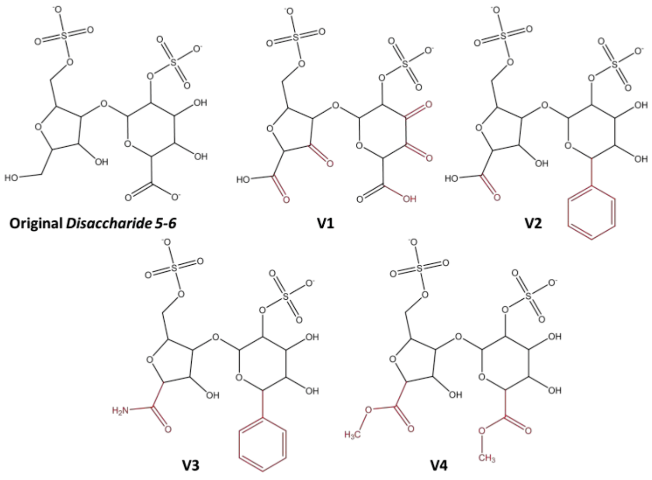

Figure 3.7. Structural models of DC variants V1-V4. Functional group substitutions are shown in red compared to DC.

The main reasons for the changes were to allow for more hydrogen bonding acceptors on the surface of V1 to try to increase the interaction with site B of the Aβ40 fibril. Furthermore, the protonated carboxylic acid groups could function as a molecular hook allowing for acceptor and donor hydrogen bonding interactions. However, V1 only interacted with the site A and would not bind to the site B of the fibril (5+ simulations). In the second variant (V2), one carboxylic acid group was substituted for an aromatic benzene ring to see if the addition of a hydrophobic group would help stabilize the site B.

Heparin Analogues	Site A	Site B
ADC	X	X
SDC	X	X
DC	X	X
V1	X	O
V2	O	O
V3	O	O
V4	O	O

Table 3.2. List of successful heparin analogue binding to the Aβ40 fibril. The “X” represents binding and the “O” represents no binding to that site.

This site could be stabilized by interacting with some of the hydrophobic residues hidden within the stacks of the Aβ40 fibrils. However, no binding to this site of the fibrils was observed, mostly due to the steric bulkiness of benzene group present on V2. In all of the simulations, V2 failed to stay bound to the site B but did bind to the site A. Interestingly, during the simulations of site A, V2 shifts to a more hydrophobic site on the top of the fibril closer to hydrophobic residues Val18 and Phe19. In the third variant (V3), the aromatic benzene was kept and a carboxylic acid group substituted for an amide group. Again, due to the bulkiness of the benzene ring, V3 binds only to a shifted site between residues Lys16-Phe19. In the last Variant studied V4, methoxy groups were added to the DC fame work to gain the hydrophobic binding benefit but loose the steric bulkiness of having a benzene ring. Again, as seen for V3, V4 binds to shifted site between residues

Lys16-Phe19 and did not bind to the site B of the Aβ40 fibril. Table 3.2 lists all successful hits obtained for the heparin analogues.

3.7. Summary and Conclusions

In this study, we have utilized molecular docking and MD simulations techniques to investigate interactions of both monomeric and aggregated forms of Aβ40 with a wide range of chemically diverse GAGs referred to as ADC, SDC, DC, V1, V2, V3 and V4 (Figure 3.1 and 3.7). GAGs such as heparin have been experimentally proposed to inhibit the generation of neurotoxic forms of amyloid oligomers. Our docking results predicted two major binding sites (A and B) on Aβ40 fibrils (Figure 3.2). Site A is located at the top of the fibril (His14-Lys16), while site B is present in the hairpin region (Glu22-Lys28). Since the letter lies along the axis of fibrils, it is an interesting target to design molecules to inhibit Aβ aggregation. It was found that ADC, SDC, and DC bind to both sites, while V1 bind to site A only and V2, V3, and V4 bind to a different site formed between residues Lys16-Phe19 (Table 3.2). These results suggested that ADC, SDC and DC can inhibit amyloid aggregation and lead to the development of molecules for the prevention of AD.

3.8. Development of Small Molecules Capable of Targeting and Modulating Aβ40

Small molecules capable of not only targeting but inhibiting amyloid beta aggregation have been examined as tools to probe the molecular level foundations of individual and inter-related features involve in neurological diseases.[22] Among them, L2-B (N^1,N^1-dimethyl-N^4-(pyrindin-2-ylmethyl)benzene-1,4-diamine; shown in Figure 3.8) was recently discovered to regulate metal-Aβ species, along with antioxidant activity and its *in vitro* and *in vivo* efficacy toward metal-Aβ has been demonstrated by Mi Hee Lim and coworkers.[146-147] However, up tell now, how the molecular formula and properties of such a tool and their effect on the specific reactivities for a desired target are not well understood. Therefore small molecules with common core features based on L2-B backbone (Figure 3.8) can be used to construct a viable chemical library of reactive analogues.

3.9. L2-B Docking to the 2-fold and 3-fold Aβ40 Fibril

Since there are no high resolution structures of the L2-b bound Aβ complex from either NMR or X-ray diffraction, the exact binding sites between the L2-b and the Aβ40 fibril are not known experimentally.

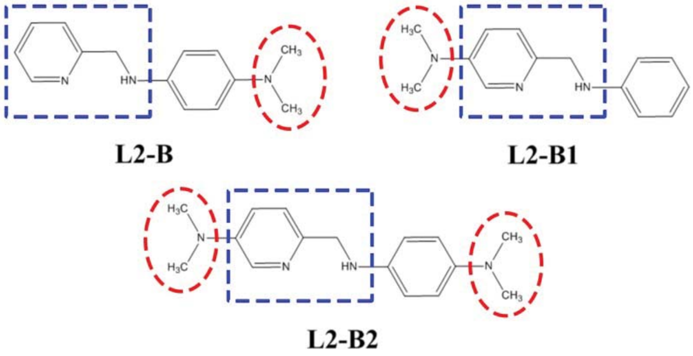

L2-B **L2-B1**

L2-B2

Figure 3.8. Small molecules inhibitors of Amyloid beta aggregation. The structural similarities are highlighted, Blue sections correspond to structural portion 1 and the red sections are structural portion 2

Computational approaches have become a powerful tool for studying protein−ligand interactions in recent years. In this study, we have utilized three different molecular docking techniques and MD simulations. The binding of the L2-b to Aβ1−40 fibril models with two-fold symmetry was investigated using (1) rigid docking, (2) flexible docking, and (3) rigid docking on different conformations of fibrils derived from short-term MD simulations, respectively. The last two approaches include flexibility of the receptor. The L2-b complex was docked onto the two-fold Aβ fibril, since the two-fold structure is the predominate conformation.

Binding Site	**Interacting Aβ40 Residues (two-fold)**
1+1`	Phe20, Glu22
2+2`	**Phe19, Asp23, Lys28**
3+3`	Glu11, His14
4+4`	Asn27, Val40
5+5`	Phe19, Phe20, Glu22
6+6`	Gly33, Met35

Table 3.3. List of binding sites for L2-B bound to the two-fold Aβ40 fibrils.

Due to the C2 symmetry of the two-fold fibril, it contains two similar binding sites on each side termed as X and X`. Firstly, the rigid docking on the fibrils provided 20 top ranked poses. The L2-b complex binds to the same site at both sides of the fibril termed as 1 and 1` and in seven of the 20 poses (Figure 3.9 and Table 3.3). Both the hydrophobic residue Phe20 and the hydrophilic residue Glu22 of the Aβ fibril interact with the L2-b complex in this site. Moreover, among the seven poses obtained the L2-b complex binds to site 1 in five poses and to site 1` in the remaining two. The reason for this variance is the different orientations of the Phe20 residue positioned at the 1 and 1` sites, which interact differently with the L2-b complex. This is due to the rigid docking simulations that do not allow for reorientation of the side chains of the fibril residues. On the other hand, the L2-b complex binds to site 2+2` in ten of the 20 top ranked poses (Figure 3.9).

It is formed by the Phe19, Asp23, and Lys28 residues which run longitudinally to the Aβ fibrils. It is interesting that site 2 was only occupied by three poses while site 2` was occupied by six poses. It may be due to the different orientation of Lys28 in the two-fold Aβ fibrils and the constraint imposed on the residue by rigid docking which prevents reorientation, thus preventing the binding of the L2-b complex.

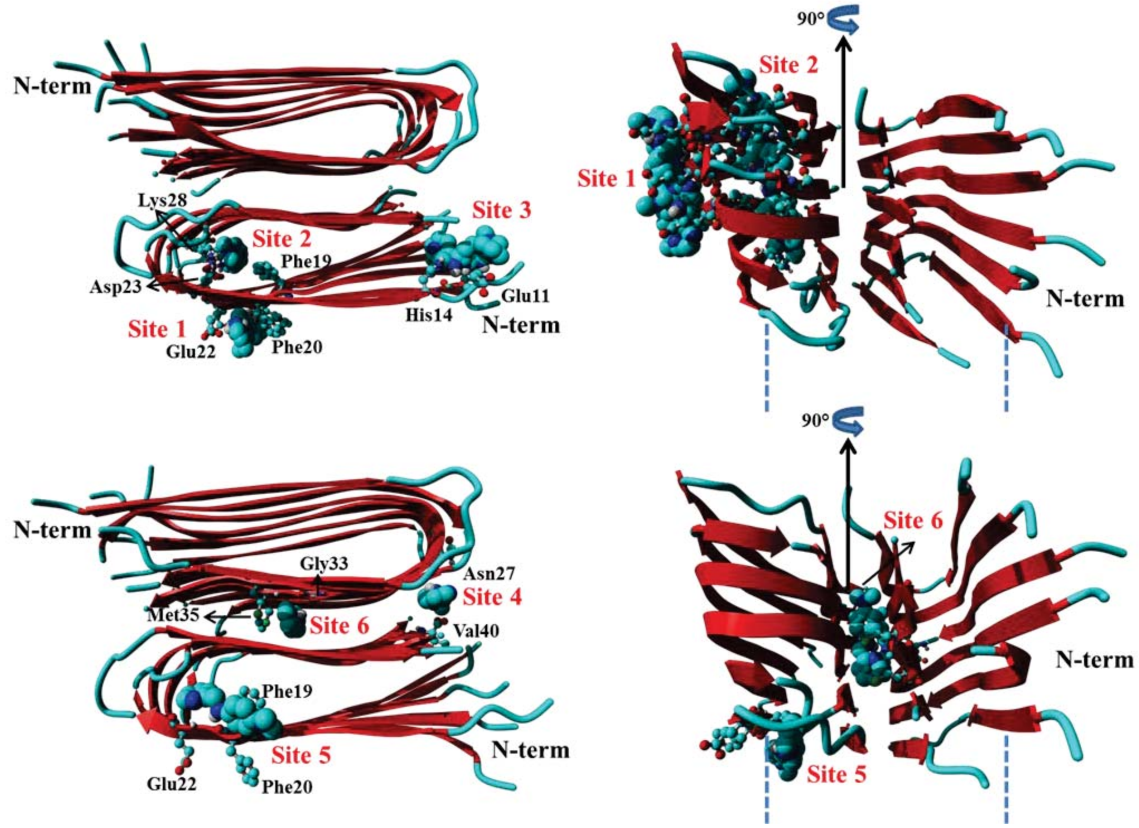

Figure 3.9. Binding sites of L2-b complex in two-fold Aβ fibrils from molecular docking

In addition, the L2-b complex binds to site 3+3` in the remaining three poses. This binding site is formed by the residues of Glu11 and His14 of the Aβ fibrils (Figure 3.9). To include the effect of receptor flexibility on the docking to these sites, we also performed flexible docking and rigid docking on different conformations of fibrils derived from short-term MD simulations. The results were similar using these methods and are summarized in Figure 3.9 for fibrils with two-fold symmetry. In the third technique, 5 snapshots of the Aβ fibrils derived from a short-term (5 ns) molecular dynamics (MD) simulation at each 1 ns interval in an aqueous solution were used for rigid docking. All 100 poses provided by rigid docking have been analyzed and six major sites have been found. The L2-b complex was found to bind to the 1+1` sites in 18% of poses obtained. The 2+2` and 3+3` sites were occupied in 66 (66%) and 8 (8%) of the poses, respectively. Sites 4, 5, and 6 have the occupation percentages of 4%, 2%, and 1% respectively. Of all the binding sites, it is obvious that site 5 is located at the ends of the fibril (Figure 3.9). Therefore, its contribution to the binding of the L2-b is negligible since binding sites at the end of the fibrils are scarce given the fibrillar elongation displayed by Aβ. As a result, the Aβ fibril will only have a maximum number of four possible binding positions for site 5+5`. In contrast to this, sites 1, 2, 3, and 4 lie longitudinally to the fibril axis, and their number would increase as more monomers were added and the fibril was elongated. In addition, we modeled the two-fold symmetry Aβ fibrils interaction with the L2-b complex using amino acids from 9−40 which form the fibril backbone. The amino acids from 1-8, occupying most of the region where sites 3 and 4 were found, are in a random coil conformation. This conformation will hinder the approach of the L2-b complex to sites 3 and 4. Hence, the binding interactions between the L2-b complex and the Aβ fibrils would decrease. In comparison to sites 3 and 4, site 1 shows binding to the surface of the fibril, while site 2 is located in the chamber of the stacks of the Aβ fibrils. Therefore, sites 1 and 2 are mostly responsible for the binding of the L2-b complex to Aβ40 fibrils. Moreover, the binding energy of site 2 (-6.5 kcal/mol) is more negative than that of site 1 (-6.3 kcal/mol), and the percentage of the L2-b complex bound to site 2 (66%) is much larger than that of site 1 (18 %).

3.10. L2-B2 Docking to 2-fold Fibril

In this study, three different docking procedures were employed in order to achieve an accurate starting structure for further molecular dynamics simulation (MD).

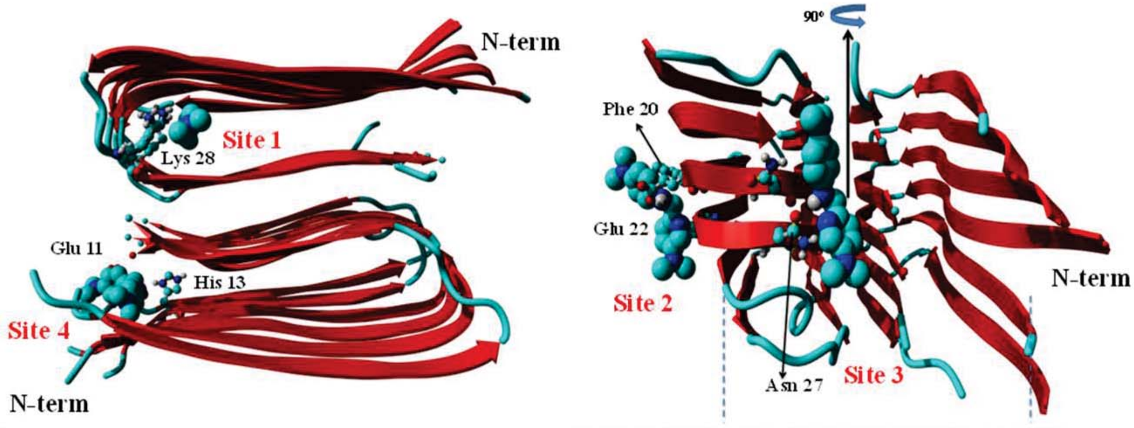

Figure 3.10. L2-B2 docking, showing sites 1, 2, 3, and 4 with interacting residues labeled.

The binding L2-B2 to the amyloid beta (AB40) two-fold symmetry structure was investigated implementing rigid docking, flexible docking, and rigid docking on different conformations of the AB40 peptide taken from a short MD simulation of the fibril alone. In all docking procedures, the ligand is kept flexible and receptor kept rigid excluding the flexible docking where both the ligand and receptor's movements are not restricted. The docking results (Table 3.4 and Figure 3.10) produced 4 binding sites for L2-B2, respectively. Due to the C2 symmetry of the two-fold structure, similar binding sites were found on either side of the fibril and are termed X and X`. The relative abundances of the docked sites obtained are listed in Table X and X. Sites 4+4` in both cases studied produced an appreciable abundance. However, this site was not chosen for further MD simulation due to steric hindrance originating from the eight missing residues that should be present attached to the N-terminus of the fibril.

Binding Site	Relative Abundance (%)	Interacting Aβ40 Residues (two-fold)
1+1`	45.0	Lys28
2+2`	31.0	Phe20, Glu22
3+3`	13.0	Asn27
4+4`	11.0	Glu11, His13

Table 3.4. Shows docking results for L2-B2 to the 2-fold fibril

For L2-B2, sites 1+1`, 2+2`, and 3+3` were chosen for further analysis. Site 1+1` as shown in Figure 3.11, possesses the highest abundance value. At that site, electronegative atoms attached to the small molecule are attracted to the positively charged protons present on the side chain of Lys28. Site 2+2` shows interactions with residue Phe20, contributing nonpolar interactions with the aromatic ring present on L2-B2 and Glu22 that forms a hydrogen bond with the amine nitrogen of L2-B2. Site 3+3` shows a minor interaction with Asn27, however is positioned on the edge of the fibril and could easily shift to another pocket on the fibrils surface.

3.11. L2-B, L2-B1 and L2-B2 Docking to Aβ40 Monomer

In Addition to fibril docking, L2-B, L2-B1 and L2-B2 were docked to *m*-Aβ40 (amyloid beta 40 monomer). Due to the flexibility of the monomer, a long 100 ns MD simulation was run on the peptide alone. Snapshots were taken every nanosecond to allow for docking to different *m*-Aβ40 conformations. 20 poses were obtained for each snapshot taken, totaling 2000 poses. Starting structures for MD were chosen based on residue binding abundances obtained through careful analysis of the docked poses. For L2-B, Table 3.5 shows relative abundance values for the docking of L2-B to *m*-Aβ40. The aromatic residues Phe4, Phe19, and Phe20 possess some of the highest percentages of 10.08, 6.37, and 19.75 respectively.

Residue	**Relative Abundance (%)**
Phe4	10.08
Arg5	8.17
His6	6.90
Val18	4.78
Phe19	6.37
Phe20	19.75
Binding site	**Interacting *m*-Aβ40 Residues**
1	Arg5, Phe4, His6
2	His14, Val18
3	Phe20, Phe4

Table 3.5. Shows the relative abundance of interacting m-Aβ40 residues with L2-B with binding sites identified.

Residue	**Relative Abundance (%)**
Phe4	9.60
His6	5.48
Tyr10	6.54
Val18	6.35
Phe19	11.10
Phe20	17.55
Binding site	**Interacting *m*-Aβ40 Residues**
1	Phe4, His6, Tyr10
2	Val18, Phe19
3	Phe4, Phe20

Table 3.6. Shows the relative abundance of interacting m-Aβ40 residues with L2-B1 with binding sites identified.

In addition, His6 and positive residue Arg5 both have appreciable abundance values of 6.90 and 8.17 respectively. Additionally, Table 3.5 lists all three possible binding sites found for L2-B bound to *m*-Aβ40. L2-B1 docking results are very similar to the other two variants, and are shown in Tables 3.6. Table 3.7 shows the relative abundance percentages of interacting *m*-Aβ40 residues with L2-B2. The aromatic residues Phe4, Phe19, and Phe20 possessed the highest abundance values of 8.71, 6.73, and 11.58% respectively. Table 3.7 shows the initial interacting residues located at each site for L2-B2 (starting structures). In all three cases, L2-B, L2-B1 and L2-B2 bind with a greater affinity to hydrophobic regions of the Aβ40 monomer when compared to hydrophilic regions where charged residues dominate.

Residue	Relative Abundance (%)
Phe4	8.71
Arg5	6.83
His6	8.42
Val18	5.35
Phe19	6.73
Phe20	11.58
Binding site	**Interacting *m*-Aβ40 Residues**
1	Arg5, Phe4, Phe20, His6
2	His14, Lys16, Val18, Gln15
3	Phe20, Glu3, Phe4

Table 3.7. Shows the relative abundance of interacting m-Aβ40 residues with L2-B2 with binding sites identified.

Hydrophobic regions form distinct pockets that are comprised of non-polar and aromatic residues that facilitate the binding of these small molecules.

3.12. Molecular Dynamics on L2-B Bound to 2-fold Aβ40 Fibrils

In the next step, 50 ns unrestrained, all-atom molecular dynamics (MD) simulations in explicit aqueous solution were performed to investigate the stability of sites 1 and 2, respectively. These simulations were performed using the GROMOS53a6[111] force field as implemented in the GROMACS[108] program. The L2-b complex showed interactions with the Aβ fibrils throughout the simulations. No significant change in the orientation of the complex was observed in the binding sites after docking and 50 ns MD simulations. Site 1 is a cleft formed by Phe20 and Glu22 in the most representative structure derived from the 50 ns MD simulation. The L2-b complex is observed to form a hydrogen bond with the side chain carboxyl oxygen of Glu22 at a distance of 2.34 Å.

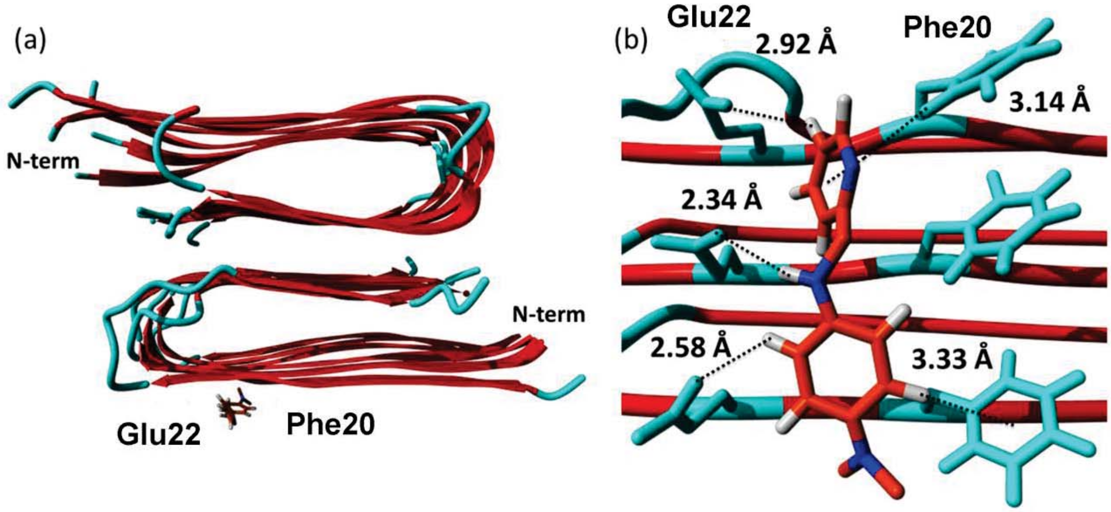

Figure 3.11. 2-fold Aβ fibril and L2-B binding site 1 after 50 ns molecular dynamics simulation. (a) Binding pocket formed between residues Phe20-Glu22, view of the whole fibril with N terminus labeled. (b) Zoomed in view of the binding pocket with residues (cyan) and interaction distances labeled in angstroms.

Two separate Phe20 residues coordinate through a π–π and a CH-π interaction with the rings of the L2-b complex at distances of 3.33 and 3.14 Å, respectively. The details of the structure can be found in Figure 3.11a and 3.11b. In site 2, the L2-b complex was buried in a hydrophobic cleft. At this site, the pyridine ring of L2-B interacts with residues Phe19 through a CH-π interaction at a distance of 2.80 Å (Figure 3.12a and 3.12b).

Additionally, Lys28 forms a hydrogen bond with the same pyridine ring at a distance of 2.12 Å. Ile32 also shows a CH-π interaction with the pyridine ring of L2-B. These interactions align the hydrophobic part of the L2-b perfectly into the hydrophobic chamber of site 2 (Figure 3.13).

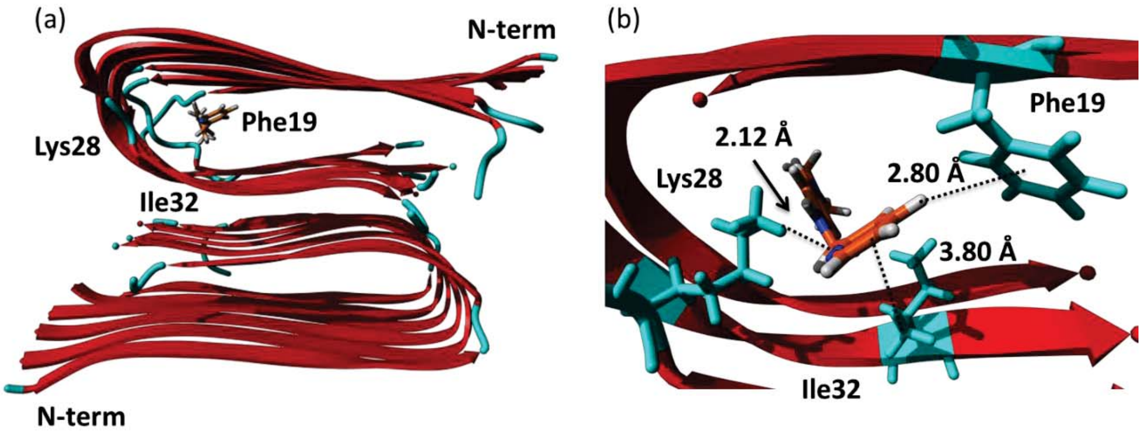

Figure 3.12. 2-fold Aβ fibril and L2-B binding site 2 after 50 ns molecular dynamics simulation. (a) Binding pocket formed between residues Phe19-Ile32, view of the whole fibril with N terminus labeled. (b) Zoomed in view of the binding pocket with residues (cyan) and interaction distances labeled in angstroms.

3.13. Molecular Dynamics on L2-B2 Bound to the 2-fold Aβ40 Fibril

Unrestrained 50 ns molecular dynamic simulations were performed on the starting structures obtained for L2-B2 bound to the AB40 fibril from molecular docking. For L2-B2, site 1+1` is stabilized by a π-π interaction between the aromatic side chain of Phe19 and the aromatic ring present on L2-B2 at a distance of 4.75Å. In Addition, Ala21 of the same site further stabilizes L2-B2 within the hydrophobic pocket of the fibril by contributing a CH-π interaction at a distance of 4.20Å. The MD most representive structure is shown in Figure 3.13. At site 2+2`, L2-B2 is held on the fibril edge by a host of Phe20 residues each contributing CH-π interactions (Figure 3.14) with the aromatic portions of L2-B2. Glu22 further stabilizes this binding site through weak hydrogen bonding with an amine group attached to L2-B2 at a distance of 3.86Å. The binding pocket located at site 3+3` consists of a hydrophobic residue Val39 and a polar residue Lys28.

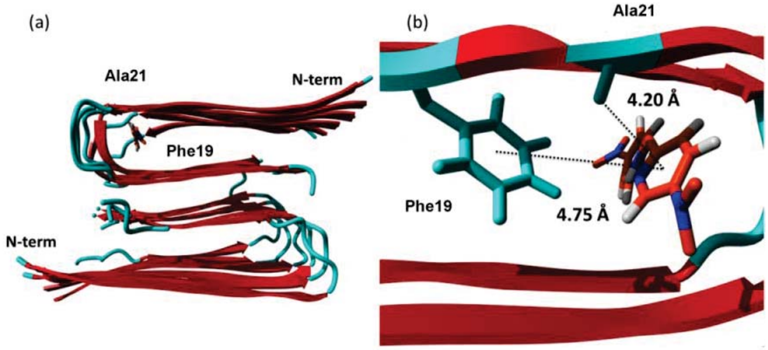

Figure 3.13. 2-fold Aβ fibril and L2-B2 binding site 1 after 50 ns molecular dynamics simulation. (a) Binding pocket formed between residues Phe19-Ala21, view of the whole fibril with N terminus labeled. (b) Zoomed in view of the binding pocket with residues (cyan) and interaction distances labeled in angstroms.

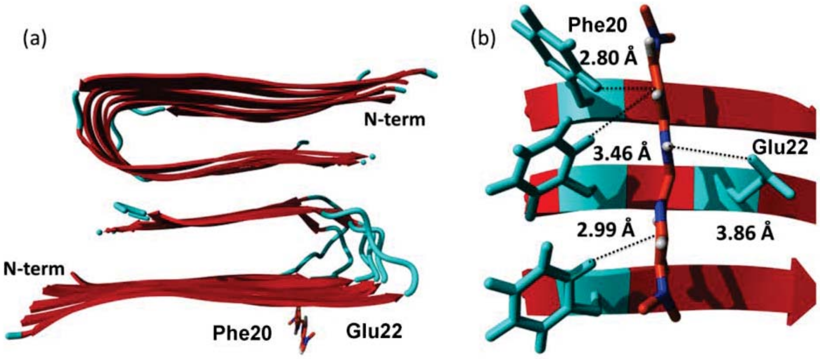

Figure 3.14. 2-fold Aβ fibril and L2-B2 binding site 2 after 50 ns molecular dynamics simulation. (a) Binding pocket formed between residues Phe19-Ala21, view of the whole fibril with N terminus labeled. (b) Zoomed in view of the binding pocket with residues (cyan) and interaction distances labeled in angstroms.

Val39 interacts through a CH-π interaction with the aromatic ring of L2-B2 at a distance of 3.82Å, while Lys28 contributes weak hydrogen bonding at a distance of 3.87Å. However, Site 3 is not shown.

3.14. Molecular Dynamics on L2-B, L2-B1, and L2-B2 Bound to Aβ40 Monomer

Unrestrained 25 ns molecular dynamics simulations were performed on the starting structure obtained from docking L2-B to *m*-Aβ40.

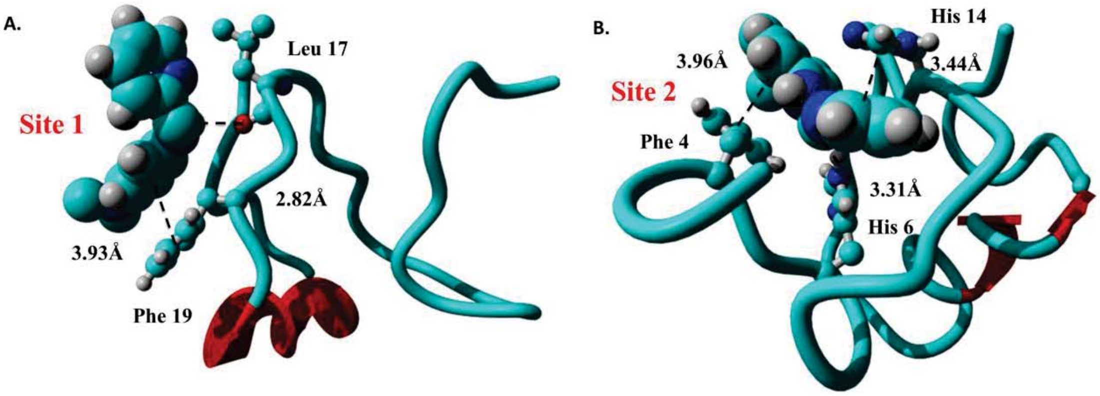

Figure 3.15. L2-B binding sites after 25 ns molecular dynamics simulations. (A) Binding site 1 of Aβ40 monomer and (B) binding site 2 of Aβ40 monomer. Zoomed in snapshots of the binding pocket for both sites are shown.

The first 5 ns of the simulation were part of the pre-production phase. The following 20 ns were part of the production phase. Cluster calculations were performed on the production phase only. At site 1 (Figure 3.15a), hydrophobic residue Phe19 interacts with L2-B through a strong π-π interaction at a distance of 3.93 Å. In addition, the carbonyl located in the backbone of Leu 17 forms a strong hydrogen bond with the amine bridging the two aromatic rings of L2-B at a distance of 2.82 Å. Interestingly, if the side chain of Leu 17 were allowed to rotate more than 30^0, a strong CH-π interaction would be gained and this site further enhanced (Figure 3.15a). Rotations of this kind would be allowed due to the unrestricted and flexible structure of *m*-Aβ40. Site 2 is stabilized by both polar and non-polar residues (Figure 3.15b). Both Phe 4 and His 6 interact through a π-π interaction at distances of 3.96 and 3.44 Å, respectively.

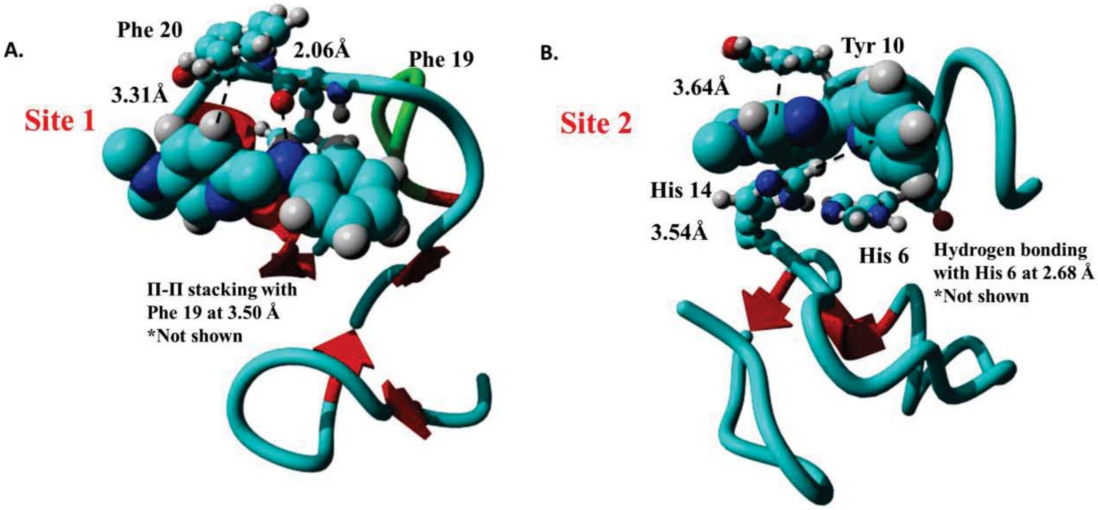

Figure 3.16. L2-B1 binding sites after 25 ns molecular dynamics simulations. (A) Binding site 1 of Aβ40 monomer and (B) binding site 2 of Aβ40 monomer. Zoomed in snapshots of the binding pocket for both sites are shown. For (A) Π-Π stacking with Phe 19 and (B) hydrogen bonding with His 6 on the reverse side, not shown.

Furthermore, His 6 displays moderate hydrogen bonding with the amine present on L2-B at a distance of 3.31 Å. Site 1 is primarily stabilized by hydrophobic residues whereas for site 2, both hydrophobic and hydrophilic residues help to stabilize the interacting cleft. From MD, zoomed in clustered snapshots are shown in Figure 6A and 6B. At site 1, L2-B1 is held between two aromatic residues Phe19 and Phe20 by π-π and CH-π interactions, respectively (Figure 3.16a). The π-π interaction with Phe 19 occurs at a distance of 3.50 Å which indicates strong orbital overlap between their π clouds. The CH-π interaction occurs at a distance of 3.31 Å and could potentially form an additional π-π interaction, if the aromatic ring present on L2-B1 was to rotate by 70^0. Additionally, the backbone atoms of Phe 19 show a strong hydrogen bond with the amine bridging the two aromatic rings of L2-B1 at a distance of 2.06 Å.

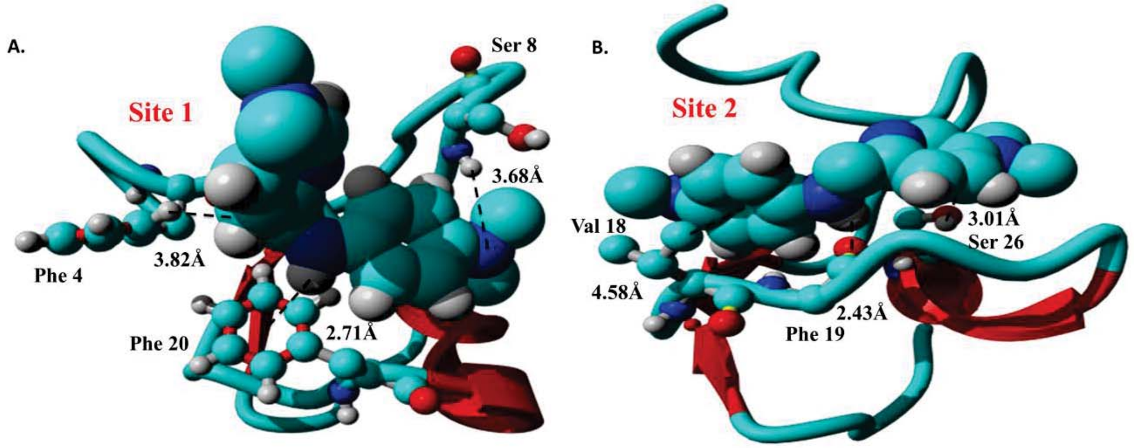

Figure 3.17. L2-B2 binding sites after 25 ns molecular dynamics simulations. (A) Binding site 1 of Aβ40 monomer and (B) is binding site 2 of Aβ40 monomer, respectively. Zoomed in snapshots of the binding pocket for all three sites are shown.

At site 2, only polar amino acids interact with L2-B1 (Figure 3.16b). Tyr 10 displays a π-π interaction with the aromatic ring of L2-B1 at a distance of 3.636 Å. Additionally, a CH-π interaction was observed between His 14 and the aromatic ring of L2-B1 at a distance of 3.54 Å. The bridging amine in L2-B1 forms a strong hydrogen bond with His 6 at a distance of 2.68 Å. Just like for L2-B, Site 1 is primarily stabilized by hydrophobic residues whereas for site 2, hydrophilic residues help to stabilize the interacting site. At site 1, L2-B2 is held between two aromatic residues Phe4 and Phe20 by CH-π and NH-π interactions, respectively (Figure 3.17a). The NH-π interaction occurs at a distance of

2.71Å while the CH-π interaction occurs at 3.82Å. Furthermore, the tail end of L2-B2 is stabilized by weak hydrogen bonding from Ser8 at a distance of 3.68Å. At site 2, Phe19 and Ser26 interact with L2-B2 through hydrogen bonding at distances of 2.34Å and 3.01Å, respectively (Figure 3.17b). In addition, the hydrophobic side chain of Val18 interacts with the aromatic ring of L2-B2 through a CH-π interaction at a distance of 4.58Å.

Small Molecule	Binding Site	Electrostatic Contribution (kcal/mol)	Hydrophobic Contribution (kcal/mol)	Binding Energy (kcal/mol)
L2-B	1	0.164	-2.881	-2.717
L2-B2	1	2.831	-3.982	-1.151
	2	1.879	-3.235	-1.357

Table 3.8. Binding energies are listed for L2-B and L2-B2 binding to the Aß40 fibril with electrostatic and hydrophobic contributions to the overall binding energy. More negative values indicate better binding.

Small Molecule	Binding Site	Electrostatic Contribution (kcal/mol)	Hydrophobic Contribution (kcal/mol)	Binding Energy (kcal/mol)
L2-B	1	0.847	-1.711	-0.864
	2	1.105	-2.639	-1.534
L2-B1	1	1.292	-2.439	-1.147
	2	2.581	-2.839	-0.258
L2-B2	1	0.685	-2.053	-1.368
	2	1.132	-3.014	-1.882

Table 3.9. Binding energies are listed for L2-B, L2-B1, and L2-B2 binding to the Aß40 monomer with electrostatic and hydrophobic contributions to the overall binding energy. More negative values indicate better binding.

3.15. Summary and Conclusions

In summary, binding sites have been identified and characterized for two small molecules, L2-B and L2-B2, binding to the Aß40 fibril. From docking and MD two primary sites were identified (site 1 and 2) for each, however site 1 of L2-B corresponds to site 2 of L2-B2 and vice versa. Nevertheless, Site 1 (L2-B) was located in a hydrophobic cleft formed from residues Lys28, Phe19, and Asp23. Site 2, was located on the surface of the fibril between residues Glu22 and Phe20. It is clear from docking and molecular dynamics these small hydrophobic molecules readily bind to hydrophobic regions within the fibrils. Additionally, the L2-B, L2-B1, and L2-B2 molecules were docked to the monomer form of the Aß40 peptide. From the results, residues Phe4, Arg5, Phe19, Phe20, Val18, and His6 contribute the most to the binding of these small molecules. After the MD simulations, all three small molecules (L2-B, L2-B1, and L2-B2) bind to similar sections along the Aß40 monomer interacting primarily with hydrophobic residues Phe19 and Phe20. Given this result it is expected that L2-B2 will have the best binding to both the monomer and fibril forms of the Aß40 peptide. However, they all bind in a very similar manor and similar strengths as shown in Tables 3.8 and 3.9.

3.16. Identification of Molecular Binding Sites on Amyloid Beta Fibrillar Aggregates

Experimental binding site identification and characterization of small molecules to proteins is often done using X-ray crystallography,[148-149] in which the protein is co-crystallized with the small molecule of interest. However, in the case of Aβ fibrils, this is a challenging task due to the diverse morphologies of the fibrils which include regions of high degrees of disorder.[100] Furthermore, current X-ray structures are obtained from fibrils that are grown from short segments of the Aβ peptide.[150-153] Fibrils that are prepared from shorter segments are not necessarily the same in structure to those formed from the full length Aβ peptide.[100] Thus, the identification of binding sites on the Aβ fibrils produced by the full length peptide are not trivial in nature.[100] In this work, both docking and molecular dynamics has been employed to identify and characterize the binding site of a Rhenium centered photoluminescence probe $[Re(CO)_3(dppz)(py)]^+$ to Aβ fibrils. These results were compared to spectroscopic data where a photochemical oxidation technique was used that provides a footprint near the site of binding.[100] Furthermore, simulations were run to determine the extent of oxygen trapping within the Aβ fibril stacks which is required for the photochemical oxidation to take place.

3.17. Molecular Docking of $[Re(CO)_3(dppz)(py)]^+$ to Aβ Fibrils

The Re-complex $[Re(dppz)(CO)_3(py)]^+$ has been docked to the dominant morphology of Aβ fibrils, which display a two-fold structure. Due to their C2 symmetry, these fibrils contain a similar binding sites within separate domains which will be termed X and X`. Parameters for Re^+ were not available in the molecular dynamics program; hence the Re^+ atom was replaced by Mn^{2+} in the docking simulations. Mn^{2+} is a good approximation for the Re^+ metal center as the $[Re(dppz)(CO)_3(py)]^+$ complex interacts with fibrils only through its aromatic ligands (dppz or pyridine). Moreover, the Mn^{2+} and Re^+ atoms are similar as they are in the same group of the periodic table. Aβ fibril flexibility of the docked structures was compared by using two methods: (1) flexible docking and (2) rigid docking on the different structures of the Aβ fibrils derived from short-term (5 ns) molecular dynamic (MD) simulations in an aqueous solution. Docking the Re-complex onto the two-fold Aβ structure produced ten top-ranked sites. In eight of them, the Re-complex binds in the same position within separate domains of the fibril structure. The first site, termed A and A`, shows interaction with residues Phe20, Val18, and Lys16. The most dominant site, B and B`, was found to interact with residues Gly9, Tyr10, Asn27, Val39, and Val40. However, site B and B` contributions to the overall binding can be neglected due to the use of a truncated form of the Aβ fibril during the simulations, where the first eight amino acid residues have been left out. Within this portion (1-8), the linked amino acids form random coil secondary structure that would block the binding of the Re-complex to this site. Site C and C` is slightly less dominating than the A and A` site due to a much higher surface area within the latter.

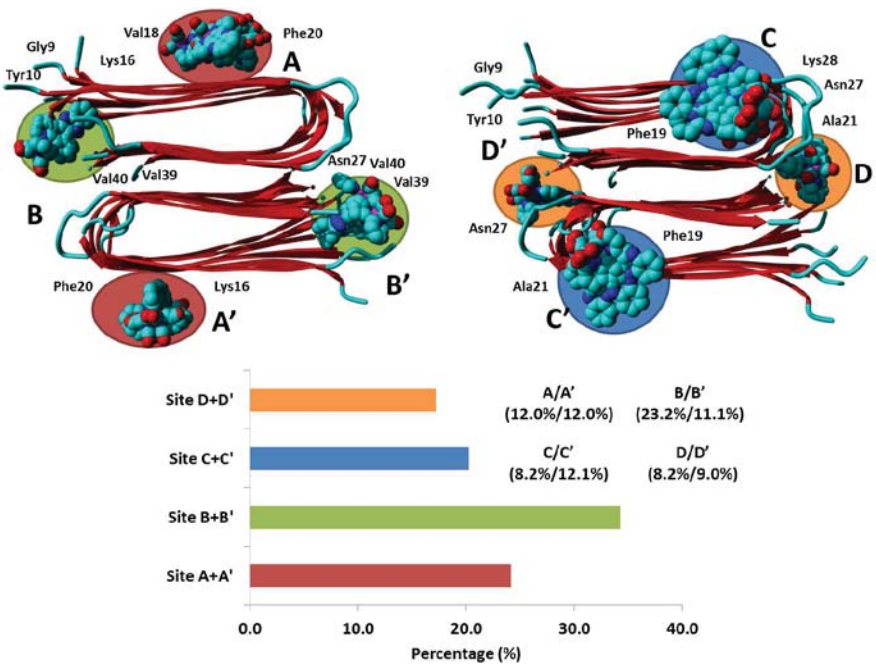

Figure 3.18. Docking results from rigid docking on different conformations of the two-fold Aβ40 fibril, where the flexibility of the ligand was maintained and conformational space of the fibrils sampled

Binding sites at the end of the fibril are scarce given the fibrillar elongation displayed by Aβ, so their binding is negligible. For example, there would be a maximum of four C and C` binding sites during the fibrillation process, whereas binding sites located on top of the fibril would increase as the number of monomer units increased. Therefore, it is plausible that site A and A` contributes the most to the binding of $[Re(dppz)(CO)_3(py)]^+$

to Aβ fibrils. Poses totaling 140 were analyzed. Two docking methods were used to insure accurate sampling of conformational space for both the receptor and ligand. In the second technique, the Aβ fibril structure was equilibrated using a short-term molecular dynamics simulation where sides chains where allowed to change conformation.

Binding Site	**Interacting Aβ40 Residues (2-fold)**
A+A’	Phe20, Val18, Lys16
B+B’	Gly9, Tyr10, Asn27, Val39, Val40
C+C’	Asn27, Ala21, Phe19, Lys28
D+D’	Asn27, Gly9, Tyr10
E	His14, Lys16, Val12
F	Leu34, Val36

Table 3.10. Interacting Aβ40 residues shown for each binding site

Structures were chosen at 1 ns intervals and were utilized in the rigid docking scheme. This approach has been widely utilized in computational chemistry.[154-156] The Re-complex was found to bind to A and A` sites 24% of the time and shows an even split of 12% each when comparing the A site to A`. The B and B` sites are the most dominant when comparing the docked poses obtained, occurring 34% of the time. However, this binding site can be neglected due to its binding position where eight more amino acids should be present. The eight missing amino acids form random coil secondary structure that would essentially block the binding to this site. Site C and C` occurred in 20% of the poses analyzed and exists where the Re-complex binds to the side of the fibril, interacting with polar residue Lys28 and non-polar residues Phe19, Ala21, and Asn27. Site C` occurs with slightly higher frequency than site C and interacts with the same residues. The rigid docking also shows the existence of site D and D` that is bridging the gap between the two domains of the Aβ structure. This site occupies 17% of the total poses analyzed and interacts with non-polar residues Gly9, Tyr10, and Asn27. Again, it is possible that this site exists only due to the absence of the first eight amino acids present in the pristine fibril structure. Two more sites were observed in the rigid docking scheme, termed E and F, but occurred with such a low frequency that they were excluded from further analysis. Docking results are shown in Figure 3.18 and interacting residues are shown in Table 3.10.

3.18. Molecular Dynamics Simulations of $[Re(CO)_3(dppz)(py)]^+$ Binding to Aβ Fibrils

More than 20 molecular dynamics simulations were performed to insure accurate and precise binding of the $[Re(dppz)(CO)_3(py)]^+$ to the Aβ fibril. The stability of site A and A` was investigated utilizing a 50 ns molecular dynamic simulation in explicit solvent. These simulations were performed in GROMACS-4.5.6[108] software with AMBER03[113, 157] force field parameters. NMR constrains were added to the $[Re(dppz)(CO)_3(py)]^+$ complex in order to accurately maintain the geometry as well as the coordination to the metal center. The dppz ligand was kept at 180 degrees as it was required to remain planar throughout the simulations. The pyridine ring was also locked at 180 degrees with respect to the opposite CO ligand, but was allowed to rotate during the simulations. During the MD simulations C_α atoms of the Aβ fibril were frozen in place to maintain the stability of the fibril structure. These atomic constraints helped to maintain the secondary structure of these fibrils without affecting the flexibility of their side chains within the binding sites. The interaction persisted between the $[Re(dppz)(CO)_3(py)]^+$ complex and the $A\beta_{40}$ fibril throughout the simulation. However, changes in the orientation of the Re-complex were observed in many of the simulations (more than 80%).

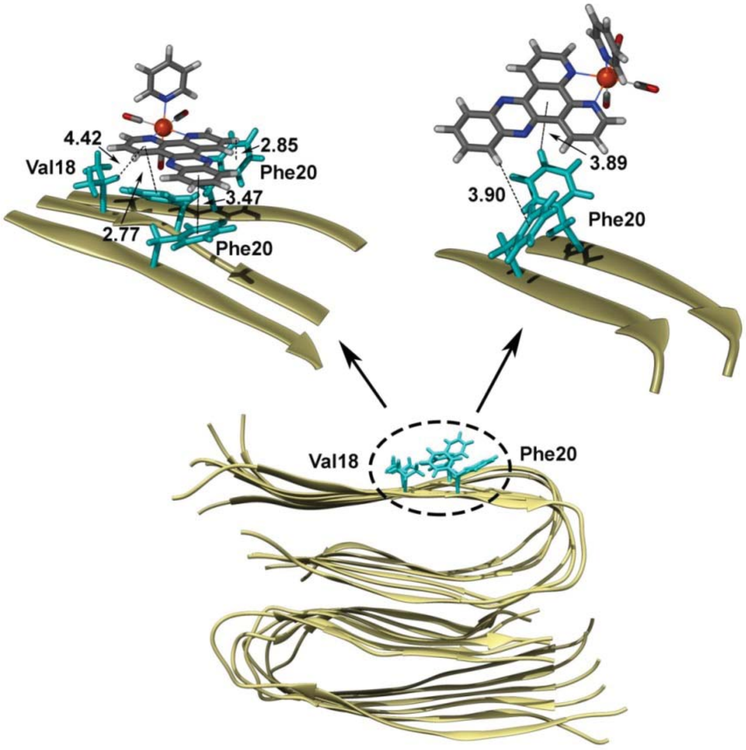

Figure 3.19. Binding modes for [Re{CO)3(dppz)(py)]+ to site A on the two-fold structure of the Aβ40 fibril

Two distinct binding modes were observed within the same binding pocket termed primary and secondary (Figure 3.19). During the simulations, the $[Re(dppz)(CO)_3(py)]^+$ complex shifted between two conformations; the first was embedded within the fibril's hydrophobic pocket between residues Val18 and Phe20 and the second was raised out of the hydrophobic pocket exposing the dppz ligand to a more hydrophilic environment. The primary binding mode, shown in Figure 3.19, was observed to occur more than 75% of the time within the simulations while the secondary mode was observed to occur less frequently. This is mostly due to the increased interaction between hydrophobic residues within the pocket that stabilizes the primary site more often compared to the secondary binding mode where only one π-π interaction holds the complex. Thermodynamically, the primary mode should dominate and was observed in the majority of the simulations.

The primary binding mode was buried within the hydrophobic pocket, extending down the fibril parallel to the beta-sheet axis. The dppz ligand is a hydrophobic extended aromatic system which can hide from more hydrophilic environments and does so throughout our simulations. This result was supported by binding constants and Job plot analysis that supports the occurrence of a non-polar binding domain on the surface of the Aβ fibril between Val18 and Phe20 where hydrophobic groups can readily bind.[100] The $[Re(dppz)(CO)_3(py)]^+$ complex interacts strongly through π-π interactions with the fibril surface at distances less than 4 Å. CH-π interactions were also observed between residue Val18 and the dppz ligand. Notably, the pyridine ring also shows interaction with the non-polar residue Phe19 at a distance of 3.57 Å. However, during the simulations, pyridine ring rotations were observed which could explain the secondary binding motif. As the pyridine ring rotates, the binding pocket is destabilized, allowing the dppz to turn outwards and expose itself to a more hydrophilic environment. However, the dppz was never allowed to turn fully out of the pocket due to such strong π-π interactions observed (<4Å , Fig 3.19).

3.19. Molecular Dynamics Simulations on Trapping Oxygen within Aβ Fibrils

MD simulations in the presence of 19 oxygen molecules showed that molecular oxygen can be trapped within the Aβ fibrils.

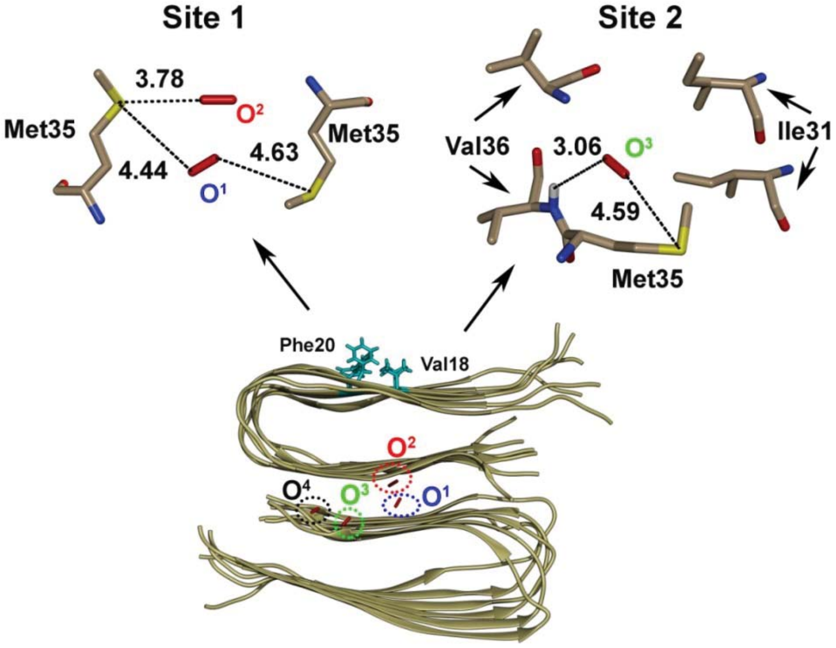

Figure 3.20. Molecular dynamics simulations of molecular oxygen pockets near Met35 residues.

Out of 19 molecules placed, four oxygen molecules (O^1-O^4) were located inside the hydrophobic core of the Aß fibrils after 200 ns simulations (Figure 3.20). The first (O^1) and second oxygen (O^2) were embedded deep inside the hydrophobic pocket of the two domains and were in proximity of five Met35 residues within the stacks. The O^1 molecule was surrounded by four Met35 residues at distances of 4.44, 4.63, 4.87, and 5.76 Å. Additionally, a second oxygen molecule (O^2), close in proximity to O^1, was surrounded by five Met35 residues at distances of 3.78, 4.21, 5.04, 5.41, and 5.73 Å. A third oxygen molecule (O^3) was near only two Met35 residues at distances of 4.59 and 5.56 Å. However, the fourth oxygen molecule (O^4) was considerably distant from Met35 at a distance of 8.55 Å. Oxygen is a small, hydrophobic molecule that can interact with the hydrophobic interior of the fibril, however these simulations only show that oxygen is stable in this hydrophobic environment and cannot completely explain how oxygen gets there. In the simulations, C_α atoms of the Aβ fibrils were frozen in place to maintain the stability of the fibril structure, which prevented exploring the dynamic fluctuations in structure that were likely to contribute to the diffusion of oxygen to these regions. On the other hand, studies have identified that the maturation and even photobleaching of fluorescent proteins such as mCherry were associated with the penetration of molecular oxygen into the beta barrel through gaps in the structure.[158] Structural defects like kinks, twists, and bends in the fibrils structure could introduce these gaps allowing oxygen to access the hydrophobic interior.

3.20. Summary and Conclusions

In summary, complementary docking and MD simulations identified a molecular binding site for a Rhenium centered photoluminescence probe [Re(dppz)(CO)3(py)]+ to Aß fibrils. The site was located in a hydrophobic regions formed between residues Val18 and Phe20 on the surface of the Aß40 fibrils. After MD, two primary binding modes were observed, one were the dppz ligand was buried within this hydrophobic region, and another where the dppz was exposed to a more solvated environment. These separate binding modes could explain the light-switching ability of this molecule; however, only partially as more experimental evidence is needed. Furthermore, our simulations show that molecular oxygen can be trapped within the fibril stacks in the vicinity of many

Met35 residues. However, that exact pathway of the oxygen molecules remains elusive and will need to be explored in future simulations.

Chapter 4. Structural and Mechanical Properties of Amyloid Beta Fibrils

In this chapter, the computational methods used to obtain amyloid fibrils of varying lengths will be discussed. Furthermore, geometric parameters obtained from theoretical *in-silco* structures will be compared to experimental values. Lastly, mechanical properties such as Young's modulus, ultimate tensile strength, and bulk and shear modulus obtained from computational derived amyloid fibril structures will be discussed and compared with experimental values obtained using atomic force microscopy nanoindention techniques.

4.1. Constructing Amyloid Beta 40/42 Fibrils of Varying Lengths

Despite the availability of smaller fragments of Amyloid fibrils such as 2LMN[159] for Aβ40 and 5KK3[160] for Aβ42, structures of full length fibrils are not readily available.

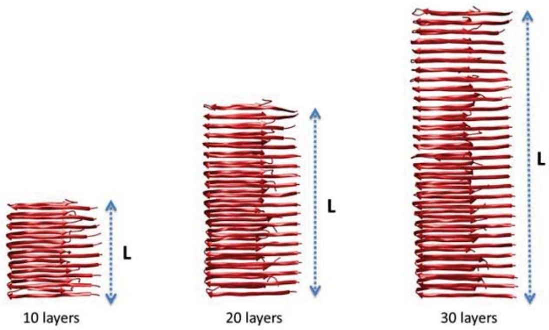

Figure 4.1. Smaller Aß40 fibrils showing the growth along the principle axis of aggregation

Amyloid fibrils are non-crystalline solid materials that are not amendable to either X-ray crystallography or liquid state NMR.[161] Therefore, full length structures were constructed *in-silco* integrating the available crystallographic and NMR data within the models (Figure 4.1) . For Aβ40 fibrils, Each amyloidogenic fibril $(A\beta40)_n$ was made up of Aβ40 peptides (monomers) consisting of 32 amino acids, where n is number of the Aβ40 monomers.

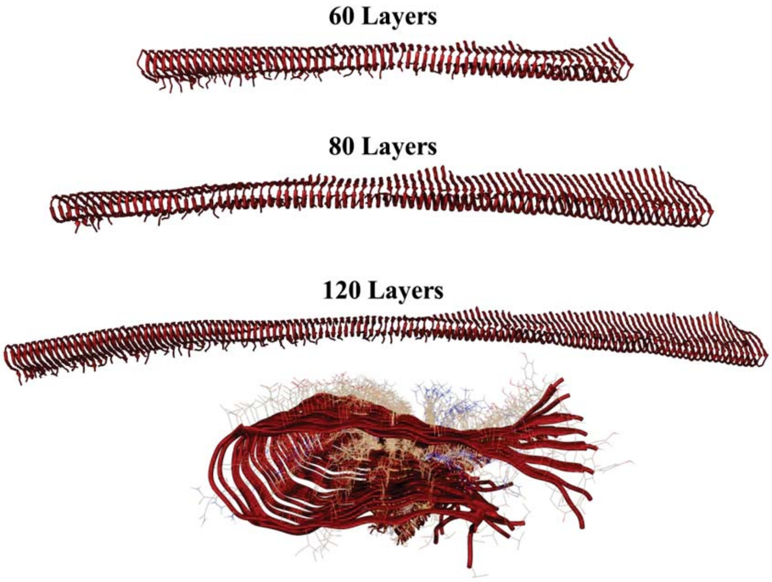

Figure 4.2. Larger *in silico* grown Aß fibrils structures highlighting the degree of fibril twist as the structures become longer. Also showing the typical morphology of Aß40 fibrils that form a “C-shaped” cross section

The amino acid sequence of each monomer begins with Gly9 through Val40, where the first eight amino acids were not resolved in solid state NMR and left out from subsequent molecular dynamics simulations. Amyloid fibrils were essentially grown, starting with a Aβ40 fibril structure that was generously provided by Robert Tycko using a solid-state nuclear magnetic resonance (NMR) method (PDB ID: 2LMN)[159]. This starting structure consisted of five monomer units (n=5) within each domain (two in total). Molecular dynamics simulations were performed to relax ($A\beta40)_5$ in an aqueous environment which allowed for a steady state structure to be obtained. The validity of this beginning fibril structure was proven by RMSD calculations performed with a strict cut-off of 0.3 nm.

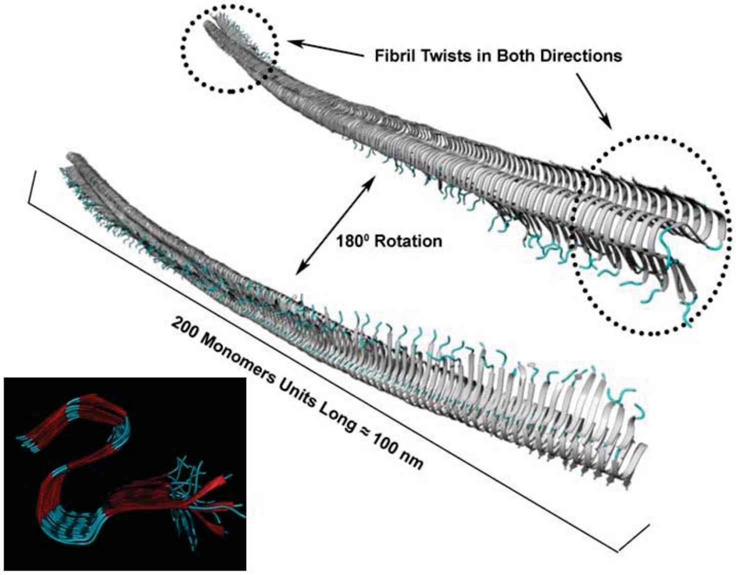

Figure 4.3. Largest Aß42 fibril structure studied showing "S-shape" morphology. The degree of the fibril twist is shown

Copies of $(A\beta40)_5$ were used to grow these fibrils in an ordered fashion. First, single interior monomer units were selected and copied from both domains and were added to the end of $(A\beta40)_5$. This new structure was then equilibrated using long MD simulations with all of the same parameters used with the previous $(A\beta40)_5$ structure. This procedure was repeated until a structure $(A\beta40)_{120}$ was obtained (Figure 4.2). For Aβ42 fibrils, the same procedure was followed however a different starting structure was used from the Protein Data Bank under PDB ID: 5KK3[160]. This structure was obtained using magic angle spinning nuclear magnetic resonance (MAS NMR) and consisted of 32 amino acids where the amino acid sequence begins with Glu11 through Ala42. The first ten amino acids were part of a random coil section that adopts many conformations and was not solved crystallographically. The *in-silco* growth procedure stated above was repeated until a structure (Aβ42)$_{200}$ was obtained (Figure 4.3).

4.2. Validation of *in-silco* Produced Amyloid Beta 40/42 Fibrils Using Geometric Parameters

The validity of the amyloid beta fibrils structures was tested utilizing a comparison between computational calculated and experientially determined geometric parameters such as secondary structure, interstrand twist and distance, and periodicity.

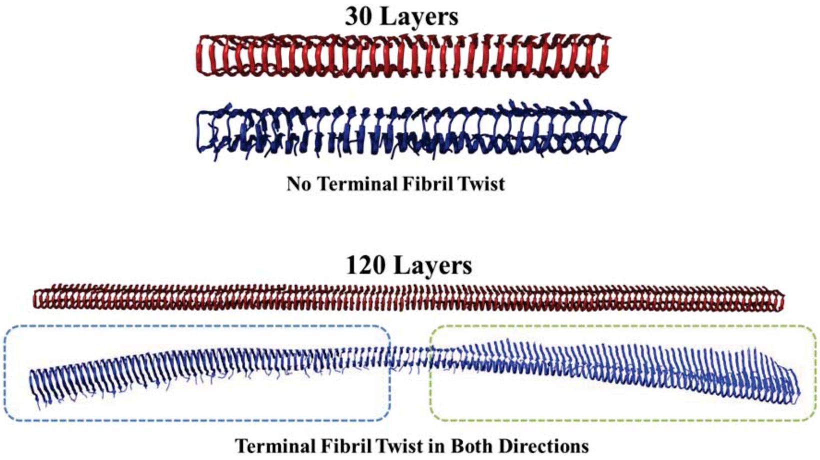

Figure 4.4. The initial and clustered Aß40 fibril structures taking from the molecular dynamics simulations. Structures in red correspond to the initial constructed conformations while the blue is the clustered result after molecular dynamics

The extrapolated asymptotic values for the inter-strand distance, twist angle, and periodicity were calculated utilizing relaxed structures obtain from molecular dynamics simulations. The inter-strand distance was calculated based on fibril length and the equation $L/n=d$, where L is length, n is the number of monomer units, and d is the inter-strand distance. Length measurements were extracted using the Yasara[162] program package where fibrils where fit to molecular volumes. The inter-strand twist angles were calculated from the molecular dynamics simulation trajectories, where V19, L34, and S26 were used as anchor points that provided two best-fit planes between monomers, which allow the angle between them to be obtained.

Monomers	B-sheet (%)	R. Coil (%)	Fibril Twist	*d* (nm)	θ (^{0})	Periodicity *v* (nm)
20	87.8	12.2	3.57 ± 1.94			
30	89.2	10.8	4.17 ± 2.34			
40	89.5	10.5	10.49 ± 5.11	0.477	1.50	114.5
50	90.6	9.4	8.91 ± 3.63	0.479	1.47	117.3
60	90.4	9.6	9.19 ± 3.69	0.479	1.29	133.7
80	90.7	9.3	17.36 ± 4.38	0.481	1.34	129.2
120	90.4	9.6	25.02 ± 6.05	0.481	1.32	131.2

Table 4.1: Secondary structure analysis of Aβ40 fibrils where N=20 to N=120. Fibril twist calculated from MD simulations. This value represents the twist angle from one end of the fibril to the other. *d*, θ denote the inter-strand distance and twist angles between adjacent monomers, respectively. Length of the fibril, $L=n\times d$, where *n* is the number of monomer layers in an amyloid fibril.

In addition, monomer units were chosen from the interior of the fibril due to large variations at either end that contributes to higher inter-strand twists that would not exist if the fibrils were to persist. Periodicity was calculated using the equation $v=360\times d/\theta$, where d and θ are the inter-strand distance and inter-strand twist angle, respectively. The Periodicity (v) is defined as the minimum length needed to cover a twist angle of 360°. In the Aβ40 structures, side-chains emanating from two separate monomer units were held together by interdigitating like the teeth on a zipper by intermolecular forces such as hydrogen bonding, π-π interactions, and CH-π interactions.[163] Furthermore due to the fact there was no water found between the monomer units it has been termed the "dry steric zipper."[163] Steric zippers are formed from self-complementary amino acid sequences, in which their side chains can mutually interdigitate. The fibrils were found primarily to be β-sheet in character (88%) with small random unordered sections at either end (12%). This dominant β-sheet structure was supported by measured Deep Ultraviolet Resonance Raman data that showed a specific narrow and intense Amide 1 peak centered at 1675 cm^{-1} which is indicative of a well-organized cross-β core.[164]

Monomers	**B-sheet (%)**	**R. Coil (%)**	**Fibril Twist**	***d* (nm)**	**θ (^{0})**	**Periodicity *v* (nm)**
40	90.9	9.1	3.78 ± 2.21	0.493	1.07	165.9
80	85.9	14.1	8.54 ± 3.47	0.501	1.21	149.1
100	89.6	10.4	11.02 ± 3.51	0.492	1.11	159.6
120	91.0	9.0	10.46 ± 3.94	0.491	1.08	163.7
140	89.6	10.4	11.97 ± 4.45	0.490	1.07	164.9
160	88.3	11.7	10.37 ± 3.48	0.495	1.03	173.0
200	89.4	10.6	19.14 ± 5.31	0.490	1.34	131.6

Table 4.2: Secondary structure analysis of Aβ42 fibrils where N=40 to N=200. Fibril twist calculated from MD simulations. This value represents the twist angle from one end of the fibril to the other. *d*, θ denote the inter-strand distance and twist angles between adjacent monomers, respectively. Length of the fibril, $L=n\times d$, where *n* is the number of monomer layers in an amyloid fibril.

The Amide 1 vibration consisting of mainly carbonyl stretching and small contributions for out-of-phase C-N stretching is known to be sensitive to the peptide's secondary structure.[165] Smaller fibrils which were less than 20 monomers in length produced overall twists less than 1^0 whereas fibrils formed by a greater number of monomers ($\geq$ 40 monomers) possess a overall twist greater than 8^0.[98] The greater overall twist is likely due to repulsive energies that arise from negatively charged monomers during aggregation (Figure 4.4). In order to minimize this repulsive energy, the monomer units adopt a staggered conformation that persists through the fibril creating an overall twist in structure (Figure 4.4).[98] This twist also helps stabilize the secondary structure and allows for reordering to occur before the fibril ruptures beyond repair, thus increasing the flexibility under no loss of strength.[98] The inter-strand distance (*d*) is defined as the average distance between monomer units within the fibril structure. The calculated *d* value for larger fibril structures (40-120) produced an average value of 0.480 ± 0.0015 nm for Aβ40 and 0.494 ± 0.0036 nm for Aβ42 (Tables 4.1 and 4.2). These values are in excellent agreement with previous experimental studies on Aβ40 and Aβ42, where values of 0.47[166] and 0.50 nm[167] were obtained, respectively. Furthermore, the interstrand distance and angle between adjacent monomers can be used to calculate the periodicity of these aggregates. The minimal length to cover a twist angle of 360^0 is driven by a balance of mechanical forces dominated by elasticity and electrostatic forces due to the distribution of hydrophobic regions and charges along the backbone.[45, 168-170] However, the periodicity does depend on the environment such that at high and low salinities they form relaxed tapes and twisted structures respectively, and has been shown to be quite tunable by Adamcik and coworkers.[171] The average computed value for the periodicity of Aβ40 and Aβ42 was 125.2 ± 7.8 and 158.3 ±12.8 nm, respectively which is in line with an experimental determined value for amyloidgenic protofibrils such as 3-fold Aβ40 fibrils of 120 ± 20 nm[45] and α-synuclein fibrils of 100-150 nm[166]. All of the geometric parameters suggest that the equilibrated structures of the larger aggregates are realistic models for both Aβ40 and Aβ42 fibrils that are hundreds of nanometers to micrometers in size (Tables 4.1 and 4.2).[172]

4.3. Mechanical Properties of Aβ40/42 Fibrils

Mechanical properties were calculated for a variety of Aβ40 and Aβ42 fibrils using a two-step approach. Where in the first step, molecular dynamics simulations were carried out on a variety of fibrils $(A\beta40/42)_n$ where n = 5, 6, 7, 8, 9, 10, 12, 15, 20, 25, 30, 40, 50, 60, 80, 100, 120, 140, 160, 200 which allowed for the solid state NMR structures to relax to a steady state within an explicit aqueous environment. All equilibrated structures reached a steady state within a 50-100 nanosecond simulation window, validated by RMSD calculations. An explicit solvent environment has been used because it affects the specific solvation and dynamics of unfolded peptides and proteins, while conformational behavior and flexibility of folded peptides and proteins remain intact.[173] The initial structures were placed in cubic boxes with similar dimensions within x and y axis (8 x 7 nm) with length variations within the z axis (5-100 nm). In order to solvate the protein there is a need to accurately model a continuum of water molecules that mimic bulk solvent effects present in many biological systems. This is ensured by using periodic boundary conditions within our simulations which replicates the simulation box in all dimensions. In the second step, stress strain calculations were performed in Materials Studio 7.0[174] utilizing two separate approaches for Aβ40 and Aβ42 fibrils. For Aβ40 fibrils, a script written in Perl language was used which applies a strain in one direction (axial or equatorial) and computes the stress within the system in kcal/mol/Å. Before any strain can be applied, the structures taking from molecular dynamics trajectories is geometrically optimized at a fine quality using force field COMPASSII[175] with maximum iterations set to 5000-500000. Force energies could not be accurately calculated if the convergence criteria were not met therefore a range of iterations were chosen with respect to those criteria. Furthermore, smaller structures had problems with convergence and were run through a series of geometric optimizations before stress-strain calculations could be performed (coarse, medium, and fine), highlighting their instability compared to the larger fibrils. The stretch script provided froze all atoms below the 10th and above the 90th percentile in their X coordinates (roughly 10-20% of the fibril). Then a strain pattern was applied. The strain pattern began at 0.001 and finished at 0.03 in which a strain value of 0.001 meant that all X coordinates were multiplied by 1.001 or the fibril was stretched by 0.1%. Next, the fibrils were geometry optimized using the COMPASSII force field, so that unconstrained atoms are allowed to move around in order to minimize the total energy. The tensile force was calculated as the net force on the bottom constrained atoms (they get pulled in the positive direction) minus the net force on the top atoms (they get pulled in the negative direction).The strain set can be separated into two parts. A linear portion (elastic) that occurs between strain 0.001-0.01 and a polynomial portion (plastic) that extends from 0.01-0.03 where the fibril reaches maximum stress, then deforms pass its ability to regain its initial structure. The linear portion or elastic region was fit to a linear trend line, where the slope is equal to Young's modulus. The highest point within the plastic portion, where structural necking can occur, can be used to determine the ultimate tensile strength of the material. Single domain structures (one-fold geometry) were chosen for these calculations due to differences in interaction energies contributions to the overall strength of the material, with the largest contributions coming from the hydrogen boding between monomer units and the smallest energetic contributions originated from the hydrophobic interactions holding the two separate domains. Additionally, as Young's modulus values are a function of total molecular area, doubling the interaction energy by having two domains is cancelled by doubling the area (force/area). Therefore, one-fold fibril structures will produce the same results as two-fold fibrils but in half the time. A average Young's modulus value of 45.0 ± 7.5 GPa was calculated for the small (Aβ40)5 –

$(A\beta40)_{20}$ fibrils (Table 4.3 and Figure 4.5), which is slightly higher but comparable to the value of 13-42 GPa calculated for small fragments of Aβ peptides reported in a previous study.[26] The similarity in the computed Young's modulus was due to common features of the equilibrated structures where smaller fibrils $(A\beta40)_{5}$ – $(A\beta40)_{30}$ contained no appreciable twist.[98]

Monomer Units	Young's Modulus (GPa)
5	38.0
6	36.2
7	37.3
8	54.1
9	44.5
10	51.2
20	54.3
30	26.0
40	33.9
50	19.8
60	11.4
80	6.1
120	4.5

Table 4.3. Computed values of Young's modulus as a function of Aβ40 monomers.

This loss in twist could account for the increase in tensile stiffness as no rearrangement or relaxation was possible during the stress-strain calculations.[98] Typically for such fibrils, instabilities can emerge at the ends of the fibrils that reduce their stability and contribute to their rigidity and dissociation under extreme chemical conditions.[47, 98, 176] However, all fibrils modeled computationally were shorter than their helical pitches and featured significant differences in their pure tensile properties. Furthermore, for fibrils shorter than their periodicity, bending modes can occur against the cross section with the lowest moment of inertia allowing increased flexibility as shown by our larger aggregates.[168-169]

The mechanical properties of Aβ40 fibrils in implicit solvent had been computed previously which varied with length and showed that larger fibrils were more stable compared to smaller ones.[47, 177] The value of Young's modulus for (Aβ40)$_{30}$ was half the value of (Aβ40)$_{20}$ and signals the next trend seen within the larger fibrils.[98]

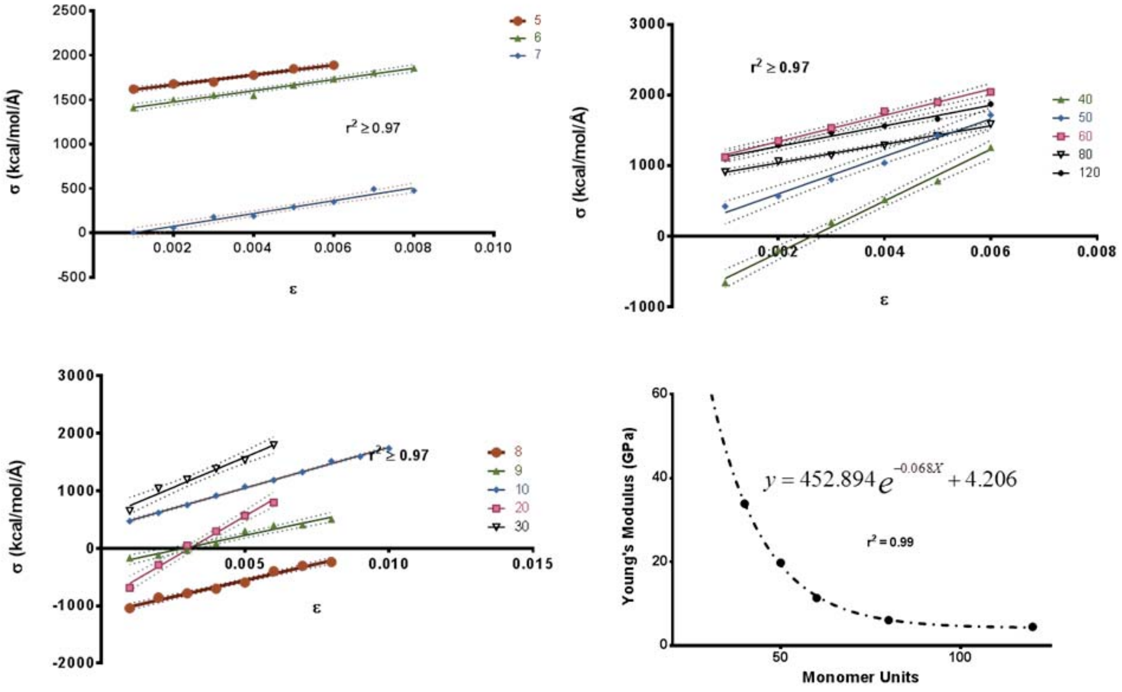

Figure 4.5. Stress-strain graphs for Aß40 fibrils comprised of 5-120 monomers in length. One-phase exponential decay comparison of larger fibril structures 40-120 showing plateau value.

For the larger fibril structures (Aβ40)$_{40}$ – (Aβ40)$_{120}$, a mono-exponential decay between the Young's modulus and the amount of monomer units was observed producing a high correlation value (0.99) indicating a scaling law might exist that could accurately calculate the lowest moduli value for much higher order aggregates.[98] The mono-exponential decay fit produced an appreciable plateau value associated with the lowest moduli that can be found for this decay (Figure 4.5). The value obtained for the plateau was 4.2 GPa, which pertains to any structure greater than 100 nm long. The calculated value of 4.5 GPa (Table 4.3) for the largest fibril should be considered in an excellent agreement with experimentally measured values of 1.79 ± 0.41 and 3.2 ± 0.8 GPa using two distinct atomic force microscopic methods.[98]

Monomer Units	**Young's Modulus (GPa)**		
	X	**Y**	**Z**
40	30.0	2.1	4.4
60	1.6	0.7	1.1
80	1.0	0.5	0.6
100	1.5	0.9	0.8
120	1.2	0.6	0.7
140	1.2	0.6	0.7
160	1.2	0.6	0.7
200	1.2	0.6	0.7

Table 4.4. Computed values of Young’s modulus as a function of Aβ42 monomers in multi-dimensions (x, y, z).

The discrepancy between the experimentally measure and theoretically calculated Young’s modulus could be due to the methods used to obtain the values. The experimentally determined values are compressive or transverse, whereas the theoretical values are purely longitudinal. In linear or longitudinal moduli, the stress and strain are related by Hook’s law where the force (F) required to lengthen or compress a spring by some distance (x) is directly proportional to that distance. Stress-strain tests exploit this law as the strain or deformation of an elastic object is proportional to the stress applied to it. This assumption is only valid for substances that produce an elastic or linear response, however has been shown that for small enough strains most solid materials exhibit Hookean behavior. Longitudinal modulus employs an iso-strain assumption where every element of the material has the same elongation. Using Transverse modulus the properties perpendicular to the fibers are examined.

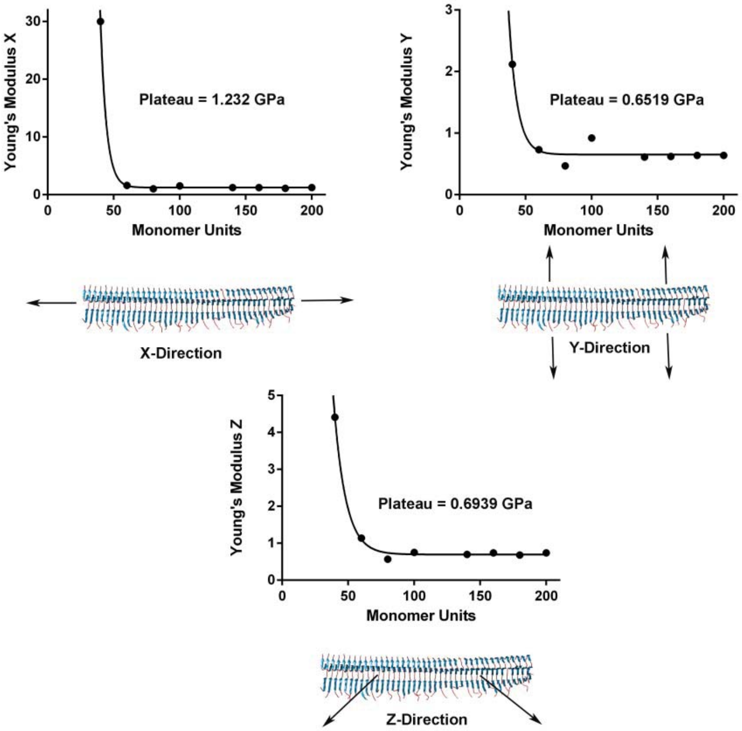

Figure 4.6. Young's modulus determined in three dimensions for the Aß42 fibrils.

Treating the individual fibers within the fibril as layers not discreet fibers is an assumption that must be made, while an even larger assumption must be made about the behavior of these fibers. As the fibers are compressed, all of the fibers condense down to a single layer that occupies the whole bottom half of the material. This assumption is made so that as a load is applied to the material, the load must first go through the matrix, then through the fibers. This allows for the load experience by the matrix to equal the load experienced by the fibers. Additionally, based on the first assumption (fibers are layers) all fibers possess the same cross-sectional area. Thus, the load and the cross-sectional area of the fibers are the same, as well as, the stress. This assumption is called iso-stress and is comparable to the iso-strain experience for longitudinal stretching.

Monomer Units	**Bulk Modulus (GPa)**	**Shear Modulus (GPa)**	**Compressibility (1/GPa)**
40	3.3	2.9	0.3
60	0.5	0.3	1.8
80	0.3	0.2	3.2
100	0.5	0.3	2.1
120	0.4	0.3	2.6
140	0.4	0.3	2.6
160	0.4	0.3	2.4
200	0.4	0.3	2.7

Table 4.5. Computed values of compressibility, bulk and shear modulus as a function of Aβ42 monomers.

These results along with the geometric parameters discussed above suggest that models of fibrils that are longer than 100 monomer units (≥60 nm) represent realistic models of mature fibrils when compared with traditional atomic force microscopy stress experiments. For Aβ42 fibrils, a different stress-strain method was developed that expanded on the current methodology. This expansion allowed for more mechanical properties to be calculated such as, bulk modulus, shear modulus, and compressibility (Table 4.5). This method applies a strain pattern as before however uses a crystal lattice refinement method that allows for simultaneous calculation of multidimensional mechanical properties (x, y, z). This was performed utilizing the Forcite module which permits fast single point energy determination and also performs geometric optimizations of molecules and periodic systems. The module uses a constrained approach, where the process starts by removing symmetry from the system followed by an optimization of the structure where cell parameters can be maintained or varied. For each configuration, a number of strains will be applied producing some strained structure that is then re-optimized for the next set of strains.

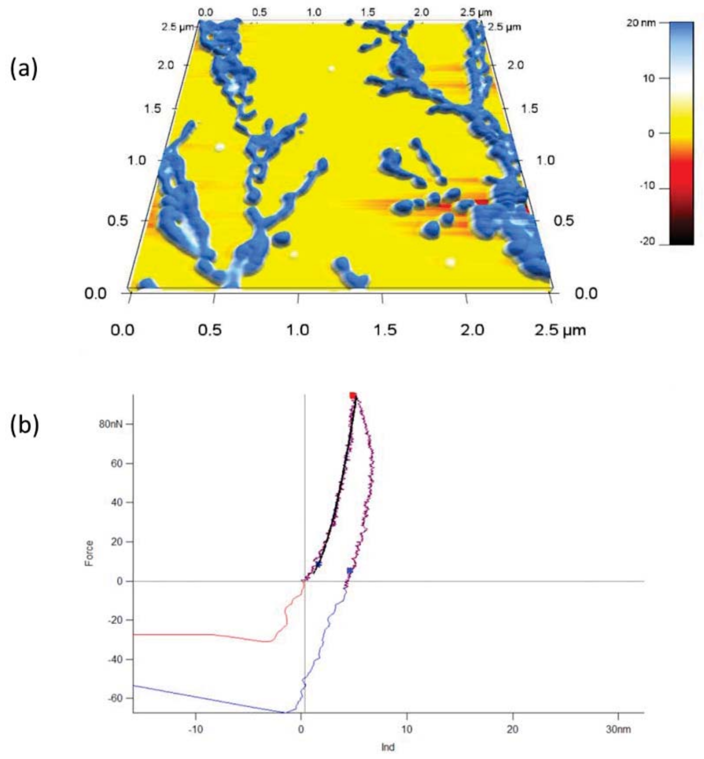

Figure 4.7. (a) Shows the AFM imaging of the Aß42 fibrils on mica and (b) is showing the experimentally obtained stress strain graph.

Each strain pattern represents a strain matrix in Voight notation and is used to generate a metric tensor G in the form of $G = HO'[2E + I]HO$, where HO is formed by the lattice vectors, E is the strain matrix, I is the identity matrix, and HO' is the transpose of HO. From G, new lattice parameters can be calculated and transformed into cell parameters followed by a stress calculation based on a stiffness matrix built up from a linear fit between the applied strain and resulting stress patterns. Any element that is acted on by an external force is said to be in a state of stress. Additionally, the stress to the body results in a change in the relative positions of the atoms within the body and can be expressed as a strain tensor matrix where elastic compliance components can be extracted and used to determine the aforementioned mechanical properties. The average Young's modulus for the larger fibrils formed from the Aβ42 peptide was 1.3 ± 0.2, 0.6 ± 0.1, and 0.8 ±0.1 GPa for the x, y, and z dimensions, respectively (Table 4.4 and Figure 4.6). This is three times more flexible when compared to the fibrils made from the Aβ40 peptide. Interestingly, the Young's modulus does change with respect to the principle axis examined and shows greater flexibility within the y and z dimensions. The average Young's modulus of 1.3 ± 0.2 GPa along the fibril's axis is in great agreement with atomic force microscopy measurements, where a value of 1.69 ± 0.17 GPa was obtained by our experimental collaborators (shown in Figure 4.7).

4.4. Summary and Conclusions

In this study, we have combined complementary experimental and theoretical techniques to investigate the structural and mechanical properties of Aβ40/42 fibrils. The atomic force microscopy experiments showed the formation of linear and unbranched Aβ40/42 fibrils with varying length (a few hundred nanometers to a few microns) and thickness (3 – 5 nm). The DUVRR spectrum provided a high relative intensity of the Amide I peak at 1675 cm^{-1} that was characteristic of β-sheet rich fibrils. The MD equilibrated fibrils, whether Aβ40 or Aβ42, formed using 5, 6, 7, 8, 9, 10, 12, 15, 20, 25, 30, 40, 50, 60, 80,100, 120, 140, 160, and 200 monomers were also dominated by β-sheets (88.0%) and formed through a zipper created by self-complementary amino acid residues. The other structural properties (twist, inter-strand distance and periodicity) of these fibrils were also in agreement with experimental measurements. The atomic force microscopy experiments provided the values of compressive Y of 1.79±0.41 GPa (sample size = 20 fibrils) in air (dry) condition. The SS calculations on the small equilibrated $(A\beta40)_5$ - $(A\beta40)_{20}$ fibrils provided an average Y value of 45.0±7.5 GPa that was significantly higher than the measured value. However, the larger structures $(A\beta40)_{40}$ - $(A\beta40)_{120}$, exhibited a mono-exponential decay and produced a high correlation value of 0.99 which suggested the existence of a scaling law. The mono-exponential decay using this law provided Y = 4.206 GPa that can be associated to any structure greater than 200 units long. This value is in excellent agreement with atomic force microscopy nanoindention experimental value of 1.8±0.41 GPa. Furthermore, stress-strain methodology was changed when considering Aß42 fibrils which produced more accurate results. The average Young's modulus of 1.3 ± 0.2 GPa along the Aß42 fibril axis is in great agreement with atomic force microscopy measurements, where a value of 1.69 ± 0.17 GPa was obtained. The results reported in this study will advance our efforts to understand sequence-structure-material properties relationship of biomaterials and to develop "design rules" for their computational modeling.

Chapter 5. Biological Systems of Molecular Recognition

Molecular recognition refers to the specific interaction between two or more molecules through noncovalent bonding such as hydrogen bonding, metal coordination, electrostatics, and hydrophobic forces. Molecular structure, recognition, and chemical properties undeniably play an import role in biological systems and the investigation of these concepts can accelerate our efforts in designing more efficient molecules for diagnostic, therapeutic, and imaging. To accomplish this aim, we have studied the molecular recognition of three complex systems: a natural enzyme glycerophosphodiesterase (GpdQ) - bis(p-nitrophenyl) phosphate, Zr^{IV}-Keggin type Polyoxometalate (ZrK) - human serum albumin (HSA), and a hybrid antimicrobial peptide ATCUN-*sh*-Buforin – DNA. Computational studies have provided the platform for quantifying and classifying these noncovalent interactions. For GpdQ, the structures of three chemically distinct phases within the catalytic cycle ($E_{m,}$ E_m-S, and E_b-S) have been determined, as well as, the influence of amino acid substitution and different substrates on active site conformation within the primary and secondary shell residues of E_b-S. Additionally, ZrK interactions at four chemically diverse sites (Arg114-Leu115, Ala257-Asp258, Lys313-Asp314, and Cys392-Glu393) within HSA have been determined and were found to be dominated by hydrogen bonding and electrostatic interactions. Furthermore, binding free energies predicted one major site (site 4) and three minor sites (sites 1, 2, 3). These complex structures were then used for mechanistic studies utilizing a quantum mechanics/molecular mechanics (QM/MM) approach where the second transition state was found to be the rate determining step with site four possessing the lowest barrier. Lastly, four forms of the antimicrobial peptide buforin

(BF2) including the ATCUN moiety were used to study its interaction with DNA. Both L- and D- forms of the peptide have been investigated as well as variable residues that make up the ATCUN portion of the peptide. The aforementioned studies have provided unprecedented insights into these complicated complex structures, molecular binding events, and chemical properties that could lead to the development of molecules with significantly increased reactivities and/or stabilities.

5.1. The Formation of the Catalytically Active Binuclear Center of Glycerophosphodiesterase (GpdQ)

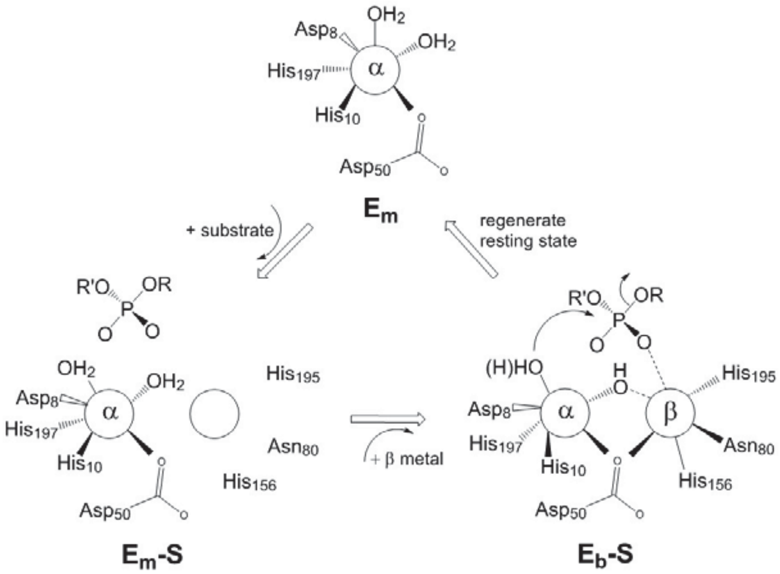

Figure 5.1. The proposed mechanism for the generation of the active binuclear $\mathbf{E_b}$**-S** species based on extensive experimental data.[178](Figure taken from ref.[97]).

Glycerophosphodiesterase (GpdQ) is a binuclear metallophosphatase that catalyzes the hydrolytic cleavage of mono-, di-, and triphosphoester bonds of a wide range of critical molecules. Upon substrate binding, this enzyme undergoes a complex transformation from an inactive mononuclear form E_m to an active binuclear center (**E_b-S**, with metals bound to both the α and β site) through a mononuclear, substrate-bound intermediate state (**E_m-S**). The proposed mechanism for the formation of the active binuclear core of GpdQ is shown in Figure 5.1. In this study, all-atom molecular dynamics (MD) simulations have been employed to investigate structures and dynamical transformations in this process using eight different variants incorporating five wild-type and three mutant forms of GpdQ. Additionally, the effects of the substrate, *bis*-(*para*-nitrophenyl) phosphate (*bp*NPP), a metal-bridging nucleophilic hydroxyl, and specific first and second coordination shell residues have been investigated. The initial binding of the substrate to **E_m** enhance the metal binding affinity of the α site and prepares the β site for coordination of the second metal ion. These results are in agreement with stopped-flow fluorescence and calorimetry data. In **E_b-S**, the computed increase in the substrate and metal (both α and β) binding energies is also in line with the experimental data. However, removal of the substrate from this complex is found to cause substantial reduction in binding energies of both α and β metals. The role of the substrate in the creation and stabilization of the active site predicted in this study is supported by the kinetic measurements using both stopped-flow and nuclear magnetic resonance (NMR) techniques. Importantly, residue Asn80, a ligand of the metal in the β site, exhibits coordination flexibility by acting as a gate in the formation of **E_b-S**, in good agreement with mutagenesis and spectroscopic data.

5.2. The Structure of the Mononuclear (E_m) Complex

The mononuclear structure (**E_m**) represents the inactive state of the enzyme. In **E_m** only the α metal site is occupied and the substrate is not present at the active site. In this state, the metal ion is directly coordinated to Asp8, His10, Asp50 and His197.

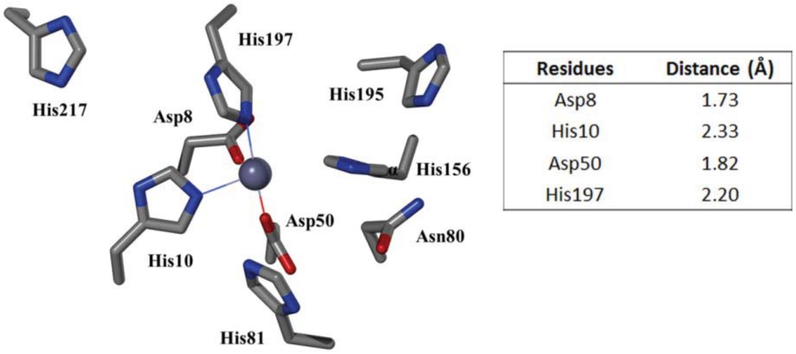

Residues	Distance (Å)
Asp8	1.73
His10	2.33
Asp50	1.82
His197	2.20

Figure 5.2. Most representative structure of the mononuclear form (**E_m**) of GpdQ from MD simulations. The (α) metal is shown in purple and coordinating distances are shown in the table.

The starting structure of this species for MD simulations was obtained by removing both the substrate and the metal in the β site from the X-ray structure of GpdQ (PDB ID: 3D03).[179] The most representative structure derived from this simulation is shown in Figure 5.2. In this structure all of the first shell residues (Asp8, His10, Asp50 and His197) remained coordinated to the metal in the α site at distances of 1.73, 2.33, 1.82 and 2.20 Å, respectively. Additionally, two water molecules interacted with this metal ion but are not shown in the figure. These waters could serve as the bridging hydroxyl and terminal nucleophile which are required for phosphoester cleavage. In **E_m** the largest fluctuations were observed within Asp50 that shifted and associated with the metal in the α site. This is not surprising as there is no metal present in the β site to interact with this residue. In this structure, another flexible first shell residue, Asn80, remains exposed to the solvent in what looks like an open conformation (Figure 5.2). The flexible nature of Asn80 is not unexpected since experimental data have demonstrated that it is a key residue for the binding of the metal in the β site to form the enzyme-substrate complex.[178-179] The second coordination shell residues His81 and His217 that facilitate the positioning of the substrate and the coordination of the metal in the β site through an extensive hydrogen bond network surround the metal in the α site in this resting state structure. The contact maps show that His81 is positioned closer to the metal in the α site (~4.5 Å) than His217 (≥5.0 Å; Figure 5.4a). Lastly, together with Asp50 and Asn80, His156 and His195 define the β metal site in a rather open conformation.

5.3. The Structure of the Substrate Bound Mononuclear ($\mathbf{E_m}$-S) Complex

The binding of the substrate *bp*NPP to the $\mathbf{E_m}$ species generates a mononuclear enzyme-substrate ($\mathbf{E_m}$**-S**) complex. The most representative structure obtained from MD simulation shows that *bp*NPP replaces a water molecule that bound to the metal in the α site in $\mathbf{E_m}$ (Figure 5.3). The substrate monodentately coordinates to the metal in the α site at a distance of 1.92 Å. Binding energy calculations indicate the formation of a stable complex with a binding energy of -13.9 kcal/mol (Table 5.1). Amino acids (Asp8, His10, Asp50 and His197) and one water ligand remained bound to the metal ion and complete the first coordination shell. However, there are some conformational changes observed in the active site due to the binding of the substrate. In comparison to $\mathbf{E_m}$ the four amino acid ligands in $\mathbf{E_m}$**-S** are bound more strongly to the metal in the α site, supported by shorter bond distances (Figure 5.2 and 5.3). Binding energy calculations indicate strong binding of the metal to the α site (-93.0 kcal/mol). In particular, the bond distance involving His10 has decreased substantially (by 0.11 Å) as the substrate exerts a slight crowding effect on the active site [Residue Index (RI) (2,10) transition from dark blue to light green in Figure 5.4b].

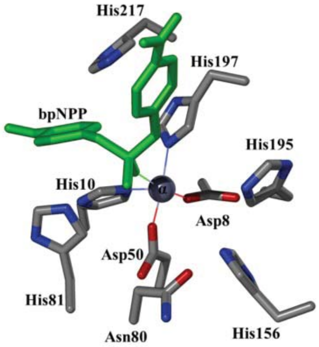

Residues	Distance (Å)
Asp8	1.78
His10	2.22
Asp50	1.80
His197	2.16
*bp*NPP	1.92

Figure 5.3. Most representative structure of the mononuclear substrate bound form (E_m-S) of GpdQ from MD simulations. The (α) metal is shown in purple, while the substrate *bp*NPP in green. The coordinating distances are provided in the table

The enhanced metal affinity of the substrate-bound complex is in agreement with a recent isothermal titration calorimetry study that demonstrated a considerable reduction in the K_d value of the metal upon the addition of the reactant.[180] Another significant change upon substrate binding is apparent in the position of residue Asn80, which shifted further away from the metal in the α site by roughly ~1.0 Å; its side chain rotates to accommodate the binding of a metal to the β site [RI (4,10) in Figure 5.4b]. Key second coordination shell residues, His81 and His217, condense around the metal-bound substrate molecule. They form weak interactions (CH-π and π-π) with the aromatic ring of the substrate and stabilize its position within the active site (Figure 5.3). Additionally, residue Arg12 (not shown) also provides a further stabilization of the substrate's position through a hydrogen bond (2.91 Å) between its terminal guanidinium group and the nitro group of *bp*NPP. In comparison to the substrate-free mononuclear enzyme, residue His195 rotated closer to Asn80, pre-shaping ("priming") the binding pocket for the second metal ion [RI (7,4) transition from light blue to a dark green color in Figure 5.4b].

Complex	ΔE_{vdW}	ΔE_{elec}	ΔG_{polar}	$\Delta G_{nonpolar}$	$\Delta G_{binding}$
$\mathbf{E_m\text{-}S}$	-11.9	-30.5	30.7	-2.2	-13.9 ± 8.0
$\mathbf{E_b\text{-}S}$	2.9	-81.9	48.8	-1.7	-31.9 ± 5.2
$\mathbf{E_b\text{-}S^{-H}}$	-5.3	-116.1	71.0	-2.1	-52.6 ± 7.1
$\mathbf{E_b\text{-}S_{H81\text{-}A}}$	6.2	-88.7	50.8	-1.5	-33.2 ± 4.5
$\mathbf{E_b\text{-}S_{H217\text{-}A}}$	3.8	-87.1	49.8	-1.5	-35.0 ± 4.1
$\mathbf{E_b\text{-}S_{N80\text{-}A}}$	3.4	-92.9	62.8	-1.6	-28.3 ± 3.5

Table 5.1. Binding energies of the substrate *bp*NPP obtained from molecular dynamics production trajectories. The energies are in kilocalories per mol.

In summary, in this initial phase of the reaction cycle substrate binding enhances the metal affinity of the α site (computed enhancement of 20.0 kcal/mol) while priming the β site for binding of a metal ion. This is in good agreement with stopped-flow fluorescence data that demonstrated that in a rapid initial phase of the catalytic cycle (k_{obs} ~350 s^{-1}) a "primed" $\mathbf{E_m\text{-}S}$ complex is formed, that has enhanced metal affinity.[178] Furthermore, from calorimetry experiments an enhancement of the metal affinity in the presence of a substrate mimic was demonstrated.[180]

5.4. The Structure of the Catalytic Binuclear (E_b-S) Complex

In the last stage of the catalytic cycle the binding of a metal ion to the β site in $\mathbf{E_m\text{-}S}$ (k_{obs} ~40 s^{-1})[178] generates a catalytically active binuclear complex ($\mathbf{E_b\text{-}S}$). The most representative structure of **E_b-S** derived from MD simulation indicates that the binuclear core [(Asp8, His10, His197)(α)-(β)(Asp50, Asn80, His156, His195)] of this complex is held together by a bridging hydroxyl ion and the substrate, which forms a μ-1,3 bidentate complex with the metals (Figure 5.5).

Complex	**ΔE_{vdW}**	**ΔE_{elec}**	**ΔG_{polar}**	**$\Delta G_{nonpolar}$**	**$\Delta G_{binding}$**
$E_{m\alpha}$	19.2	-320.3	228.9	-0.8	-73.0 ± 12.5
E_m-S_α	18.9	-353.8	242.7	-0.8	-93.0 ± 4.6
E_b-S_α	31.9	-537.1	324.1	-0.9	-182.0 ± 6.9
E_b-S_β	28.6	-526.3	306.3	-0.8	-192.2 ± 5.4
$E_{b\alpha}$	25.3	-495.2	337.3	-0.9	-133.5 ± 3.4
$E_{b\beta}$	34.2	-521.2	314.3	-0.8	-173.5 ± 7.4
E_b-S^{-H}_α	15.5	-329.4	238.6	-0.8	-76.2 ± 3.5
E_b-S^{-H}_β	23.2	-379.7	240.8	-0.8	-116.6 ± 3.3
E_b-$S_{H81\text{-}A\text{-}\alpha}$	30.3	-531.4	320.9	-0.8	-181.0 ± 6.0
E_b-$S_{H81\text{-}A\text{-}\beta}$	26.4	-517.7	299.8	-0.9	-192.4 ± 7.0
E_b-$S_{H217\text{-}A\text{-}\alpha}$	30.4	-524.7	314.8	-0.9	-180.4 ± 7.9
E_b-$S_{H217\text{-}A\text{-}\beta}$	27.6	-516.0	302.5	-0.8	-186.7 ± 6.2
E_b-$S_{N80\text{-}A\text{-}\alpha}$	31.9	-519.0	322.2	-0.8	-165.7 ± 7.0
E_b-$S_{N80\text{-}A\text{-}\beta}$	20.7	-451.4	307.6	-0.9	-124.0 ± 15.1

Table 5.2. Comparison between binding energies of both (α) and (β) metals per complex. The energies are in kilocalories per mole.

The accuracy of the MD structures was proven by two methods; a B-factor (great overlap) and superposition (≤0.42 Å) comparison between the X-ray structure and MD obtained structure which was in excellent agreement (results not shown). In both structures all first coordination shell residues lie within bond forming distances of the metals, and the bridging hydroxyl group is positioned opposite the substrate. However, the α-β distance (3.13 Å) in the equilibrated structure is 0.56 Å shorter than the one observed in the crystal structure, which may be partially due to the difference in the identity of the substrate (*bp*NPP *vs* PO_4).[179]

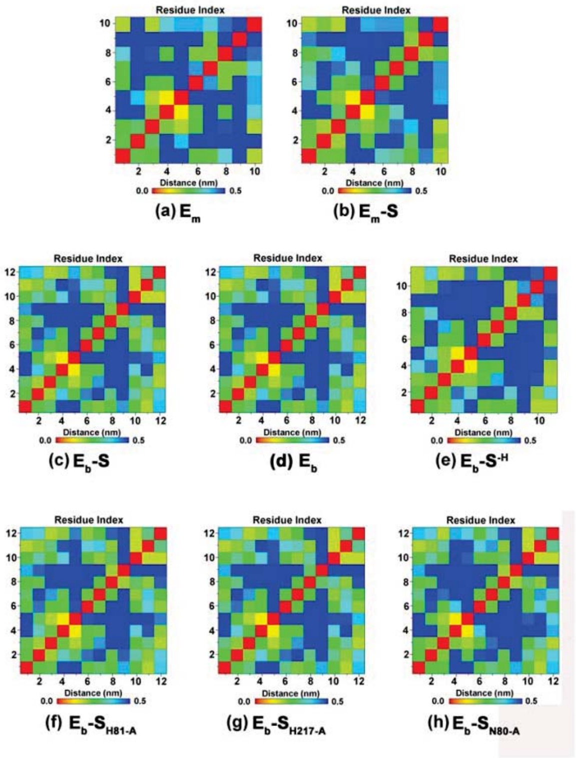

(a) E_m (b) E_m-S (c) E_b-S (d) E_b (e) E_b-S^{-H} (f) E_b-S_{H81-A} (g) E_b-S_{H217-A} (h) E_b-S_{N80-A}

Figure 5.4. Contact maps of all complexes showing only the active site and secondary shell residues. Color scale bars have been used at a range of 0 to 0.5 nm. (Taken from ref.[97])

Based on bond length the interaction of *bp*NPP is stronger with the metal in the β site than the one in the α site (1.87 Å *vs* 2.06 Å, respectively; Figure 5.5). The coordination numbers of the metals in the α and β sites are five and six, respectively (Figure 5.5). Among the first coordination shell residues, His195 is the weakest ligand (bond distance = 2.57 Å). It appears that Asn80 acts initially as a strong ligand for the metal in the β site (bond distance = 2.01 Å), thereby stabilizing the active site. However, this possible interaction may be due to the force-field that places a more negative charge on the oxygen present of the side chain of Asn80 compared to the less negative nitrogen of His195. Additionally, this Asn80 backbone carbonyl oxygen atom interacts with the side chain of Asp50 through a strong hydrogen bond at a distance of 1.91 Å.

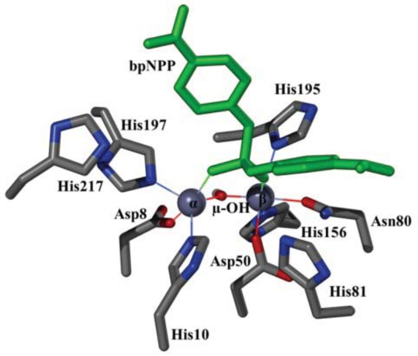

Residues	Distance (Å)
Asp8	1.83
His10	1.94
Asp50	1.89
Asn80	2.01
His156	2.23
His195	2.57
His197	2.02
bpNPP	2.06 , 1.87
μ-OH	1.68 , 1.68

Figure 5.5. Most representative structure of the active binuclear substrate bound form (**E_b-S**) of GpdQ from MD simulations. The (α) and (β) metals are shown in purple, while the substrate *bp*NPP is in green. The coordinating distances are provided in the table.

This hydrogen bonding interaction was also observed in the crystal structure of GpdQ. During the transition from **E_m-S** to **E_b-S** Asp50 switched its position so that it interacts predominantly with the metal in the β site (the M_α-O_{Asp50} and M_β-O_{Asp50} distances are 3.22 and 1.89 Å, respectively). In contrast, in the crystal structure this residue is bridging both metal ions. Again this variation may be due, at least partially, to the use of an actual substrate (*bp*NPP) in the MD simulations, contrasting the use of the smaller phosphate molecule in the crystallographic (and spectroscopic) studies.

Similar to the **E_m-S** complex the second coordination shell residue His81 stabilizes the substrate at the active site through a CH-π interaction (at a distance of 2.91 Å), but the previously observed interaction between His217 and the substrate is lost. This loss is compensated by (i) a strong hydrogen bond between the α-amino group of Gln166 and the nitro group of the substrate (2.18 Å) and (ii) a CH-π interaction between the terminal methyl group of Met167 and the aromatic ring of *bp*NPP (2.71 Å). Additionally, His81 rotated to increase its interactions with the aromatic rings of *bp*NPP (Figure 5.5). All of the changes during the **E_m-S** → **E_b-S** transition caused an enhancement by 18.0 kcal/mol in the substrate binding energy (Table 5.1). The electrostatic contribution to the binding energy has also significantly increased (by 51.4 kcal/mol). Importantly, in the **E_b-S** complex the binding energy of the α site for a metal is strongly enhanced when compared to the mononuclear complex (by 89.0 kcal/mol), while the β site also displays a strong affinity for a metal (Table 5.2), in good agreement with experimental data.[178, 180]

5.5. The Effect of the Bridging Hydroxyl Group on the Structure of the E_b-S Complex

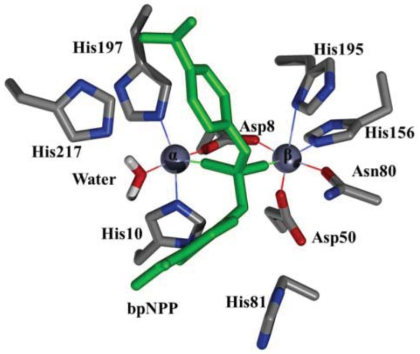

Residues	Distance (Å)
Asp8	1.73 , 1.79
His10	2.06
Asp50	1.71
Asn80	1.90
His156	2.18
His195	2.65
His197	1.92
bpNPP	1.78 , 1.83
Water	1.93

Figure 5.6. Most representative structure of the nucleophile (-OH) free form (**E_b-S^{-H}**) of **E_b-S** derived from MD simulations. The (α) and (β) metals are shown in purple, while the substrate *bp*NPP in green. The coordinating distances are provided in the table.

The hydroxyl group that bridges the metals bound to the α and β sites has been proposed to function as a nucleophile in some binuclear metallohydrolases (*e.g.* some PAPs,[181-182] organophosphate-degrading hydrolases[181, 183-184] and antibiotic-degrading metallo-β-lactamases[181, 185]), but in GpdQ it was proposed to act as a base, abstracting a proton from a water bound to the metal in the α site, activating this water for its nucleophilic attack on the substrate.[178-179] To study its effect on the structure of the **E$_b$-S** complex, MD simulations were performed on a structure (**E$_b$-S^{-H}**) without this group. In this complex the α-β distance is substantially longer than in **E$_b$-S** (3.13 Å *vs* 4.74 Å; Figure 5.6) [RI (11, 12) in Figure 5.4c and RI (10, 11) in Figure 5.4e]. Additionally, a terminal water that is not observed in **E$_b$-S** coordinates to the metal in the α site in **E$_b$-S^{-H}**, and the first coordination shell Asp8 changes its coordination mode from mono- to μ-1,3 bidentate, effectively occupying the bridging position previously held by the μ-hydroxyl group [compare RI (1,11) in Figure 5.4e and RI (1,12) in Figure 5.4c]. This significant rearrangement of Asp8 was possibly due to the absence of a steric clash with that bridging hydroxyl group. The effect of the removal of μ-OH on the bond between Asn80 and the metal in the β site (1.90 Å) is comparable to that observed upon removing the substrate, demonstrating the synergistic nature of substrate and metal binding in the active site of GpdQ. Furthermore, in comparison to **E$_b$-S**, the bonds between *bp*NPP and the two metals in **E$_b$-S^{-H}** are more symmetric and tight (relevant bond length pairs are 1.78 Å/1.83 Å and 2.06 Å/1.87 Å for **E$_b$-S^{-H}** and **E$_b$-S**, respectively; Figures 5.5 and 5.6). This symmetry also translates into a higher substrate binding energy for **E$_b$-S^{-H}** (Table 1). In contrast, the binding energies for both metals in the absence of the μ-hydroxyl group (-76.2 and -116.6 kcal/mol for the metals in the α and β sites, respectively) are strongly reduced (Table 5.2), even though their respective coordination numbers (five and six) is unaltered. The combined results observed upon removing the metal-bridging hydroxyl group demonstrate the importance of this group in the formation of a stable bimetallic, catalytically active site. Its strong interaction with the two metals is anticipated to raise its alkaline character, which enhances its efficiency to activate the α-metal-bound nucleophile. Furthermore, the presence of the μ-OH also renders the enzyme-substrate complex more labile, lowering the activation barrier of the reaction.

5.6. The Effect of the Substrate on the Structure of the E_b-S Complex

To study the effect of the addition of the substrate *bp*NPP, a simulation was run on the **E_b-S** species, where the substrate was removed. The resulting structure (**E_b** in Figure 5.7) was compared to the fully active substrate-bound complex (**E_b-S** in Figure 5.5).

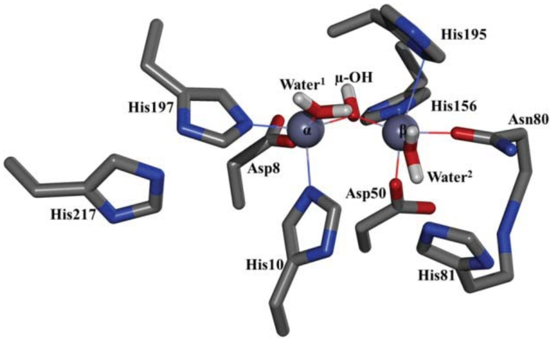

Residues	Distance (Å)
Asp8	1.85
His10	2.10
Asp50	1.82
Asn80	1.88
His156	2.10
His195	2.73
His197	1.98
$Water^1$	1.90
$Water^2$	1.98
μ-OH	1.73 , 1.70

Figure 5.7. Most representative structure of the substrate free form (**E_b**) of **E_b-S** derived from MD simulations. The (α) and (β) metals are shown in purple and the coordinating distances are provided in the table.

There are a few notable differences. Firstly, the α-ß distance is elongated in the absence of the substrate by 0.13 Å (3.27 Å), moving closer to the distance shown in the crystal structure (3.68 Å). Additionally, two terminal water molecules coordinate to the metals, replacing the substrate, while the μ-OH remains in the same position in both complexes. Of particular interest is the observation that in the absence of substrate the bond between residue Asn80 and the metal in the β site is shortened by 0.13 Å, which is in support of this residue experimentally observed coordination flexibility (see above).[178-179] The opposite movement is observed for His10 and His195, where the addition of the substrate leads to a contraction of their bond distances to the metals in the α and β sites, respectively, by 0.16 Å. However, the contact map generated for this complex did not differ greatly from the fully active form (Figure 5.4d).

Importantly, and again in good agreement with experimental data, in the absence of substrate the binding energies for both metals are significantly decreased (by 48.5 and 18.7 kcal/mol for the α and β sites, respectively; Table 5.2).[180] These results indicate that the substrate helps to stabilize several primary residues within the active site as well as the catalytically active metals, but they also demonstrate that once formed the bimetallic center does not dissociate easily in the absence of substrate. This explanation agrees with kinetic measurements using both stopped-flow[178] and NMR[181] that showed that GpdQ employs a non-processive mechanism, whereby the active site remains assembled until the substrate is depleted.

5.7. The Effects of Mutations on the Structure of the E_b-S Complex

The effects of three key residues (Asn80, His81 and His217) on the structure of the E_b-S complex were investigated using their mutant forms (*i.e.* Asn80Ala, His81Ala, and His217Ala). Asn80 was shown experimentally to play an important role in both substrate and metal binding,[186] and our computational data supports this conclusion. This residue directly coordinates to the metal in the β site and acts as a gate to block its exit. It also positions the substrate at the active site through hydrogen bonding. The Asn80Ala mutant of GpdQ, while shown to be catalytically active,[179] and is expected to have decreased affinities for both the substrate and the metal in the β site. In the structure derived from the MD simulation of this mutant (E_b-S_{N80A}) substantial alterations in the active site configuration are observed (Figure 5.8). The β metal binding site collapsed and the coordination bond between the metal in this site and His195 is broken (Figure 5.4h and 5.8). In addition, greater fluctuations are observed for the metal in this site when compared to **E$_b$-S** (Figure 5.4c and 5.4h) as it has more space to move.

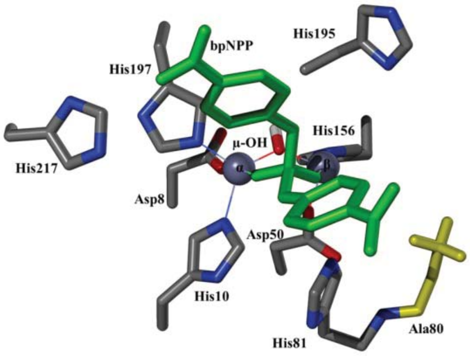

Residues	Distance (Å)
Asp8	1.79
His10	2.09
Asp50	1.80
His156	2.44
His195	4.61
His197	1.94
bpNPP	1.87 , 1.97
μ-OH	1.71 , 1.66

Figure 5.8. Most representative structure of the Asn80Ala mutant (**E$_b$-S$_{N80A}$**) of **E$_b$-S** derived from MD simulations. The (α) and (β) metals are shown in purple, the substrate *bp*NPP in green and mutation is in yellow color. The coordinating distances are provided in the table.

It is thus not surprising (and in agreement with experimental data[179]) that the substrate binding energy is reduced by 3.6 kcal/mol in this mutant. Furthermore, this mutation has a major impact on the binding energy of the metal in the β site (a reduction of nearly 70 kcal/mol), while the effect on the metal in the α site is moderate (Table 5.2). The computational data are thus in qualitative agreement with available experimental data and demonstrate that a catalytically active bimetallic center can be maintained in GpdQ, even after a ligand of one of the metals is removed. This lends credence to the coordination flexibility of Asn80, initially proposed based on mutagenesis and spectroscopic data.[179] The two second coordination shell residues His81 and His217 are part of an extensive hydrogen bond network that links the substrate binding pocket to the bimetallic catalytic center. Their replacement with Ala has little effect on the catalytic efficiency of the resulting mutants; since the respective K_m values are also not altered largely by these mutations, it appears that these residues are not crucial for substrate binding.[178]

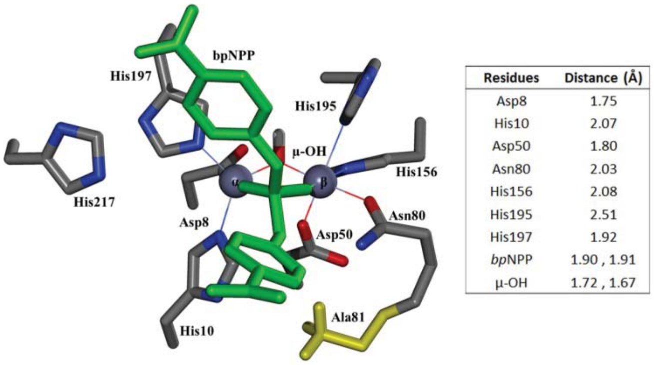

Residues	Distance (Å)
Asp8	1.75
His10	2.07
Asp50	1.80
Asn80	2.03
His156	2.08
His195	2.51
His197	1.92
*bp*NPP	1.90 , 1.91
μ-OH	1.72 , 1.67

Figure 5.9. Most representative structure of the His81Ala mutant (**E_b-S_{H81A}**) of **E_b-S** derived from MD simulations. The (α) and (β) metals are shown in purple, the substrate *bp*NPP in green and mutation is in yellow color. The coordinating distances are provided in the table.

However, an enhanced affinity in particular for the metal in the β site is observed, especially in the absence of substrate.[178] In the most equilibrated calculated structure (**E_b-S_{H81A}**) derived from the simulation of the His81Ala mutant, the interaction between the residue Ala81 and the substrate is broken and the side chain is moved away from the binuclear metal center (Figure 5.9). However, the overall configuration of the active site is not greatly affected by this mutation (Figure 5.4f); the rmsd value obtained from a superposition of this and the crystal structure is low (0.40 Å). In agreement with the experimental data the substrate binding energy in this mutant is very similar (slightly enhanced) to that of the wild-type enzyme (Table 5.1). Furthermore, the metal affinity for both binding sites is virtually identical to that of **E_b-S** (Table 5.2). The mutation of His217 to Ala produced similar effects and active site coordination compared to His81 to

Ala as shown by the contact maps (Figure 5.4f and 5.4g). In this case, the non-bonding interaction energy shows an increase of 3.1 kcal/mol. The equilibrated structure (**E_b-S_{H217A}**) obtained from this simulation is shown in Figure 5.10.

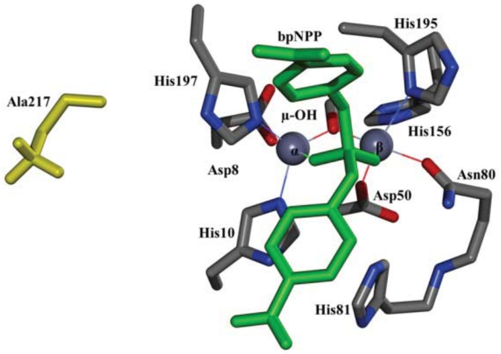

Residues	Distance (Å)
Asp8	1.82
His10	2.07
Asp50	1.86
Asn80	1.98
His156	2.09
His195	2.55
His197	1.85
*bp*NPP	1.94 , 1.95
μ-OH	1.71 , 1.69

Figure 5.10. Most representative structure of the His217Ala mutant (**E_b-S_{H217A}**) of **E_b-S** derived from MD simulations. The (α) and (β) metals are shown in purple, the substrate *bp*NPP in green and mutation is in yellow color. The coordinating distances are provided in the table.

The electrostatic energy contribution for both mutants shows a minor increase and may be attributed to a slight decrease in the size of the binding pocket. It is also apparent that interactions that were lost due to mutation of these two residues are largely compensated by other residues in the proximity of the active site. The mutation of His81 to Ala enables the amine group of the primary shell residue Asn80 to form a hydrogen bond with the substrate at a distance of 1.94 Å. The His217 to Ala mutation allows for Tyr19 to move closer to the substrate to form a Π-Π interaction with the aromatic group of *bp*NPP at a distance of 3.36 Å.

5.8 Summary and Conclusions

GpdQ is an unusual metallohydrolase that requires the addition of a substrate in order to form a catalytically active binuclear metal center.[178-179, 187] Furthermore, upon forming a bimetallic center conformational changes in the active site alter the coordination environment of the metal in the β site (illustrated by the flexibility of ligand Asn80) and enhance the reactivity further. The purpose of this study was the development of a computational methodology to probe this mechanism with a view to designing specific modifications (mutations) that may lead to desired alterations of the enzyme's catalytic properties (*e.g.* improving its catalytic rate, enhancing its stability). In our MD simulations we focused on the initial stage of the catalytic cycle, *i.e.* the transformation of a catalytically inactive mononuclear form to a fully active bimetallic one. We considered the role of the substrate in this transition, as well as that of the proposed nucleophile of the reaction, *i.e.* the metal-bridging hydroxide group. Overall we observed a good agreement between the simulated processes and those proposed based on experimental data.

In the resting state the inactive mononuclear system ($\mathbf{E_m}$) has a Zn(II) bound to the α site; the metal-free β site is rather exposed to the solvent in an open conformation (Figure 5.2). The coordination of the substrate *bp*NPP to the metal ion of $\mathbf{E_m}$ significantly alters the active site and generates the $\mathbf{E_m}$**-S** species (Figure 5.3). Furthermore, the addition of the substrate enhances the bonding interaction between the metal and all of its four amino acid ligands (*i.e.* Asp8, His10, Asp50 and His197). Importantly, substrate binding also induces a shift of the gating residue Asn80 further away from the α site, a move that is accompanied by a reorientation of its side chain to facilitate coordination with a metal in the β site. Thus, the addition of *bp*NPP effectively primes the active site for the formation of a catalytically essential bimetallic center. In $\mathbf{E_b}$**-S**, *bp*NPP adopts a metal-bridging μ-1,3 coordination mode. Importantly, in the presence of substrate the affinity of the metal in the α site is significantly enhanced (the binding free energy doubles from ~-90 kcal/mol to ~-180 kcal/mol; Table 5.2), which follows the trend observed in calorimetric[180] and spectroscopic[178] measurements.

The calculations also support the role of the metal-bridging hydroxide as the activator of the hydrolysis-initiating nucleophile. *In silico* removal of this μ-OH group leads to a significant expansion of the metal-metal distance and the formation of a more symmetric enzyme-substrate complex (Figure 5.6). These observations indicate that the μ-hydroxide interacts strongly with both metals, a process that greatly enhances its basic character and thus its ability to act as an efficient promoter of the hydrolytic reaction. Furthermore, by imposing a less symmetric and hence more strained conformation on the enzyme-substrate complex a reduction of the activation barrier is achieved.

The calculations also successfully demonstrated the importance of residues Asn80, His81 and His217 in the mechanism of GpdQ. Some discrepancies, however, between experimental and theoretical studies ought to be noted. The calculations have not reproduced the full coordination flexibility of Asn80, a process that is relevant for the enzyme to obtain its catalytically most efficient conformation.[178] It is likely that the discrepancy between the experimental and theoretical extent of flexibility at this site is linked to the position of residue Asp50. In a future study our efforts will focus on factors that guide the movements of this residue. The outcomes of our studies are encouraging as they provide the first theoretical approach to successfully recreate various aspects of a complex hydrolytic reaction carried out by an enzyme that employs an intricate regulatory mechanism of action.

5.9. The Investigation of Polyoxometalate-HSA Interactions at Chemically Distinct Binding Sites

Polyoxometalates (POMs) are a versatile class of metal-oxygen clusters that utilize their molecular properties like charge, oxidation state, ligand environment, and photochemical characteristics in diverse fields such as catalysis, materials science, and analytical chemistry.[188-190,191-198] Due to their specificity towards different biomolecules, they also exhibit antiviral[199], antitumoral[200], antibacterial[201], and anticancer activities[202]. Additionally, they have also been used in ribosomal crystallography[203] and for the inhibition of HIV reverse transcriptase[204] and HIV protease activity[199].

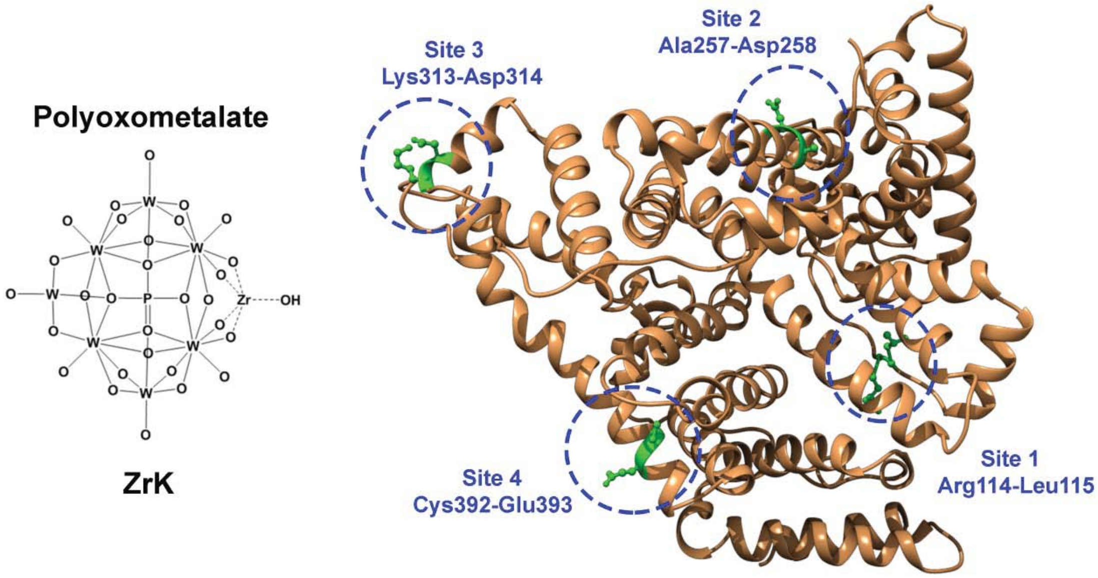

Figure 5.11. Structure of ZrK and HSA with all four cleavage sites labeled. The peptide bond is highlighted in green with connecting residues labeled.

Furthermore, as a hydrolytic agent, Ce(IV) and Zr(IV)-substituted POMs have been reported to hydrolyze multiple peptide bonds of critical biomolecules including human serum albumin (HSA),[188, 205] hen egg-white lysozyme (HEWL)[206], myoglobin[1], amyloid beta peptides (Aß)[207] and basic fibroblast growth factor (bBGF)[208]. From western blot and subsequent NH_2-terminal Edman degradation analysis, four distinct cleavage sites (Arg114-Leu115, Ala257-Asp258, Lys313-Asp314, and Cys392-Glu393) located in different regions of HSA were identified (Figure 5.11).[188] ZrK was quite versatile and unlike most natural proteases, in a rather non-preferential manner, it cleaved a variety of peptide bonds formed by chemically diverse amino acid residues i.e. polar charged (Arg, Asp and Glu) and nonpolar (Leu, Ala and Cys). Cleavage site 1 (Arg114-Leu115) was located in the central cleft of HSA within a positive inner surface. The width of the cleft was reported to be roughly 1 nm in size, which was quite comparable to the size of ZrK. Site 1, as in all sites, was flanked by a positively charged surface patch, which could facilitate interactions with the negatively charged groups of ZrK.[188] The remaining cleavage sites Ala257-Asp258, Lys313-Asp314, and Cys392-Glu393 of HSA occurred upstream from negatively charged Asp or Glu residues suggesting that there could also be a possible electrostatic interaction with the positively charged Zr(IV) or W ions of ZrK. However, the hydrolysis requires coordination of the carbonyl oxygen of the peptide bond to the Zr(IV) ion and from experiments, a weak ionic interaction rather than true coordination was suggested.[188] Interestingly, it appears that charge plays a larger role in binding of ZrK to HSA as an increase in negative charge of this metal cluster resulted in increased reactivity, while the addition of more of Zr(IV) ions in its framework showed no apparent change.[188]

In the absence of X-ray structures of the POM-HSA complexes, the physicochemical nature of their interactions at multiple cleavage sites are not known. The understanding of these interactions at the atomistic level is required for utilization of POMs in a variety of biochemical, biotechnological, and medical applications. In this aspect, molecular dynamics (MD) simulations can provide structural information and elucidate the nature of POM-HSA interactions. Recently, this technique was successfully utilized to explore association of HEWL with a variety of Ce(IV) and Zr(IV) substituted POMs.[209] However, to the best of our knowledge, interactions of a single POM with multiple chemically distinct cleavage sites of a protein have thus far not been investigated. Furthermore, changes in the secondary structure of protein after the binding of POM and its hydrolysis are not known.

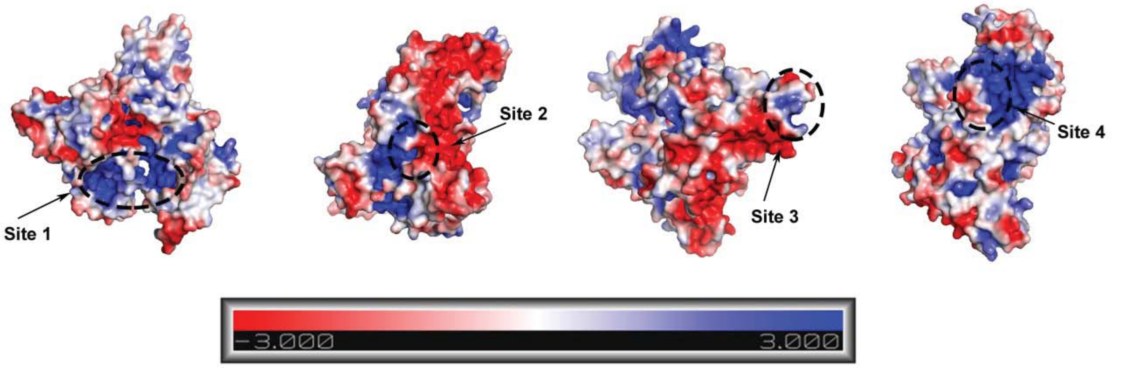

Figure 5.12. Electrostatic potential maps of HSA showing all four site of cleavage.

In this study, we have employed all-atom MD simulations using ZrK and HSA as models to address all these unresolved issues. The results are compared with the available experimental data. Our simulations will provide structures of ZrK-HSA complexes at all four chemically distinct cleavage sites and elucidate their specificities. They will also help to elucidate roles of dynamics, specific amino acid residues, solvent, charge distributions, secondary structures, and binding affinities in POM-proteins interactions. Furthermore, they will contribute to design the next generation of POMs with enzyme-like activities.

5.10. ZrK-HSA Interactions at Site 1 (Arg114-Leu115)

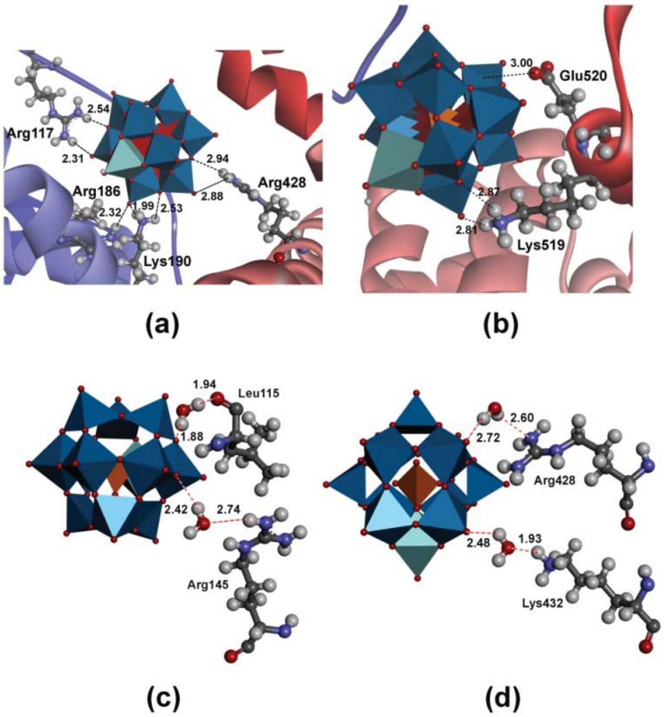

(a) (b)

(c) (d)

Figure 5.13. Most representative structure of POMs-HSA at site 1 obtained from molecular dynamics simulations. (a) and (b) are zoomed in images of binding site 1 with amino acid residues and interaction distances labeled in Å. In the POMs structure, the orange polyhedron represents the interior phosphate group, the dark blue polyhedron represent the octahedron geometry around the tungsten, while the light blue represents the Zr(IV) species. (c) and (d) are showing water mediated interactions with the oxygen of ZrK, hydrogen bonding interacting distances labeled in Å.

The first cleavage site (Arg114-Leu115, site 1) was formed by a positively charged (Arg) and a nonpolar (Leu) residue. This site was a part of a random coil section on the surface of HSA that showed little to no secondary structure (Figure 5.11). The electrostatic potential map (Figure 5.12), suggested two positively charged regions on either side of the peptide bond. Thus, both rigid and flexible docking of ZrK around this site provided two possible binding motifs.

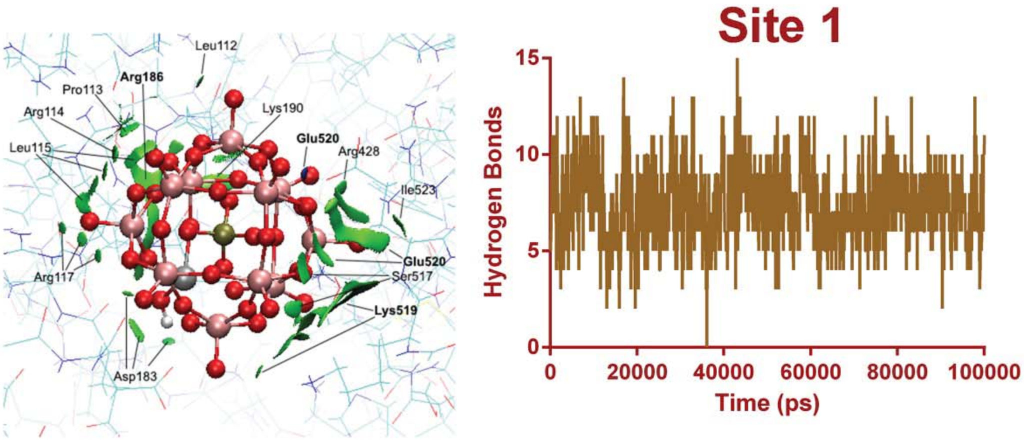

Figure 5.14. Noncovalent interaction plots and hydrogen bonding interactions at site 1

The first motif included two positive residues Arg114 and Lys137 of HSA that were present on the exterior surface of the cleavage site. The stability of this site was tested through MD simulations. There were no ZrK-HSA interactions at this site throughout the MD trajectory and the overall non-bonding energies were very small. However, during the simulation, ZrK moved down to a more hydrophobic cleft formed by the Val120-Lys137 region. The second binding motif from the docking procedure was found on the opposite side of site 1. It was located on the interior of the cleavage site, where a large pocket surrounded by many positively charged residues allowed for binding of a negatively charged ZrK. Given the flexible nature of random coil sections, this site was easily accessible for the binding of ZrK. It was stabilized by host of hydrogen bonding and electrostatic interactions from both negatively and positively charged amino acid residues of HSA. These types of interactions have been previously proposed to drive association of POMs with biomolecules.[210-212] For instance, Arg117, Arg186, and Arg428 formed multiple hydrogen bonds through interactions between their amine protons and the negatively charged oxygen cage of ZrK (Figure 5.13c).

Position	**Hydrogen Bonds**	**$\Delta G_{Binding}$**
Site 1	7	-57.5 ± 11.7
Site 2	3	-24.2 ± 11.9
Site 3	3	-50.8 ± 11.3
Site 4	8	-91.2 ± 10.8

Table 5.3. Free energy change of the complexation of the ligand and receptor (kJ/mol).

Additionally, positively charged Lys190 and Lys519 residues associated through hydrogen bonding with the surface of ZrK (Figure 5.13c and 5.13d). The negatively charged surface of ZrK preferred positive patches along the protein surface and readily bound to these sections even in the presence of negatively charged residues. These negatively charged residues should in theory repel the ZrK from binding however; here the repulsion is overcome by greater attractive electrostatic interactions within this site. Negatively charged residues such as; Asp and Glu (particularly Glu520) did show minor interactions with the positive charge of the W metals of the cage, but they were very weak (~10 kJ/mol) and low in number as the negatively charged oxygen atoms dominated the structure (Figure 5.13b). The NCI contour plots that show relative abundance and strength of the noncovalent interactions also highlighted Lys519, Glu520, and Arg186 as the main interacting residues at this site (Figure 5.14). At this site, ZrK was found to form an average of 7 direct hydrogen bonds with HSA (Figure 5.14). Additionally, there were multiple hydrogen bonding interactions mediated by 1-3 solvent water molecules. The key interactions promoted by one water molecule are shown in Figures 5.14c and 5.14d. In particular, the backbone of Leu115 and sidechain of Arg145 associated with Zrk through one water molecule (Figure 5.14c). The side chains of Arg428 and Lys432 also exhibited similar interactions. The catalytically important Zr-OH moiety was positioned on the interior of the protein close to this cleavage site, however, was still exposed to water through the bottom channel opening. It was in the direct vicinity of a positively charged Lys190 residue. The binding free energy of this site was -57.5 kJ/mol (Table 5.3). The binding of HSA to another Kegging type POM [H2W12] was also shown to be exothermic (ΔH = -50 kJ/mol) by isothermal calorimetry (ITC) experiments.[213] The strong exothermicity of this process also suggests that these interactions are dominated by electrostatic interactions.[213] The binding of ZrK to HSA at site 1 was not observed to alter its secondary structure, which was dominated by α-helical conformation (67%), Table 5.4. Additionally, this interaction had no effect on the overall structure of HSA and the RMSD with the ZrK free structure was only 1.16 Å. The binding of H2W12 POM also did not change the secondary structure of the HSA.[214] Furthermore, the overall secondary structure of HSA was found to be quite stable and did not alter upon the hydrolysis of site 1 both in the presence and absence of ZrK.

5.11. ZrK-HSA Interactions at Site 2 (Ala257-Asp258)

The second cleavage site (Ala257-Asp258, site 2) was formed by a nonpolar (Ala) and a negatively charged (Asp) residue. This site was located 34.5 Å away from site 1. It was sandwiched between two parts of a well folded section of HSA in which alpha helical secondary structure dominated (Figure 5.11). Furthermore, this site was flanked by a large positively charged region that could offer stability for binding of ZrK to the HSA's surface (Figure 5.12).

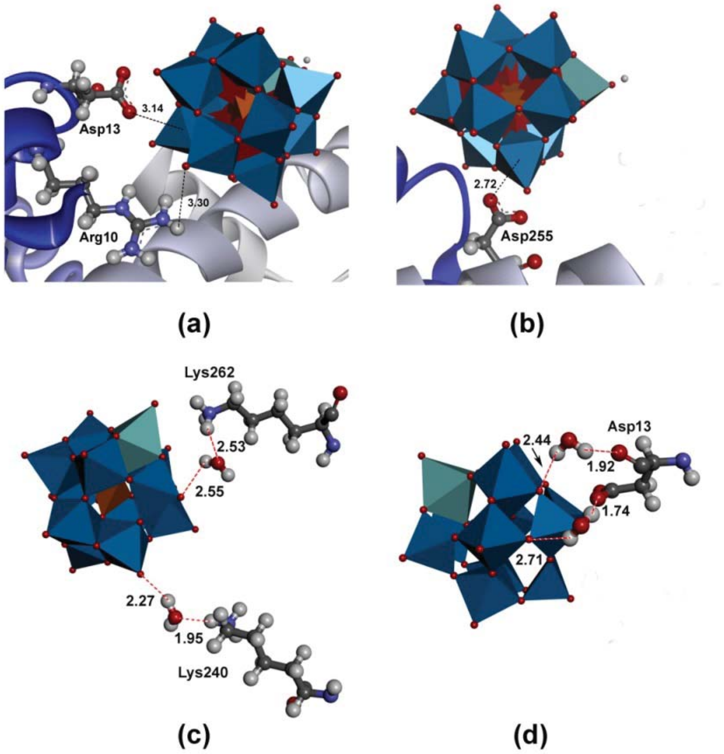

Figure 5.15. Most representative structure of POMs-HSA at site 2 obtained from molecular dynamics simulations. (a) and (b) are zoomed in images of binding site 2 with amino acid residues and interaction distances labeled in Å. (c) and (d) are showing water mediated interactions with the oxygen of ZrK, hydrogen bonding interacting distances labeled in Å.

Both negative and positive amino acid residues stabilize this site through electrostatic and hydrogen bonding interactions. Unlike site 1, the docking procedure (both rigid and flexible) around this site provided only one binding motif that was used as the starting point in the subsequent MD simulations. The most representative structure derived from MD simulations is shown in Figure 5.15a and 5.15b. At the binding site, negatively charged residues Asp13 and Asp255 interacted with the metals present within the cage of ZrK at distances of 3.14 and 2.72 Å, respectively (Figure 5.15a and 5.15b). Interestingly, both Asp13 and Asp255 associated in a monodentate fashion to the W metal. These interactions with ZrK remained intact throughout the trajectory.

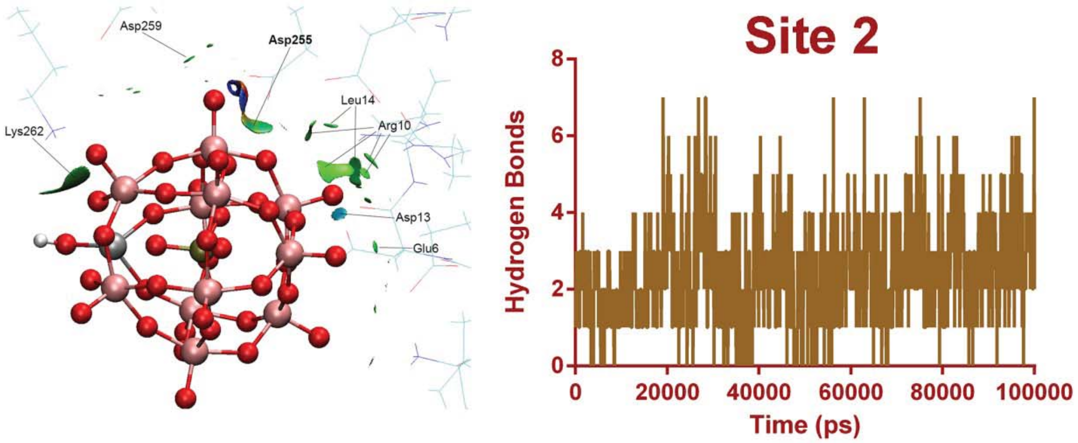

Figure 5.16. Noncovalent interaction plots and hydrogen bonding interactions at site 2

On the other hand, only one positively charged residues, Arg10, associated with ZrK through hydrogen bonding (Figure 5.15a). The amine group of Arg10 interacted with the oxygen cage of ZrK through weak hydrogen bonds. NCI contour plots also showed moderate interactions originating from the Asp255 and Arg10 residues (Figure 5.16). Periodically Lys262 formed weak hydrogen bonds with the oxygen atoms of ZrK during the simulations, however this was infrequent and not observed in the clustered result. In comparison to site 1, at this site ZrK formed a much smaller number of direct hydrogen bonds, on average 3, with HSA (Figure 5.16). Among water mediated hydrogen bonds, the side chains of Lys240 and Lys262 interacted through one water molecule (Figure

5.15c). On the other hand, both side chain and backbone of Asp13 formed hydrogen bonds with the cage of Zrk (Figure 5.15d). Unlike site 1, here the Zr-OH moiety was flipped out and exposed to the solvent positioned perpendicular to the cleavage site. As a result of these weak and fewer interactions, the binding free energy (24.2 kJ/mol, Table 5.3) for this site was substantially higher than the one (57.5 kJ/mol) computed for site 1. The association of POM to this site slightly (1%) increased the α-helical content (69%) of HSA in comparison to site 1, but the overall secondary structure remained the same (Table 5.4). The binding of ZrK at this site and its hydrolysis did not modify the overall structure of HSA and RMSD remained 1.15 Å in both cases. Since binding of ZrK to sites 1 and 2 and their hydrolysis did not change the structure of HSA, those possibilities were not explored for the remaining two sites.

5.12. ZrK-HSA Interactions at Site 3 (Lys313-Asp314)

The third cleavage site (Lys313-Asp314, site 3) was created by a positively charged (Lys) and a negatively charged (Asp) residue. This site was located 61.4 Å apart from site 1 and positioned on the edge of HSA (Figure 5.11). It contains a small positively charged patch surrounded by a predominantly negative region (Figure 5.12). Among all four cleavage sites, this site was the most challenging to obtain the ZrK-HSA complex. That was in part due to its location at the very edge of HSA with not much in the way of amino acids to stabilize this site. The lack of secondary structure within this site could also account for the loss in stabilization. Unlike for the previous two sites, for which rigid docking multiple binding motifs were observed, here mainly binding to the side of HSA near the cleavage site was detected. However, these binding sites positioned ZrK far (≥ 10 Å) from the peptide bond cleavage site and were discarded. However, flexible docking that allowed Lys313 and Lys317 to adjust their conformations provided a more stable binding site on the very edge of HSA. In this pose, ZrK was positioned much closer to the cleavage site.

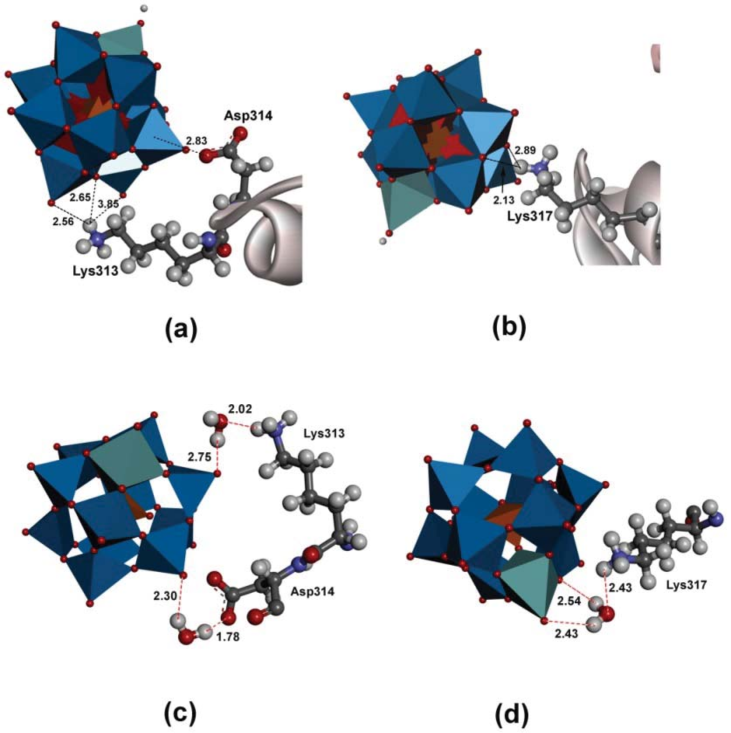

(a) (b)

(c) (d)

Figure 5.17. Most representative structure of POMs-HSA at site 3 obtained from molecular dynamics simulations. (a) and (b) are zoomed in images of binding site 3 with amino acid residues and interaction distances labeled in Å. (c) and (d) are showing water mediated interactions with the oxygen of ZrK, hydrogen bonding interacting distances labeled in Å.

The MD simulations showed that at this site, ZrK was trapped between two positively charged residues Lys313 and Lys317 (Figure 5.17a and 5.17b). Both these residues formed multiple hydrogen bonding interactions with ZrK. In particular, the amine side chains of Lys313 and Lys317 residues associated through contacts with the oxygen cage of ZrK. Additionally, ZrK interacted directly with the residues forming the scissile peptide bond which was not observed for any other site. The NCI plots akso showed Lys313 and Asp314 as main interacting residues and similar to site 2, ZrK formed 3 direct hydrogen bonds on average with HSA (Figure 5.18).

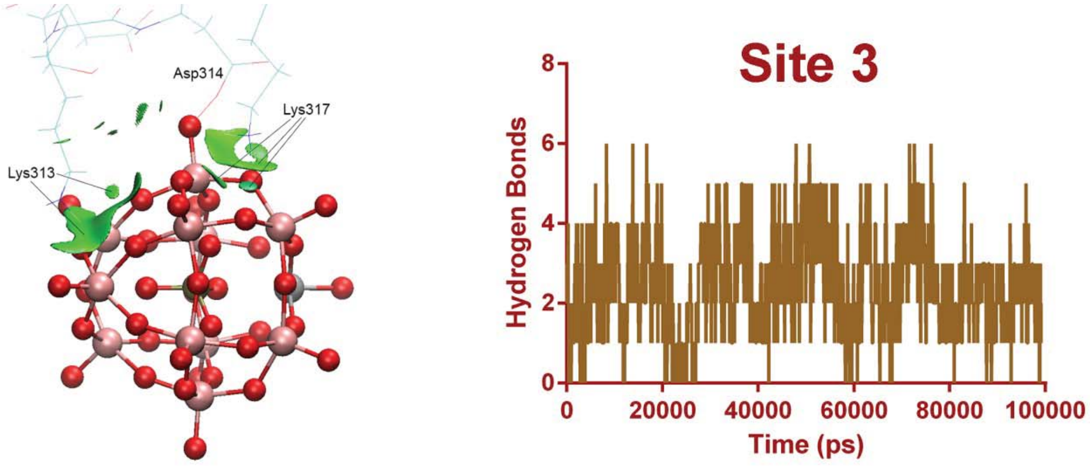

Figure 5.18. Noncovalent interaction plots and hydrogen bonding interactions at site 3

Additionally, some solvent water mediated interactions were observed for this site. For instance, side chains of Lys313 and Asp314 associated with Zrk through one water molecule each that form a single hydrogen bond with oxygen atoms of the metal cluster (Figure 5.17c). On the other hand, the side chain of Lys317 formed a hydrogen bond with a water molecule that in turn interacted through two hydrogen bonds with ZrK (Figure 5.17d). Similar to site 2, the Zr-OH moiety in this site was oriented towards the solvent i.e. on the opposite site of the substrate. The binding free energy of -50.8 kJ/mol for this site is comparable to site 1 but much lower than the binding energy for site 2 (Table 5.3). The ZrK-POM association at this site is facilitated by smaller number but somewhat stronger interactions in comparison to site 1. In comparison to the previous sites, the association of ZrK to this site slightly (1%) decreased the α-helical content (66%) by 1% and 3%, respectively without affecting the overall structure of HSA (Table 5.4).

5.13. ZrK-HSA Interactions at Site 4 (Cys392-Glu393)

The last site (Cys392-Glu393, site 4) was created by a nonpolar (Cys) and a negatively charged (Glu) residue. This site was positioned 33.9 Å away from site 1 on the backside of HSA. It was stabilized by alpha helical secondary structure and a cysteine bridge (Figure 5.11). This binding pocket was surrounded by a very large positively charged region located next to the cleavage site (Figure 5.12). From both rigid and flexible docking, two binding motifs were observed with the first being close to the site of cleavage however was primarily stabilized by a glutamine residue. The second binding motif was located on the opposite side of the cleavage site however it was stabilized by a host of hydrogen bonds originating from positively charge residues such as Lys and Arg. Due to greater electrostatic interaction and stabilization, the second binding motif was found to dominate and was used for the subsequent MD simulations. The binding pocket was formed primary from Arg410, Lys413, Lys414, and Lys541 all held strong interactions with the negatively charged oxygen cage of ZrK (Figure 5.19a and 5.19b). Interestingly, this was the largest positive patch calculated for HSA as shown be electrostatic maps. This large positively charged region could make this site more accessible to ZrK, and this was observed during the simulations. Additionally, this site has been identified as the major binding site for a variety of drug molecules such as ibuprofen[215-216] and diazepam[217-218] and has been labeled Sudlow's drug site II[219-220]. Like site 1, ZrK was held between many positive residues Arg410, Lys413, Lys414, and Lys541 of HSA at distances of 2.20, 2.26, 2.48, and 2.42 Å, respectively (Figure 5.19a and 5.19b). Additionally, these residues interacted through multiple hydrogen bonds with the cage of ZrK, for example, Lys414 shows hydrogen bonding interaction with three separate contacts with the oxygen cage of ZrK.

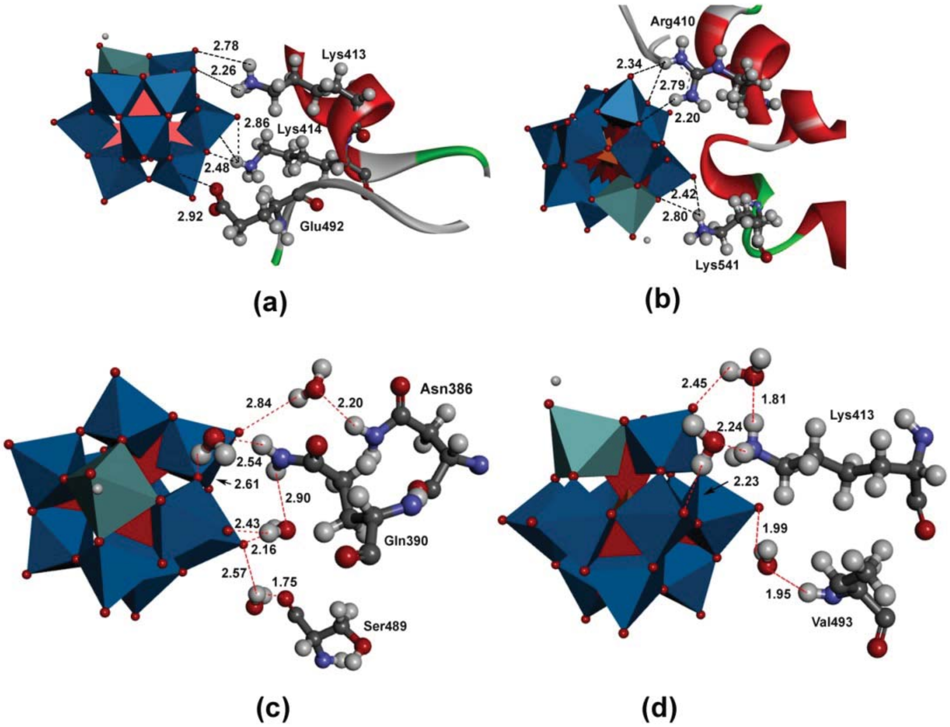

Figure 5.19. Most representative structure of POMs-HSA at site 4 obtained from molecular dynamics simulations. (a) and (b) are zoomed in images of binding site 4 with amino acid residues and interaction distances labeled in Å. (c) and (d) are showing water mediated interactions with the oxygen of ZrK, hydrogen bonding interacting distances labeled in Å.

However, the interaction distances were shorter in comparison to the other sites 2 and 3 where hydrogen bonding was weaker and less in number. This site is most comparable to site 1 where it was surrounded by positively charged residues however; site 4 is more exposed to the solvent whereas site 1 was more buried within the protein. Additionally, Glu492 forms an electrostatic interaction with a W metal, which is part of the cage of

ZrK, at a distance of 2.92 Å (Figure 5.19a). This interaction was further probed by a short MD simulation run where Glu492 was flipped out of the binding pocket (≥ 6 Å). Within the first 10 ps, Glu492 coordinated in a mono-dentate fashion, and then switched back to a bi-dentate coordinate only after 50 ps of simulation time.

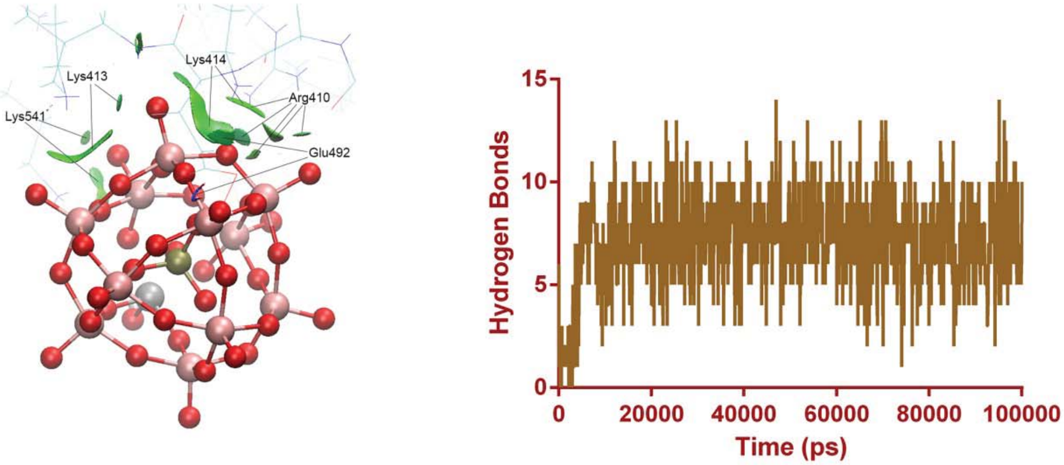

Figure 5.20. Noncovalent interaction plots and hydrogen bonding interactions at site 4

At this site, ZrK formed the highest number of direct hydrogen bonds, 8 on average, with HSA and showed strong interactions with Lys541, Lys413, Lys414, Arg410, and Glu492 (Figure 5.20). Like in the first three sites, hydrogen bonding interaction involving one water molecule was observed. For instance, side chains of Gln390, Asn386, and Ser489 interact with ZrK through one water molecules (Figure 5.19c). Ser489 associates with this complex through unusual hydrogen bonding. The carboxyl group of this residue utilizes one water molecule to interact with ZrK (Figure 5.19c). This site possessed the highest binding free energy (-91.2 kJ/mol, Table 5.3) among all four binding sites.

Similar to site 1, in contrast to sites 2 and 3, the Zr-OH group here was opposite the protein's surface and was shifted towards the cleavage site. Rather surprisingly, the α-helical content (66%) of this site is exactly the same as of the site 3 (Table 5.4).

Position	**Coil**	**Bend**	**Turn**	**A-Helix**	**3-Helix**
HSA	13	8	9	68	2
Site 1	13	6	9	67	5
Site 2	13	6	9	69	3
Site 3	13	7	10	66	4
Site 4	13	6	10	66	5

Table 5.4. Secondary structure (%) of Human Serum Albumin (HSA) and POMs bound to HSA at sites 1-4.

5.14. Investigation of Cleavage Site Preference Using QM/MM

To see if there is an energetic preference for the cleavage of one site over another, QM/MM calculations have been performed. The starting structures for the QM/MM simulations were taken from the MD results in the previous section. The ZrK catalyzed peptide hydrolysis has been proposed to occur via the general dual activation mechanism.[221-223] This mechanism was also proposed to be utilized by metalloproteases such as thermolysin and insulin degrading enzyme.[224-225] According to the mechanism (Figure 2), the binding of the HSA substrate to the ZrK (**R'**$_{\mathbf{E}}$) generates the reactant (**R**$_{\mathbf{E}}$). In **R**$_{\mathbf{E}}$, the Zr ion plays the role of a Lewis acid and activates HSA substrate through the coordination of its carbonyl oxygen atom. This interaction increases the electrophilicity of the carbon atom of the substrate and polarizes the peptide bond. Therefore, the Zr-O=C(HSA) association reflects a degree of its Lewis acidity.[226] The weak metal-ligand interaction is also known to increase Lewis acidity of the metal ion.[226-230] Since Zr(IV) bound water is known to have very low pK_a value ($\leq$ 0.6), it creates a hydroxyl nucleophile by activating a water molecule.[231] From $\mathbf{R_E}$, an attack of the hydroxyl nucleophile on the amide carbonyl carbon of HSA generates a four-membered ring containing tetrahedral intermediate ($\mathbf{IN_E}$).

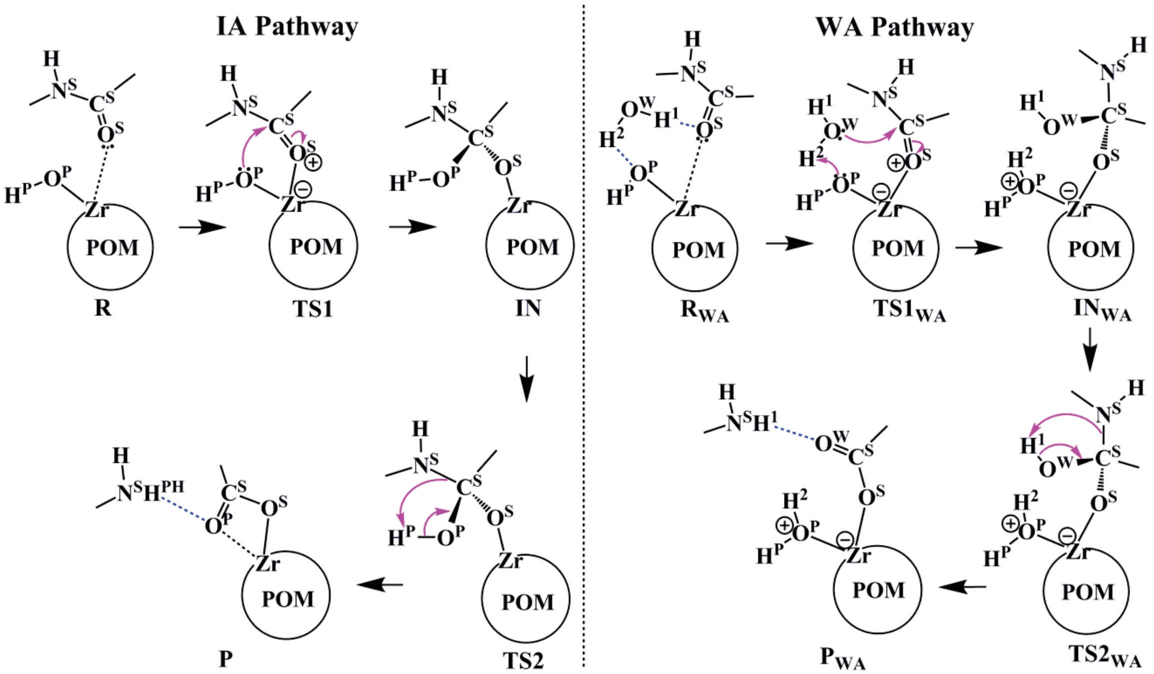

Figure 5.21. Mechanisms studies using ZrK as the catalyst

In this process, the Zr(IV) ion facilitates the release of the nucleophile at the peptide bond due to the fast ligand exchange kinetics.[232] The Zr(IV)-OH bond distance provides a measure of the strength of the nucleophile.[233-234] Lewis acidity of the Zr(IV) ion and nucleophilicity of the hydroxyl oxygen along with geometry of $\mathbf{IN_E}$ affect the kinetics of this step.[223] These two effects can counter each other i.e. an increase in Lewis acidity of the metal ion can lower the nucleophilicity of the hydroxyl ion.[226, 235-238] In the last step, a proton transfer from the hydroxyl ion to the amine group of the HSA splits the amide bond (-C-N-). Here, the Zr(IV) ion promotes the release of separated amine (-NH_2) and carboxyl (-COO) termini (**P**$_E$).

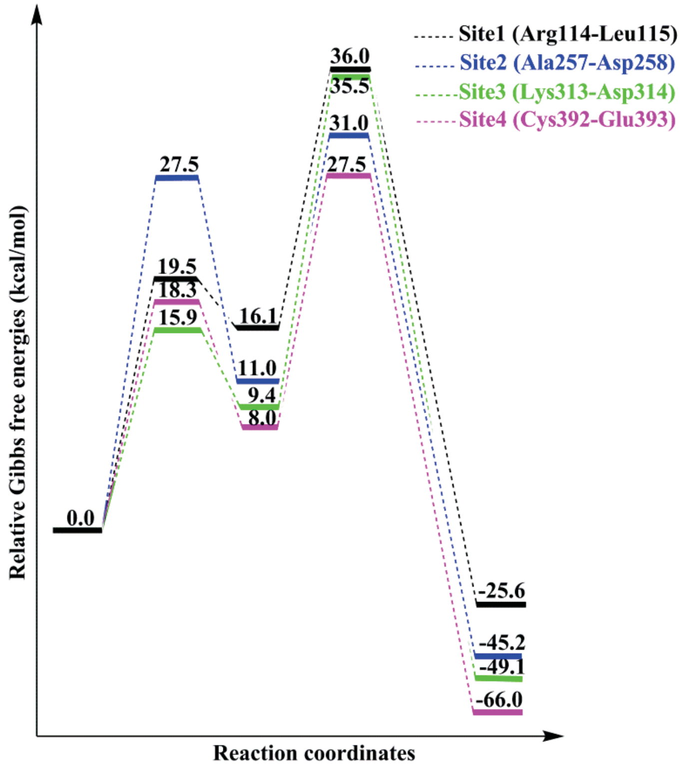

Figure 5.22.Calculated potential energy surface of sites 1, 2, 3, and 4 of HSA.

Despite the availability of the wealth of experimental information, the exact mechanism and energetics for the hydrolysis of all four sites of HSA by ZrK is not known. In this two layer QM/MM (ONIOM) study, we have elucidated the mechanistic, kinetic and structural properties of HSA hydrolysis at multiple sites by ZrK. These reactions were studied using two different mechanisms: internal attack (IA) and water assisted (WA). Additionally, two different models (NW and LW) are used to simulate these mechanisms. There was no water in the low layer in the NW model, while 57 explicit water molecules were included in the low layer in the LW model. The computed energetics for the hydrolysis of the major site (site 4) of HSA predicted that the cleavage of peptide bond occurs in the rate-limiting step (step 2) in both mechanisms. These calculations suggested that the IA mechanism is energetically most feasible pathway for the HSA hydrolysis. The barrier using this mechanism in the rate-limiting step was 4.1 kcal/mol lower in energy than the barrier for the WA mechanism for site 4. The LW model was found to be more accurate than the NW model for this mechanism i.e. barrier in the rate limiting step in the former is 7.9 kcal/mol lower than the one in the latter for the same site. The computed energies for the IA mechanism are in agreement with the measured kinetics for hydrolysis of a variety of dipeptides.[239] These calculations suggest a clear energetic preference (site 4, site 2, site 3 and site 1) for the hydrolysis of the four sites of HSA by ZrK.

5.15. Summary and Conclusions

In this study, we have employed molecular docking and all-atom MD simulation techniques to study interactions of 1:1 Zr-containing Keggin POM (ZrK) with four cleavage sites of HSA. These chemically diverse sites (Arg114-Leu115, Ala257-Asp258, Lys313-Asp314, and Cys392-Glu393) were located in different parts of HSA (Figure 5.11). They were found to bind in a rather distinct manner to form the ZrK-HSA complexes. These complexes were dominated by hydrogen bonding and electrostatic interactions from the Zr and oxo group containing cage of ZrK and both negatively and positively charged amino acid residues of HSA. The computed binding free energies (-57.5, -24.2, -50.8, and -91.2 kJ/mol for site 1, 2 ,3 and 4, respectively) suggested that there is one major binding site (site 4), two intermediate (site 1 and site 3) and one minor binding site (site 2), Table 5.3. The site 4 has been known to bind several drug molecules as well. The high exothermicity of this process was in agreement with the measured value (ΔH = -50 kJ/mol) for the POM [H2W12]-HSA interaction.[213] It is suggested to be driven mostly by electrostatic interactions.[213] At site 4, the ZrK-HSA complex formed 8 direct hydrogen bonds on average, while 2-3 direct hydrogen bonds were observed for sites 2 and 3. These hydrogen bonds were contributed by positively charged Lys and Arg residues. Additionally, there were multiple hydrogen bonding interactions mediated by 1-3 solvent water molecules. The binding of ZrK to HSA did not modify the secondary structure of HSA which was primarily dominated by α-helical conformation (67%), Table 5.4. Furthermore, as suggested experimentally the binding of ZrK and hydrolysis at sites 1 and 2 did not alter the overall structure of HSA.[214] POMs, in general, have been reported to interact with diverse biomolecules through hydrogen bonding albeit with varying strength, extent, and type. Our study is complementary to experimental binding studies between POMs and proteins that are typically performed with ITC or Trp fluorescence spectroscopy, however it offers an additional advantage as it allows detailed molecular and thermodynamic understanding of each binding site separately. Therefore, these results can be also applicable to understand the interaction of other POMs with a variety of different proteins. The QM/MM calculations suggest a clear energetic preference (site 4, site 2, site 3 and site 1) for the hydrolysis of the four sites of HSA by ZrK.

5.16. Hybrid Peptide ATCUN-sh-Buforin Binding to DNA

A plethora of life forms have evolved the ability to synthesize antimicrobial peptides (AMPs) as part of a defense mechanism against invading organisms. This large class of peptides is effective against a wide range of microbes, and exerts their action either by direct interaction or by enhancing pathogen clearance by activating an immune response.[240-242] The variety of mechanisms of action is the main reason why bacteria exposed to AMPs have a hard time developing resistance.[99] For this reason, AMPs have attached attention from both academics and drug developers in industry.[99] The rational design of AMPs depends largely on the understanding of the molecular characteristics responsible for its binding and antimicrobial activity. Thus, we have studied the influence of a basic residue in the ATCUN motif in AMPs that can readily target DNA. This was done by appending a RTH (Arg-Thr-His) motif to *sh*-Buforin and comparing it to its derivative containing a VIH (Val-Ile-His) motif. The effect of the stereochemistry (L or D) of the parent peptide has also been investigated. An increase in activity is expected for D-BF2 due to a pervious study that showed L to D substutuions increased the ROS-generating activity of the ATCUN motif.[99, 243]

5.17. Molecular Docking Study on Four Forms of Buforin with DNA

An initial structural model of L-type BF2 (L-BF2) peptide bound to DNA was generated beginning with the crystal structure PDB ID: 1AOI of the *Xenopus laevis* histone and was equilibrated using molecular dynamic simulations. The initial L-BF2 peptide residues were converted to their D-derivatives (D-BF2) through changing the stereo chemistry around their Cα atoms (Figure 5.23). The equilibrated structures reached a steady state within a 50 ns simulation proven by rmsd calculations. Significant changes occurred, 0.6 nm and 0.8 nm from the L-BF2 and D-BF2 initial structures, respectively. Cluster calculations were performed to ensure the most representative structures were used for docking procedures with an RMSD cutoff of 0.3 nm. The relaxed structures were docked to different conformations of DNA allowing for further molecular dynamics simulations to be performed instituting a pre-production phase of 5 ns followed by a production phase of 15 ns.

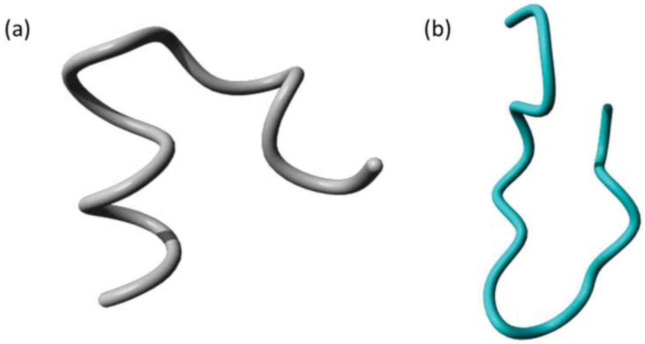

Figure 5.23. (A) Most equilibrated structure of the L-BF2 peptide. (B) Most equilibrated structure of the D-BF2 peptide

Combinations of docking and molecular dynamics (MD) simulation have been employed to study the interaction between four different forms of buforin with DNA. The four forms studied were L-BF2, D-BF2, VIH-BF2, and RTH-BF2. Docking of the four forms to DNA yielded 100 docked poses for each peptide. Pose selection for the initial MD structure was based on Uyterhoeven et al.[244] computational and experimental findings in 2008 where the peptide's basic residues interact with the negatively charged backbone of DNA. Both L and D forms of BF2 showed preferential binding to the major groove of the DNA segment studied (>90% of poses examined). However, the D form of the peptide showed greater affinity for minor groove binding than that of the L form, 10% and <1% respectively. Nonetheless, these results are expected based on the docking procedure performed where the peptide is kept rigid, the D form is slightly elongated allowing for fitting within the minor grove where the L form is bulkier. A comparison of the two equilibrated forms (L and D) is shown in Figure 5.23. The docked poses that showed the highest number of basic residues interacting with the negatively charged phosphate backbone of the DNA segment were chosen for further MD simulations. ATCUN portions of the peptides where attached to the L-form of the BF2 peptide and docking procedures performed. Docking the ATCUN-BF2 to the DNA segment produced similar results to the peptide docked without the ATCUN bound. However, the position of the ATCUN portion of the peptide relative to the DNA did change when comparing the VIH and RTH motifs. The VIH-BF2 complex studied exhibits an ATCUN position equatorial to a negatively charged phosphate group on the DNA while the RTH-BF2 complex is axial to the same phosphate group. Since in all cases, the basic residue components of the parent peptide bound to the negatively charged phosphate backbone, there would be non-specific binding to DNA as the phosphate backbone is identical throughout its structure.[244]

5.18. Molecular Dynamics Study on Four Forms of Buforin with DNA

After the MD simulations, the peptide in all structures studied stayed within the major groove pocket of the DNA segment. Basic residues within the parent chain and the ATCUN portions had the highest binding interactions in all simulations. Table 5.5 shows the interacting residues within the MD simulations performed. L-BF2’s residues; Gly 9, Arg 10, and Arg 16 display hydrogen bonding with phosphate groups present on the DNA backbone at distances of 2.02, 1.85, and 1.88 Å respectively (Fig 5.24). Basic residue Arg 13 of the same peptide shows hydrogen bonding with the interior base residue guanine 179 at a distance of 2.25 Å.

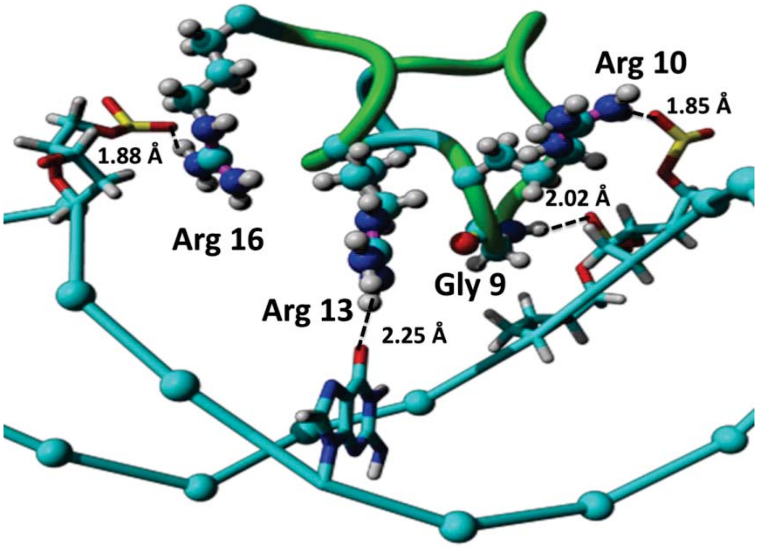

Figure 5.24. L-BF2 shown binding with DNA segment with residues, electrostatic interactions, and distances labeled. Interactions are shown with the black dotted lines

The D-BF2 peptide's residues Arg 10 and Arg 16 show similar hydrogen bonding interactions, but at distances of 2.43 and 1.97 Å respectively. In comparison, D-BF2 is stabilized by additional hydrogen bonding between residues Arg 1, His 12, and Arg 16 (Figure 5.25) with phosphate groups present on the DNA's backbone. The VIH-BF2 peptide's Gln 4 residue shows hydrogen bonding with an amine group present on the interior base cytosine 116 at a distance of 1.70 Å. Only the L-BF2 and VIH-BF2 complexes studied showed interactions with interior base residues. Moreover, the parent peptide's first residue Arg 1 helps stabilize the VIH-ATCUN's copper center equatorially to the backbone of DNA through hydrogen bonding (Figure 5.26).

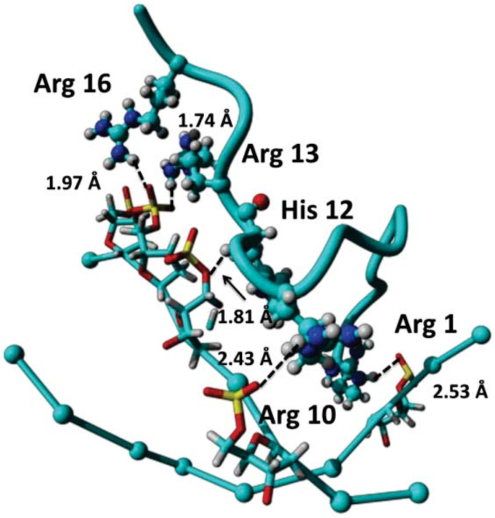

Figure 5.25. D-BF2 shown binding with DNA segment with residues, electrostatic interactions, and distances labeled. Interactions are shown with the black dotted lines

Residues Arg 10 and Arg 13 participate in hydrogen bonding with phosphate groups at distances of 1.82 and 1.86 Å, respectively. In addition, VIH-BF2's parent peptide is stabilized by the C-terminus residue Lys 17 at a distance of 1.64 Å (Fig 5.26), while in all other complexes studied, Arg 16 is responsible for the peptide's C-terminus stability in the major groove. The RTH-BF2 complex is different in that the sole interacting residue from the parent peptide is Arg 16 at a distance of 1.74 Å. Furthermore, the two other interacting residues, Arg and Thr, belong to the ATCUN portion of the complex and interact through hydrogen bonding at distances of 1.93 and 1.85 Å, respectively. Interestingly, the parent peptide in all cases was responsible for the majority of binding to the DNA segment, excepting the RTH_BF2 complex (Figure 5.27). Three separate MD simulations where run to rule out incorrect selections of docked poses, and in all cases, the arginine and threonine residues of the ATCUN were the main binding contributors.

These residues showed interactions with the phosphate backbone of the DNA and stabilized the ATCUN's copper center within a more specific area.

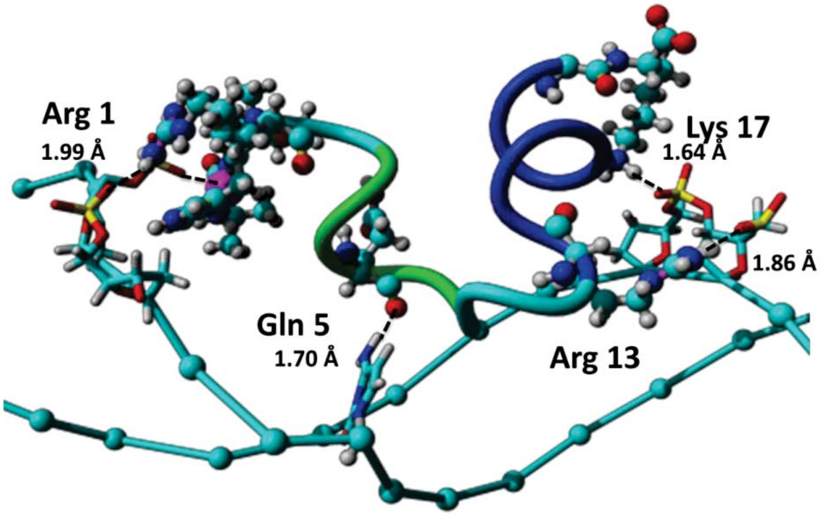

Figure 5.26. VIH-BF2 shown binding with DNA segment with residues, electrostatic interactions, and distances labeled. Interactions are shown with the black dotted lines

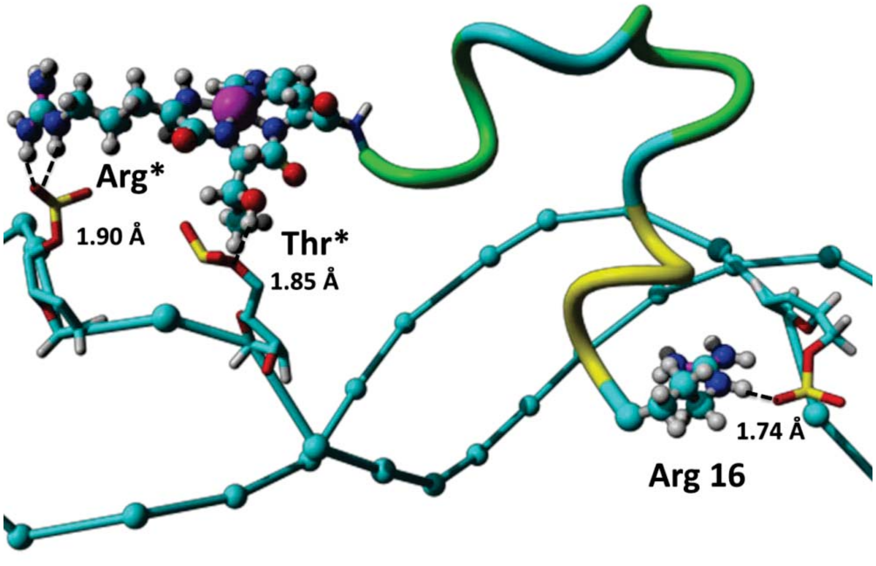

Figure 5.27. RTH-BF2 shown binding with DNA segment with residues, electrostatic interactions, and distances labeled. Interactions are shown with the black dotted lines

In contrast, in the VIH-ACTUN motif, the first arginine residue present on the parent peptide helped stabilize its position within the DNA segment through the same electrostatic interaction.

System	Interacting Residues	Interacting portions of DNA	Distance (Å)
L-BF2	Arg 29	Backbone DT 112	1.852
	Gly 28	Backbone DA 113	2.025
	Arg32	Guanine 179	2.253
	Arg 35	Backbone DA 176	1.883
D-BF2	Arg 20	Backbone DT 118	2.534
	Arg 29	Backbone DA 174	2.428
	His 31	Backbone DC 172	1.805
	Arg32	Backbone DC 171	1.742
	Arg35	Backbone DC 171	1.967
VIH-BF2	Arg20	Backbone DA 113	1.994
	Gln 24	Cytosine 116	1.702
	Arg 29	Backbone DC 172	1.818
	Arg 32	Backbone DA 173	1.859
	Lys 36	Backbone DA 173	1.636
RTH-BF2	Arg*	Backbone DT 112	1.930
	Thr*	Backbone DC 114	1.854
	Arg35	Backbone DC 171	1.739

Table 5.5. Interacting residues from the parent peptide. * represent interactions from the ATCUN amino acid residues with the DNA segment.

System	E_{elec} (kcal/mol)	ΔG_{ele} (kcal/mol)
L-BF2	-37.65	-14.97
D-BF2	-41.19	-15.01
VIH-BF2	-54.39	-18.76
RTH-BF2	-22.12	-5.17

Table 5.6. Electrostatic energy, desolvation energy of the BF2 complex, desolvation energy of DNA, and the binding energies.

However, the VIH motif's parent peptide showed decreased distance between itself and the base pairs of the DNA (embedded in the DNA). Binding energies of the L-BF2, D-BF2, VIH-L-BF2 and RTH-L-BF2 peptides computed using Adaptive Poisson-

Boltzmann Solver (APBS) software are 14.9, 15.0, 18.8 and 5.2 kcal/mol, respectively (Table 5.6). This result is consistent with the both the L-BF2 and D-BF2 peptides studied.

5.19. Summary and Conclusion

In summary, the addition of the ATCUN motif increased the binding energy indicated increased interaction with the DNA segment. Furthermore, the parent peptide was primarily responsible for the binding to DNA excepting the charged RTH-BF2 where the ATCUN portion of the peptide interacted with the major groove. This interaction caused an unfavorable conformation between the parent peptide and the DNA. From the structure above, it is apparent that the L to D amino acid substation resulted in increased surface interaction with the DNA segment however; this was not reflected in the binding energy calculation mostly due to large solvation effects observed. Additionally, basic residues within the parent chain and the ATCUN portions had the highest binding interactions in all simulations . Since in all cases, the basic residue components of the parent peptide bound to the negatively charged phosphate backbone, there would be non-specific binding to DNA as the phosphate backbone is identical throughout its structure. These results provide atomistic insight into the binding event between *sh*-Buforin and DNA.

References

(1) Association, A. s., Alzheimer's Disease Facts and Figures. *Alzheimer's and Dementia* **2014,** *10*.

(2) Masters, C.; Simms, G.; Weinman, N., Amyloid Plaque Core Protein in Alzheimer's Disease and Down Syndrome. *PNAS* **1985**, 4245-4249.

(3) Glenner, G.; Wong, C., Alzheimer's Disease: Initial Report of the Purification and Characterization of a Novel Cerebrovascular Amyloid Protein *Biochem Biophys Res. Commun.* **1984,** *120*.

(4) Cui, H.; Hung, A.; Freeman, C.; Small, D., Size and Suflation Are Critical for the Effect of Heparin on App Processing and Ab Production *J Neurochem.* **2012**, 447-457.

(5) Bergamaschini, L.; Rossi, E.; Vergani, C.; Simoni, M. D., Alzheimer's Disease: Another Target for Heparin Therapy. *Sci. World J* **2009**, 891-908.

(6) Leveugle, B.; Ding, W., Heparin Oligsaccharides That Pass the Blood-Brain Barrier Inhibit Beta-Amyloid Protein Secretion and Heparin Binding to Beta-Amyloid Peptide. *J. Neurochem* **1998**, 736-744.

(7) Leveugle, B.; Ding, W.; al., e., Heparin Promotes Beta-Secretase Cleavage of the Alzheimer's Amyloid Precursor Protein. *Neurochem Int.* **1997**, 543-548.

(8) Scholfield, Z.; Yates, E.; Wayne, G., Heparan Sulfate Regulates Amyloid Precursor Protein Processing by Bace1, the Alzheimer's Beta-Secretase. *J. Cell Biol.* **2003**, 97-107.

(9) Bergamaschini, L.; Donarini, C.; Gobbo, G.; Parnetti, G., Activation of Complement and Contact System in Alzheimer's Disease. *Mech. Ageing Dev.* **2001**, 1971-1983.

(10) Velazquez, P.; Cribbs, D.; Poulos, T.; Tenner, A., Aspartate Residue 7 in Amyloid Beta-Protein Is Critical for Classical Complement Pathway Activation: Implications for Alzheimer's Disease Pathogenesis. *Nat Med.* **1997**, 77-79.

(11) Webster, S.; Bonnell, B.; Rogers, J., Charge-Based Binding Binding of Complement Component C1q to the Alzheimer Amyloid Beta-Peptide *Am. J. Pathol* **1997**, 1531-1536.

(12) Ma, Q.; Cornelli, U.; Hanin, I.; Jeske, W.; Linhardt, R., Heparin Oligosaccharides as Potential Therapeutic Agents in Senile Dementia. *Curr. Pharm. Des.* **2007**, 1607-1616.

(13) Tyrrell, D.; Horne, A.; Preuss, K.; Page, C., Heparin in Inflammation: Potential Therapeutic Applications Beyond Anticoagulation *Adv. Pharmacol.* **1999**, 151-208.

(14) Watson, D.; Lander, A.; Selkoe, D., Heparin-Binding Properties of the Amyloidgenic Peptides Abeta and Amylin. Dependence on Aggregation State and Inhibition by Congo Red. *J. Biol. Chem.* **1997**, 31617-31624.

(15) Bergamaschini, L.; Donarini, C.; Rossi, E.; Luigi, A. D.; Vergani, C., Heparin Attenuates Cytotoxic and Inflammatory Activity of Alzheimer Amyloid-Beta in Vitro. *Neurobiol. Aging.* **2002**, 531-536.

(16) Pollack, S.; Sanders, I.; Hawtin, S., Sulfonated Dyes Attenuate the Toxic Effects of Beta-Amyloid in a Structure-Specfic Fashion. *Neurosci. Lett.* **1995**, 211-214.

(17) Pollack, S.; Sanders, I.; Hawtin, S., Sulfated Glycoaminoglycans and Dyes Attenuate the Neurotoxic Effects of Beta-Amyloid in Rat Pc12 Cells. *Neurosci. Lett.* **1995**, 113-116.

(18) Woods, A.; Cribbs, D.; Whittemore, E.; Cotman, C., Heparan Sulfate and Chondroitin Sulfate Glycoaminoglycan Attenuate Beta-Amyloid(23-25) Induced Neurodegeneration in Cultured Hippocampal Neurons. *Brain Res.* **1995**, 53-62.

(19) Nie, Q.; Du, X.-g.; Geng, M.-y., Small Molecule Inhibitors of Amyloid Β Peptide Aggregation as a Potential Therapeutic Strategy for Alzheimer'S Disease. *Acta Pharmacologica Sinica* **2011,** *32*, 545.

(20) Belluti, F.; Rampa, A.; Gobbi, S.; Bisi, A., Small-Molecule Inhibitors/Modulators of Amyloid-Β Peptide Aggregation and Toxicity for the Treatment of Alzheimer's Disease: A Patent Review (2010 – 2012). *Expert Opin. Ther. Pat.* **2013,** *23*, 581-596.

(21) Young, L. M.; Saunders, J. C.; Mahood, R. A.; Revill, C. H.; Foster, R. J.; Tu, L.-H.; Raleigh, D. P.; Radford, S. E.; Ashcroft, A. E., Screening and Classifying Small-Molecule Inhibitors of Amyloid Formation Using Ion Mobility Spectrometry–Mass Spectrometry. *Nat. Chem.* **2014,** *7*, 73.

(22) Jin, L. H.; J., K. K.; Younwoo, N.; Juhye, K.; J., P. T.; A., K. R.; Seung, Y. I.; Mehmet, O.; S., K. K.; T., R. B., et al., Structural and Mechanistic Insights into Development of Chemical Tools to Control Individual and Inter-Related Pathological Features in Alzheimer's Disease. *Chem. Eur. J.* **2017,** *23*, 2706-2715.

(23) Ratner, B. D.; Hoffman, A. S.; Schoen, F. J.; Lemons, J. E., *Biomaterials Science: An Introduction to Materials in Medicine*. 2nd ed.; Elsevier Academic Press: 2004; p 824.

(24) Becke, A. D., Density-Functional Exchange-Energy Approximation with Correct Asymptotic Behavior. *Phys. Rev. A* **1988,** *38*, 3098-3100.

(25) Smith, J. F.; Knowles, T. P. J.; Dobson, C. M.; Macphee, C. E.; Welland, M. E., Characterization of the Nanoscale Properties of Individual Amyloid Fibrils *PNAS* **2006,** *103*, 15806-15811.

(26) Knowles, T. P.; Fitzpatrick, A. W.; Meehan, S.; Mott, H. R.; Vendruscolo, M.; Dobson, C. M.; Welland, M. E., Role of Intermolecular Forces in Defining Material Properties of Protein Nanofibrils. *Science* **2007,** *318*, 1900-1903.

(27) Wu, Z.; Tang, Y.; Fang, H.; Su, Z.; Xu, B.; Lin, Y.; Zhang, P.; Wei, X., Decellularized Scaffolds Containing Hyaluronic Acid and Egf for Promoting the Recovery of Skin Wounds. *J. Mater. Sci. Mater. Med.* **2015,** *26*, 1-10.

(28) Becke, A. D., Density-Functional Thermochemistry. Iii. The Role of Exact Exchange. *J. Chem. Phys.* **1993,** *98*, 5648-5652.

(29) Lee, C.; Yang, W.; Parr, R. G., Development of the Colle-Salvetti Correlation-Energy Formula into a Functional of the Electron Density. *Phys. Rev. B* **1988,** *37*, 785-789.

(30) Zhang, S., Fabrication of Novel Biomaterials through Molecular Self-Assembly. *Nat. Biotech.* **2003,** *21*, 1171-1178.

(31) Meersman, F.; Dobson, C. M., Probing the Pressure–Temperature Stability of Amyloid Fibrils Provides New Insights into Their Molecular Properties. *Biochim. Biophys. Acta* **2006,** *1764*, 452-460.

(32) Hamada, D.; Yanagihara, I.; Tsumoto, K., Engineering Amyloidogenicity Towards the Development of Nanofibrillar Materials. *Trends Biotechnol.* **2004,** *22*, 93-97.

(33) Lopez De La Paz, M.; Goldie, K.; Zurdo, J.; Lacroix, E.; Dobson, C. M.; Hoenger, A.; Serrano, L., De Novo Designed Peptide-Based Amyloid Fibrils. *PNAS* **2002,** *99*, 16052-16057.

(34) Saiki, M.; Shiba, K.; Okumura, M., Structural Stability of Amyloid Fibrils Depends on the Existence of the Peripheral Sequence near the Core Cross-B Region. *FEBS Lett.* **2015,** *589*, 3541-3547.

(35) Makin, O. S.; Atkins, E.; Sikorski, P.; Johansson, J.; Serpell, L. C., Molecular Basis for Amyloid Fibril Formation and Stability. *PNAS* **2005,** *102*, 315-320.

(36) Broersen, K.; Jonckheere, W.; Rozenski, J.; Vandersteen, A.; Pauwels, K.; Pastore, A.; Rousseau, F.; Schymkowitz, J., A Standardized and Biocompatible Preparation of Aggregate-Free Amyloid Beta Peptide for Biophysical and Biological Studies of Alzheimer's Disease. *Protein Eng. Des. Sel.* **2011,** *24*, 743-750.

(37) Zhang, S. G.; Holmes, T.; Lockshin, C.; Rich, A., Spontaneous Assembly of a Self-Complementary Oligopeptide to Form a Stable Macroscopic Membrane. *PNAS* **1993,** *90*, 3334-3338.

(38) Jacob, R. S.; Ghosh, D.; Singh, P. K.; Basu, S. K.; Jha, N. N.; Das, S.; Sukul, P. K.; Patil, S.; Sathaye, S.; Kumar, A., et al., Self Healing Hydrogels Composed of Amyloid Nano Fibrils for Cell Culture and Stem Cell Differentiation. *Biomaterials* **2015,** *54*, 97-105.

(39) Gelain, F.; Bottai, D.; Vescovi, A.; Zhang, S., Designer Self-Assembling Peptide Nanofiber Scaffolds for Adult Mouse Neural Stem Cell 3-Dimensional Cultures. *PLoS ONE* **2006,** *1*, e119.

(40) Scheibel, T.; Parthasarathy, R.; Sawicki, G.; Lin, X. M.; Jaeger, H.; Lindquist, S. L., Conducting Nanowires Built by Controlled Self-Assembly of Amyloid Fibers and Selective Metal Deposition. *PNAS* **2003,** *100*, 4527-4532.

(41) Petkova, A. T., Ishii, Y., Balbach, J. J., Antzutkin N. O., Leapman, R. D., Delaglio, F., and Tycko, R., A Structural Model for Alzheimer's Β-Amyloid Fibrils Based on Experimental Constrains from Solid State Nmr. *PNAS* **2002,** *99*, 16742-16747.

(42) Shiraham.T; Cohen, A. S., Reconstitution of Amyloid Fibrils from Alkaline Extracts. *J. Cell Bio.* **1967,** *35*, 459-&.

(43) Nielsen, L.; Frokjaer, S.; Carpenter, J. F.; Brange, J., Studies of the Structure of Insulin Fibrils by Fourier Transform Infrared (Ftir) Spectroscopy and Electron Microscopy. *J. Pharm. Sci.* **2001,** *90*, 29-37.

(44) Jimenez, J. L.; Nettleton, E. J.; Bouchard, M.; Robinson, C. V.; Dobson, C. M.; Saibil, H. R., The Protofilament Structure of Insulin Amyloid Fibrils. *PNAS* **2002,** *99*, 9196-9201.

(45) Khurana, R.; Ionescu-Zanetti, C.; Pope, M.; Li, J.; Nielson, L.; Ramirez-Alvarado, M.; Regan, L.; Fink, A. L.; Carter, S. A., A General Model for Amyloid Fibril Assembly Based on Morphological Studies Using Atomic Force Microscopy. *Biophys. J.* **2003,** *85*, 1135-1144.

(46) Serpell, L. C.; Sunde, M.; Benson, M. D.; Tennent, G. A.; Pepys, M. B.; Fraser, P. E., The Protofilament Substructure of Amyloid Fibrils. *J. Mol. Biol.* **2000,** *300*, 1033-1039.

(47) Xu, Z.; Paparcone, R.; Buehler, M. J., Alzheimer's Aβ(1-40) Amyloid Fibrils Feature Size-Dependent Mechanical Properties. *Biophys. J.* **2010,** *98*, 2053-2062.

(48) Paparcone, R.; Pires, M. A.; Buehler, M. J., Mutations Alter the Geometry and Mechanical Properties of Alzheimer's a Beta(1-40) Amyloid Fibrils. *Biochemistry* **2010,** *49*, 8967-8977.

(49) Lv, S.; Dudek, D. M.; Cao, Y.; Balamurali, M. M.; Gosline, J.; Li, H., Designed Biomaterials to Mimic the Mechanical Properties of Muscles. *Nature* **2010,** *465*, 69-73.

(50) Cherny, I.; Gazit, E., Amyloids: Not Only Pathological Agents but Also Ordered Nanomaterials. *Angew. Chem., Int. Ed.* **2008,** *47*, 4062-4069.

(51) Knowles, T. P. J.; Buehler, M. J., Nanomechanics of Functional and Pathological Amyloid Materials. *Nat. Nanotech.* **2011,** *6*, 469-479.

(52) Petkova, A. T.; Yau, W.-M.; Tycko, R., Experimental Constraints on Quaternary Structure in Alzheimer's B-Amyloid Fibrils. *Biochemistry* **2006,** *45*, 498-512.

(53) Riek, R., Guntert P., Dobeli H., and Wuthrich K., Nmr Studies in Aqueous Solution Fail to Identify Significant Conformational Differences between the Monomeric Forms of Two Alhzeimer Peptides with Widely Different Plaque-Competence, Ab(1-40)^{Ox} and Ab(1-42)^{Ox}. *Eur. J. Biochem.* **2001,** *268*, 5930-5936.

(54) Sipe, J. D., Cohen, A. S Review: History of the Amyloid Fibril *J. Stru. Biol.* **2000,** *130*, 88-98.

(55) Bernstein, S. L.; Dupuis, N. F.; Lazo, N. D.; Wyttenbach, T.; Condron, M. M.; Bitan, G.; Teplow, D. B.; Shea, J.-E.; Ruotolo, B. T.; Robinson, C. V., et al., Amyloid-B Protein Oligomerization and the Importance of Tetramers and Dodecamers in the Aetiology of Alzheimer's Disease. *Nat. Chem.* **2009,** *1*, 326-331.

(56) Bernstein, S. L.; Wyttenbach, T.; Baumketner, A.; Shea, J.-E.; Bitan, G.; Teplow, D. B.; Bowers, M. T., Amyloid B-Protein: Monomer Structure and Early Aggregation States of Aβ42 and Its Pro19 Alloform. *J. Am. Chem. Soc.* **2005,** *127*, 2075-2084.

(57) Hamley, I. W., The Amyloid Beta Peptide: A Chemist's Perspective. Role in Alzheimer's and Fibrillization. *Chem. Rev.* **2012,** *112*, 5147-5192.

(58) Nasica-Labouze, J.; Nguyen, P. H.; Sterpone, F.; Berthoumieu, O.; Buchete, N.-V.; Coté, S.; De Simone, A.; Doig, A. J.; Faller, P.; Garcia, A., et al., Amyloid B Protein and Alzheimer's Disease: When Computer Simulations Complement Experimental Studies. *Chem. Rev.* **2015,** *115*, 3518-3563.

(59) Jimenez, J. L.; Nettleton, E. J.; Bouchard, M.; Robinson, C. V.; Dobson, C. M.; Saibil, H. R., The Protofilament Structure of Insulin Amyloid Fibrils. *Proc Natl Acad Sci U S A* **2002,** *99*, 9196-9201.

(60) Siegbahn, P. M., The Catalytic Cycle of Catechol Oxidase. *J Biol Inorg Chem.* **2004,** *9*, 577-590.

(61) Meersman, F.; Dobson, C. M., Probing the Pressure–Temperature Stability of Amyloid Fibrils Provides New Insights into Their Molecular Properties. *Biochimica et Biophysica Acta (BBA) - Proteins and Proteomics* **2006,** *1764*, 452-460.

(62) Blomberg, M. R. A.; Borowski, T.; Himo, F.; Liao, R.-Z.; Siegbahn, P. E. M., Quantum Chemical Studies of Mechanisms for Metalloenzymes. *Chem. Rev.* **2014,** *114*, 3601-3658.

(63) Xu, Z.; Paparcone, R.; Buehler, M. J., Alzheimer's Aβ(1-40) Amyloid Fibrils Feature Size-Dependent Mechanical Properties. *Biophysical Journal* **2010,** *98*, 2053-2062.

(64) Graveland-Bikker, J. F.; Schaap, I. A. T.; Schmidt, C. F.; de Kruif, C. G., Structural and Mechanical Study of a Self-Assembling Protein Nanotube. *Nano Lett.* **2006,** *6*, 616-621.

(65) Guo, S.; Akhremitchev, B. B., Packing Density and Structural Heterogeneity of Insulin Amyloid Fibrils Measured by Afm Nanoindentation. *Biomacromolecules* **2006,** *7*, 1630-1636.

(66) Kol, N.; Adler-Abramovich, L.; Barlam, D.; Shneck, R. Z.; Gazit, E.; Rousso, I., Self-Assembled Peptide Nanotubes Are Uniquely Rigid Bioinspired Supramolecular Structures. *Nano Lett.* **2005,** *5*, 1343-1346.

(67) Williams, M. A., Protein–Ligand Interactions: Fundamentals. In *Protein-Ligand Interactions: Methods and Applications*, Williams, M. A.; Daviter, T., Eds. Humana Press: Totowa, NJ, 2013; pp 3-34.

(68) Savage, N., Proteomics: High-Protein Research. *Nature* **2015,** *527*, S6-S7.

(69) Ngaosuwan, K.; Lotero, E.; Suwannakarn, K.; Goodwin, J. G.; Praserthdam, P., Hydrolysis of Triglycerides Using Solid Acid Catalysts. *Ind. Eng. Chem. Res* **2009,** *48*, 4757-4767.

(70) Galante, Y. M.; Formantici, C., Enzyme Applications in Detergency and in Manufacturing Industries. *Curr. Org. Chem.* **2003,** *7*, 1399-1422.

(71) Radzicka, A.; Wolfenden, R., Rates of Uncatalyzed Peptide Bond Hydrolysis in Neutral Solution and the Transition State Affinities of Proteases. *J. Am. Chem. Soc.* **1996,** *118*, 6105-6109.

(72) Stroobants, K.; Absillis, G.; Moelants, E.; Proost, P.; Parac-Vogt, T. N., Regioselective Hydrolysis of Human Serum Albumin by Zriv-Substituted Polyoxotungstates at the Interface of Positively Charged Protein Surface Patches and Negatively Charged Amino Acid Residues. *Chem. Eur. J.* **2014,** *20*, 3894-3897.

(73) Sutmann, G., *Classical Molecular Dynamics* John von Neumann Institute for Computing, Julich, 2002; Vol. 10.

(74) Dill, K.; Bromberg, S.; Stigter, D., *Molecular Driving Forces*. Garland Science: New York, 2003.

(75) Kahl, G.; Kambayashi, S., A Molecular-Dynamics Study of the Dynamic Properties of Liquid Rubidium. I. Collective Correlation Functions. *J. Phys. Condens. Matter* **1994,** *6*, 10897.

(76) Heyes, D. M., Physical Properties of Liquid Water by Molecular Dynamics Simulations. *J. Chem. Soc. Faraday Trans.* **1994,** *90*, 3039-3049.

(77) Koishi, T.; Fujikawa, S., Static and Dynamic Properties of Ionic Liquids. *Mol Simul.* **2010,** *36*, 1237-1242.

(78) Todorova, T.; Seitsonen, A. P.; Hutter, J.; Kuo, I. F. W.; Mundy, C. J., Molecular Dynamics Simulation of Liquid Water: Hybrid Density Functionals. *J. Phys. Chem. B* **2006,** *110*, 3685-3691.

(79) Hanchen, H.; Ghoniem, N. M.; Wong, J. K.; Baskes, M., Molecular Dynamics Determination of Defect Energetics in Beta -Sic Using Three Representative Empirical Potentials. *Model. Simul. Mater. Sci. Eng.* **1995,** *3*, 615.

(80) Lazarev, N. P.; Dubinko, V. I., Molecular Dynamics Simulation of Defects Production in the Vicinity of Voids. *Radiat Eff. Def. Sol.* **2003,** *158*, 803-810.

(81) Chu, C.-J.; Chen, T.-C., Surface Properties of Film Deposition Using Molecular Dynamics Simulation. *Surf. Coat. Tech.* **2006,** *201*, 1796-1804.

(82) El-Bayyari, Z.; Erkoç, Ş., Bulk and Surface Properties of Aluminum: A Molecular-Dynamics Simulation. *Mater. Chem. Phys.* **1994,** *37*, 382-388.

(83) Lü, Y.; Wei, B., A Molecular Dynamics Study on Surface Properties of Supercooled Water. *Sci. China Phys. Mech. Astro.* **2006,** *49*, 616-625.

(84) Prathab, B.; Aminabhavi, T. M., Atomistic Simulations to Compute Surface Properties of Poly(N-Vinyl-2-Pyrrolidone) (Pvp) and Blends of Pvp/Chitosan. *Langmuir* **2007,** *23*, 5439-5444.

(85) Sanz-Navarro, C. F.; Åstrand, P.-O.; Chen, D.; Rønning, M.; van Duin, A. C. T.; Goddard, W. A., Molecular Dynamics Simulations of Metal Clusters Supported on Fishbone Carbon Nanofibers. *J. Phys. Chem. C* **2010,** *114*, 3522-3530.

(86) Salonen, M.; Napari, I.; Vehkamäki, H., Molecular Dynamics Simulation of Atomic Clusters in Equilibrium with a Vapour. *Mol Simul.* **2007,** *33*, 245-251.

(87) Abeyrathne, C. D.; Halgamuge, M. N.; Farrell, P. M.; Skafidas, E., Dielectric Properties of Liquid Phase Molecular Clusters Using the External Field Method: Molecular Dynamics Study. *PCCP* **2014,** *16*, 13943-13947.

(88) Carrillo, J.-M. Y.; Dobrynin, A. V., Polyelectrolytes in Salt Solutions: Molecular Dynamics Simulations. *Macromolecules* **2011,** *44*, 5798-5816.

(89) Liao, Q.; Dobrynin, A. V.; Rubinstein, M., Molecular Dynamics Simulations of Polyelectrolyte Solutions: Nonuniform Stretching of Chains and Scaling Behavior. *Macromolecules* **2003,** *36*, 3386-3398.

(90) Sofronova, A. A.; Evstafyeva, D. B.; Izumrudov, V. A.; Muronetz, V. I.; Semenyuk, P. I., Protein-Polyelectrolyte Complexes: Molecular Dynamics Simulations and Experimental Study. *Polymer* **2017,** *113*, 39-45.

(91) He, G.-L.; Merlitz, H.; Sommer, J.-U., Molecular Dynamics Simulations of Polyelectrolyte Brushes under Poor Solvent Conditions: Origins of Bundle Formation. *J. Chem. Phys.* **2014,** *140*, 104911.

(92) Karplus, M.; McCammon, J. A., Molecular Dynamics Simulations of Biomolecules. *Nat. Struct. Mol. Biol.* **2002,** *9*, 646.

(93) Karplus, M., Molecular Dynamics Simulations of Biomolecules. *Acc. Chem. Res.* **2002,** *35*, 321-323.

(94) Karplus, M.; Kuriyan, J., Molecular Dynamics and Protein Function. *PNAS* **2005,** *102*, 6679-6685.

(95) Beck, D. A. C.; Daggett, V., Methods for Molecular Dynamics Simulations of Protein Folding/Unfolding in Solution. *Methods* **2004,** *34*, 112-120.

(96) Childers, M. C.; Daggett, V., Insights from Molecular Dynamics Simulations for Computational Protein Design. *Mol. Sys. Des. & Eng.* **2017,** *2*, 9-33.

(97) Paul, T. J.; Schenk, G.; Prabhakar, R., Formation of Catalytically Active Binuclear Center of Glycerophosphodiesterase: A Molecular Dynamics Study. *J. Phys. Chem. B* **2018**.

(98) Paul, T. J.; Hoffmann, Z.; Wang, C.; Shanmugasundaram, M.; DeJoannis, J.; Shekhtman, A.; Lednev, I. K.; Yadavalli, V. K.; Prabhakar, R., Structural and Mechanical Properties of Amyloid Beta Fibrils: A Combined Experimental and Theoretical Approach. *J. Phys. Chem. Lett.* **2016,** *7*, 2758-2764.

(99) Libardo, M. D. J.; Paul, T. J.; Prabhakar, R.; Angeles-Boza, A. M., Hybrid Peptide Atcun-Sh-Buforin: Influence of the Atcun Charge And stereochemistry on Antimicrobial Activity. *Biochimie* **2015,** *113*, 143-155.

(100) Aliyan, A.; Paul, T. J.; Jiang, B.; Pennington, C.; Sharma, G.; Prabhakar, R.; Martí, A. A., Photochemical Identification of Molecular Binding Sites on the Surface of Amyloid-β Fibrillar Aggregates. *Chem* **2017,** *3*, 898-912.

(101) Paul, T. J.; Kelly, H.; Zuchniarz, J.; Ahmed, T.; Prabhakar, R., Design of Heparin Oligosaccharide Based Molecules for Inhibition of Alzheimer Amyloid Beta (Aβ40) Aggregation. *Can. J. Chem.* **2016,** *94*, 1090-1098.

(102) Case, D. A.; Cheatham, T. E.; Darden, T.; Gohlke, H.; Luo, R.; Merz, K. M.; Onufriev, A.; Simmerling, C.; Wang, B.; Woods, R., The Amber Biomolecular Simulation Programs. *J. Computat. Chem.* **2005,** *26*, 1668-1688.

(103) Case, D. A.; Babin, V.; Berryman, J. T.; Betz, R. M.; Cai, Q.; Cerutti, D. S.; Cheatham, T. E.; Darden, T. A.; Duke, R. E.; Gohlke, H., et al., *{Amber 14}*. 2014.

(104) Brooks, B. R.; Brooks, C. L.; MacKerell, A. D.; Nilsson, L.; Petrella, R. J.; Roux, B.; Won, Y.; Archontis, G.; Bartels, C.; Boresch, S., et al., Charmm: The Biomolecular Simulation Program. *J. Comput. Chem.* **2009,** *30*, 1545-1614.

(105) Phillips, J. C.; Braun, R.; Wang, W.; Gumbart, J.; Tajkhorshid, E.; Villa, E.; Chipot, C.; Skeel, R. D.; Kalé, L.; Schulten, K., Scalable Molecular Dynamics with Namd. *J. Comput. Chem.* **2005,** *26*, 1781-1802.

(106) Berendsen, H. J. C.; van der Spoel, D.; van Drunen, R., Gromacs: A Message-Passing Parallel Molecular Dynamics Implementation. *Comp. Phys. Comm.* **1995,** *91*, 43-56.

(107) Lindahl, E.; Hess, B.; van der Spoel, D., Gromacs 3.0: A Package for Molecular Simulation and Trajectory Analysis. *J. Mol. Model.* **2001,** *7*, 306-317.

(108) David, V. D. S.; Erik, L.; Berk, H.; Gerrit, G.; E., M. A.; C., B. H. J., Gromacs: Fast, Flexible, and Free. *J. Comput. Chem.* **2005,** *26*, 1701-1718.

(109) Hess, B.; Kutzner, C.; van der Spoel, D.; Lindahl, E., Gromacs 4: Algorithms for Highly Efficient, Load-Balanced, and Scalable Molecular Simulation. *J. Chem. Theory Comput.* **2008,** *4*, 435-447.

(110) Plimpton, S., Fast Parallel Algorithms for Short-Range Molecular Dynamics. *J Comput Phys.* **1995,** *117*, 1-19.

(111) Oostenbrink, C.; Villa, A.; Mark, A. E.; Van Gunsteren, W. F., A Biomolecular Force Field Based on the Free Enthalpy of Hydration and Solvation: The Gromos Force-Field Parameter Sets 53a5 and 53a6. *J. Comput. Chem.* **2004,** *25*, 1656-1676.

(112) Wang, J.; Wolf, R. M.; Caldwell, J. W.; Kollman, P. A.; Case, D. A., Development and Testing of a General Amber Force Field. *J. Comput. Chem.* **2004,** *25*, 1157-1174.

(113) Duan, Y.; Wu, C.; Chowdhury, S.; Lee, M. C.; Xiong, G.; Zhang, W.; Yang, R.; Cieplak, P.; Luo, R.; Lee, T., et al., A Point-Charge Force Field for Molecular Mechanics Simulations of Proteins Based on Condensed-Phase Quantum Mechanical Calculations. *J. Comput. Chem.* **2003,** *24*, 1999-2012.

(114) Lii, J. H.; Allinger, N. L., Molecular Mechanics. The Mm3 Force Field for Hydrocarbons. 3. The Van Der Waals' Potentials and Crystal Data for Aliphatic and Aromatic Hydrocarbons. *J. Am. Chem. Soc.* **1989,** *111*, 8576-8582.

(115) L., A. N.; Kuohsiang, C.; Jenn-Huei, L., An Improved Force Field (MM4) for Saturated Hydrocarbons. *J. Comput. Chem.* **1996,** *17*, 642-668.

(116) Ponder, J. W.; Case, D. A., Force Fields for Protein Simulations. *Adv. Prot. Chem* **2003,** *66*, 27-85.

(117) Jing, H.; D., M. A., Charmm36 All-Atom Additive Protein Force Field: Validation Based on Comparison to Nmr Data. *J. Comput. Chem.* **2013,** *34*, 2135-2145.

(118) Robertson, M. J.; Tirado-Rives, J.; Jorgensen, W. L., Improved Peptide and Protein Torsional Energetics with the Opls-Aa Force Field. *J. Chem. Theory Comput.* **2015,** *11*, 3499-3509.

(119) Goodsell, D. S.; Olson, A. J., Automated Docking of Substrates to Proteins by Simulated Annealing. *Proteins: Struct., Funct., Bioinf.* **1990,** *8*, 195-202.

(120) Ruth, H.; M., M. G.; J., O. A.; S., G. D., A Semiempirical Free Energy Force Field with Charge-Based Desolvation. *J. Comput. Chem.* **2007,** *28*, 1145-1152.

(121) D L Beveridge, a.; DiCapua, F. M., Free Energy Via Molecular Simulation: Applications to Chemical and Biomolecular Systems. *Ann. Rev. Biophy. Biomole. Struc.* **1989,** *18*, 431-492.

(122) Foloppe, N.; Hubbard, R., Towards Predictive Ligand Design with Free-Energy Based Computational Methods? *Curr. Med. Chem.* **2006,** *13*, 3583-3608.

(123) Kelly, C. P.; Cramer, C. J.; Truhlar, D. G., Aqueous Solvation Free Energies of Ions and Ion−Water Clusters Based on an Accurate Value for the Absolute Aqueous Solvation Free Energy of the Proton. *J. Phys. Chem. B* **2006,** *110*, 16066-16081.

(124) Ashbaugh, H. S.; Asthagiri, D., Single Ion Hydration Free Energies: A Consistent Comparison between Experiment and Classical Molecular Simulation. *J. Chem. Phys.* **2008,** *129*, 204501.

(125) Jorgensen, W. L.; Ravimohan, C., Monte Carlo Simulation of Differences in Free Energies of Hydration. *J. Chem. Phys.* **1985,** *83*, 3050-3054.

(126) Fleischman, S. H.; III, C. L. B., Thermodynamics of Aqueous Solvation: Solution Properties of Alcohols and Alkanes. *J. Chem. Phys.* **1987,** *87*, 3029-3037.

(127) Gilson, M. K.; Zhou, H.-X., Calculation of Protein-Ligand Binding Affinities. *Ann. Rev. Biophy. Biomole. Struc.* **2007,** *36*, 21-42.

(128) Knight, J. L.; Brooks, C. L., Λ-Dynamics Free Energy Simulation Methods. *J. Comput. Chem.* **2009,** *30*, 1692-1700.

(129) Brooks, C. L., Protein and Peptide Folding Explored with Molecular Simulations. *Acc. Chem. Res.* **2002,** *35*, 447-454.

(130) Jorgensen, W. L., The Many Roles of Computation in Drug Discovery. *Science* **2004,** *303*, 1813-1818.

(131) Jorgensen, W. L.; Ruiz-Caro, J.; Tirado-Rives, J.; Basavapathruni, A.; Anderson, K. S.; Hamilton, A. D., Computer-Aided Design of Non-Nucleoside Inhibitors of Hiv-1 Reverse Transcriptase. *Bioorg. & Med. Chem. Lett.* **2006,** *16*, 663-667.

(132) Knight, J. L.; Brooks, C. L., Λ-Dynamics Free Energy Simulation Methods. *Journal of Computational Chemistry* **2009,** *30*, 1692-1700.

(133) Kong, X.; III, C. L. B., Λ-Dynamics: A New Approach to Free Energy Calculations. *J. Chem. Phys.* **1996,** *105*, 2414-2423.

(134) Guo, Z.; Brooks, C. L.; Kong, X., Efficient and Flexible Algorithm for Free Energy Calculations Using the Λ-Dynamics Approach. *J. Phys. Chem. B* **1998,** *102*, 2032-2036.

(135) Martín, M. E.; Aguilar, M. A.; Chalmet, S.; Ruiz-López, M. F., An Iterative Procedure to Determine Lennard-Jones Parameters for Their Use in Quantum Mechanics/Molecular Mechanics Liquid State Simulations. *Chem. Phys.* **2002,** *284*, 607-614.

(136) Freindorf, M.; Gao, J., Optimization of the Lennard-Jones Parameters for a Combined Ab Initio Quantum Mechanical and Molecular Mechanical Potential Using the 3-21g Basis Set. *J. Comput. Chem.* **1996,** *17*, 386-395.

(137) Hay, P. J.; Wadt, W. R., Ab Initio Effective Core Potentials for Molecular Calculations. Potentials for the Transition Metal Atoms Sc to Hg. *J. Chem. Phys.* **1985,** *82*, 270-283.

(138) Frisch, M. J.; Trucks, G. W.; Schlegel, H. B.; Scuseria, G. E.; Robb, M. A.; Cheeseman, J. R.; Scalmani, G.; Barone, V.; Mennucci, B.; Petersson, G. A., et al. *Gaussian 09*, Gaussian, Inc.: Wallingford, CT, USA, 2009.

(139) Wang, J.; Wang, W.; Kollman, P. A.; Case, D. A., Automatic Atom Type and Bond Type Perception in Molecular Mechanical Calculations. *J Mol Graph Model.* **2006,** *25*, 247-260.

(140) Wang, J.; Wolf, R. M.; Caldwell, J. W.; Kollman, P. A.; Case, D. A., Development and Testing of a General Amber Force Field. *Journal of Computational Chemistry* **2004,** *25*, 1157-1174.

(141) Case, D. A.; Betz, R. M.; Botello-Smith, W.; Cerutti, D. S.; Cheatham, T. E.; Darden, T. A.; Duke, R. E.; Giese, T. J.; Gohlke, H.; Goetz, A. W., et al. *Amber*, University of California, San Francisco: 2016.

(142) Leroy, F.; Miró, P.; Poblet, J. M.; Bo, C.; Bonet Ávalos, J., Keggin Polyoxoanions in Aqueous Solution: Ion Pairing and Its Effect on Dynamic Properties by Molecular Dynamics Simulations. *J. Phys. Chem. B* **2008,** *112*, 8591-8599.

(143) López, X.; Nieto-Draghi, C.; Bo, C.; Avalos, J. B.; Poblet, J. M., Polyoxometalates in Solution: Molecular Dynamics Simulations on the A-Pw12o403- Keggin Anion in Aqueous Media. *J. Phys. Chem. A* **2005,** *109*, 1216-1222.

(144) Rappe, A. K.; Casewit, C. J.; Colwell, K. S.; Goddard, W. A.; Skiff, W. M., Uff, a Full Periodic Table Force Field for Molecular Mechanics and Molecular Dynamics Simulations. *J. Am. Chem. Soc.* **1992,** *114*, 10024-10035.

(145) Nurcombe, V.; Ford, M.; Wildschut, J., Developmental Regulation of Neural Response to Fgf-1 and Fgf-2 by Heparan Sulfate Proteoglycan. **1993**, 103-106.

(146) Derrick, J. S.; Kerr, R. A.; Korshavn, K. J.; McLane, M. J.; Kang, J.; Nam, E.; Ramamoorthy, A.; Ruotolo, B. T.; Lim, M. H., Importance of the Dimethylamino Functionality on a Multifunctional Framework for Regulating Metals, Amyloid-B, and Oxidative Stress in Alzheimer’s Disease. *Inorg. Chem.* **2016,** *55*, 5000-5013.

(147) Beck, M. W.; Oh, S. B.; Kerr, R. A.; Lee, H. J.; Kim, S. H.; Kim, S.; Jang, M.; Ruotolo, B. T.; Lee, J.-Y.; Lim, M. H., A Rationally Designed Small Molecule for Identifying an in Vivo Link between Metal-Amyloid-[Small Beta] Complexes and the Pathogenesis of Alzheimer's Disease. *Chem. Sci.* **2015,** *6*, 1879-1886.

(148) Salmon, A. J.; Williams, M. L.; Hofmann, A.; Poulsen, S.-A., Protein Crystal Structures with Ferrocene and Ruthenocene-Based Enzyme Inhibitors. *Chem. Comm.* **2012,** *48*, 2328-2330.

(149) Temperini, C.; Cecchi, A.; Scozzafava, A.; Supuran, C. T., Carbonic Anhydrase Inhibitors. Interaction of Indapamide and Related Diuretics with 12 Mammalian Isozymes and X-Ray Crystallographic Studies for the Indapamide–Isozyme Ii Adduct. *Bioorg. & Med. Chem. Lett.* **2008,** *18*, 2567-2573.

(150) Colletier, J.-P.; Laganowsky, A.; Landau, M.; Zhao, M.; Soriaga, A. B.; Goldschmidt, L.; Flot, D.; Cascio, D.; Sawaya, M. R.; Eisenberg, D., Molecular Basis for Amyloid-B Polymorphism. *PNAS* **2011,** *108*, 16938-16943.

(151) Landau, M.; Sawaya, M. R.; Faull, K. F.; Laganowsky, A.; Jiang, L.; Sievers, S. A.; Liu, J.; Barrio, J. R.; Eisenberg, D., Towards a Pharmacophore for Amyloid. *PLoS Biol.* **2011,** *9*, e1001080.

(152) Sawaya, M. R.; Sambashivan, S.; Nelson, R.; Ivanova, M. I.; Sievers, S. A.; Apostol, M. I.; Thompson, M. J.; Balbirnie, M.; Wiltzius, J. J. W.; McFarlane, H. T., et al., Atomic Structures of Amyloid Cross-B Spines Reveal Varied Steric Zippers. *Nature* **2007,** *447*, 453.

(153) Nelson, R.; Sawaya, M. R.; Balbirnie, M.; Madsen, A. Ø.; Riekel, C.; Grothe, R.; Eisenberg, D., Structure of the Cross-B Spine of Amyloid-Like Fibrils. *Nature* **2005,** *435*, 773.

(154) Lin, J.-H.; Perryman, A. L.; Schames, J. R.; McCammon, J. A., Computational Drug Design Accommodating Receptor Flexibility: The Relaxed Complex Scheme. *J. Am. Chem. Soc.* **2002,** *124*, 5632-5633.

(155) Gorfe, A. A.; Caflisch, A., Functional Plasticity in the Substrate Binding Site of B-Secretase. *Structure* **2005,** *13*, 1487-1498.

(156) Mangoni, M.; Roccatano, D.; Di Nola, A., Docking of Flexible Ligands to Flexible Receptors in Solution by Molecular Dynamics Simulation. *Proteins: Struct., Funct., Bioinf.* **1999,** *35*, 153-162.

(157) Case, D. A., Cheatham, III, T.E., Darden, T., Gohlke, H., Luo, R., Merz, Jr., K.M., Onufriev, A., Simmerling, C., Wang, B. Woods, R. , The Amber Biomolecular Simulation Programs. *J. Comput. Chem.* **2005,** *26*, 1668-1688.

(158) Chapagain, P. P.; Regmi, C. K.; Castillo, W., Fluorescent Protein Barrel Fluctuations and Oxygen Diffusion Pathways in Mcherry. *J. Chem. Phys.* **2011,** *135*, 235101.

(159) Petkova, A. T., Ishii, Y., Balbach, J. J., Antzutkin N. O., Leapman, R. D., Delaglio, F., and Tycko, R., A Structural Model for Alzheimer's B-Amyloid Fibrils Based on Experimental Constrains from Solid State Nmr. *Pro. Natl. Acad. Sci. USA* **2002,** *99*, 16742-16747.

(160) Colvin, M. T.; Silvers, R.; Ni, Q. Z.; Can, T. V.; Sergeyev, I.; Rosay, M.; Donovan, K. J.; Michael, B.; Wall, J.; Linse, S., et al., Atomic Resolution Structure of Monomorphic Aβ42 Amyloid Fibrils. *J. Am. Chem. Soc.* **2016,** *138*, 9663-9674.

(161) Mingyan, D.; J., P. T.; Zachary, H.; Kwaichow, C.; Dingkun, H.; Hongqi, A.; Rajeev, P., Structural and Material Properties of Amyloid Aβ40/42 Fibrils. *ChemPhysChem* **2016,** *17*, 2558-2566.

(162) Krieger, E.; Vriend, G., Models@Home: Distributed Computing in Bioinformatics Using a Screensaver Based Approach. *Bioinformatics* **2002,** *18*, 315-318.

(163) Eisenberg, D.; Jucker, M., The Amyloid State of Proteins in Human Diseases. *Cell* **2012,** *148*, 1188-1203.

(164) Shashilov, V. A.; Sikirzhytski, V.; Popova, L. A.; Lednev, I. K., Quantitative Methods for Structural Characterization of Proteins Based on Deep Uv Resonance Raman Spectroscopy. *Methods* **2010,** *52*, 23-37.

(165) Lednev, I. K., Vibrational Spectroscopy: Biological Applications of Ultraviolet Raman Spectroscopy. In *Protein Structures, Methods in Protein Structures and Stability Analysis*, Uversky, V. N.; Permyakov, E. A., Eds. Nova Science Publishers, Inc.: New York, 2007

(166) Paravastu, A. K.; Leapman, R. D.; Yau, W.-M.; Tycko, R., Molecular Structural Basis for Polymorphism in Alzheimer's Β-Amyloid Fibrils. *PNAS* **2008,** *105*, 18349-18354.

(167) Xiao, Y.; Ma, B.; McElheny, D.; Parthasarathy, S.; Long, F.; Hoshi, M.; Nussinov, R.; Ishii, Y., Aβ(1–42) Fibril Structure Illuminates Self-Recognition and Replication of Amyloid in Alzheimer'S Disease. *Nat. Struct. Mol. Biol* **2015,** *22*, 499.

(168) Adamcik, J.; Lara, C.; Usov, I.; Jeong, J. S.; Ruggeri, F. S.; Dietler, G.; Lashuel, H. A.; Hamley, I. W.; Mezzenga, R., Measurement of Intrinsic Properties of Amyloid Fibrils by the Peak Force Qnm Method. *Nanoscale* **2012,** *4*, 4426-4429.

(169) Adamcik, J.; Jung, J.-M.; Flakowski, J.; De Los Rios, P.; Dietler, G.; Mezzenga, R., Understanding Amyloid Aggregation by Statistical Analysis of Atomic Force Microscopy Images. *Nat. Nano.* **2010,** *5*, 423-428.

(170) Adamcik, J.; Berquand, A.; Mezzenga, R., Single-Step Direct Measurement of Amyloid Fibrils Stiffness by Peak Force Quantitative Nanomechanical Atomic Force Microscopy. *App. Phys. Lett.* **2011,** *98*, 193701.

(171) Adamcik, J.; Mezzenga, R., Adjustable Twisting Periodic Pitch of Amyloid Fibrils. *Soft Matt.* **2011,** *7*, 5437-5443.

(172) Paparcone, R.; Sanchez, J.; Buehler, M. J., Comparative Study of Polymorphous Alzheimer's a Beta(1-40) Amyloid Nanofibrils and Microfibers. *J. Comput. Theor. Nanosci.* **2010,** *7*, 1279-1286.

(173) Florová, P.; Sklenovský, P.; Banáš, P.; Otyepka, M., Explicit Water Models Affect the Specific Solvation and Dynamics of Unfolded Peptides While the Conformational Behavior and Flexibility of Folded Peptides Remain Intact. *J. Chem. Theory Comput.* **2010,** *6*, 3569-3579.

(174) Accelrys *Materials Studio Accelrys*, 7.0; 2001-2011.

(175) Sun, H., Compass: An Ab Initio Force-Field Optimized for Condensed-Phase Applicationsoverview with Details on Alkane and Benzene Compounds. *J. Phys. Chem. B* **1998,** *102*, 7338-7364.

(176) Choi, B.; Yoon, G.; Lee, S. W.; Eom, K., Mechanical Deformation Mechanisms and Properties of Amyloid Fibrils. *PCCP* **2015,** *17*, 1379-1389.

(177) Paparcone, R.; Buehler, M. J., Failure of a Beta(1-40) Amyloid Fibrils under Tensile Loading. *Biomaterials* **2011,** *32*, 3367-3374.

(178) Hadler, K. S.; Mitić, N.; Ely, F.; Hanson, G. R.; Gahan, L. R.; Larrabee, J. A.; Ollis, D. L.; Schenk, G., Structural Flexibility Enhances the Reactivity of the Bioremediator Glycerophosphodiesterase by Fine-Tuning Its Mechanism of Hydrolysis. *J. Am. Chem. Soc.* **2009,** *131*, 11900-11908.

(179) Hadler, K. S.; Tanifum, E. A.; Yip, S. H.-C.; Mitić, N.; Guddat, L. W.; Jackson, C. J.; Gahan, L. R.; Nguyen, K.; Carr, P. D.; Ollis, D. L., et al., Substrate-Promoted Formation of a Catalytically Competent Binuclear Center and Regulation of Reactivity in a Glycerophosphodiesterase from Enterobacter Aerogenes. *J. Am. Chem. Soc.* **2008,** *130*, 14129-14138.

(180) Pedroso, M. M.; Ely, F.; Carpenter, M. C.; Mitić, N.; Gahan, L. R.; Ollis, D. L.; Wilcox, D. E.; Schenk, G., Mechanistic Insight from Calorimetric Measurements of the Assembly of the Binuclear Metal Active Site of Glycerophosphodiesterase (Gpdq) from Enterobacter Aerogenes. *Biochemistry* **2017,** *56*, 3328-3336.

(181) Hadler, K. S.; Gahan, L. R.; Ollis, D. L.; Schenk, G., The Bioremediator Glycerophosphodiesterase Employs a Non-Processive Mechanism for Hydrolysis. *J. Inorg. Biochem.* **2010,** *104*, 211-213.

(182) Mitić, N.; Hadler, K. S.; Gahan, L. R.; Hengge, A. C.; Schenk, G., The Divalent Metal Ion in the Active Site of Uteroferrin Modulates Substrate Binding and Catalysis. *J. Am. Chem. Soc.* **2010,** *132*, 7049-7054.

(183) Aubert, S. D.; Li, Y.; Raushel, F. M., Mechanism for the Hydrolysis of Organophosphates by the Bacterial Phosphotriesterase. *Biochemistry* **2004,** *43*, 5707-5715.

(184) Ely, F.; Hadler, Kieran S.; Gahan, Lawrence R.; Guddat, Luke W.; Ollis, David L.; Schenk, G., The Organophosphate-Degrading Enzyme from <Em>Agrobacterium Radiobacter</Em> Displays Mechanistic Flexibility for Catalysis. *Biochem. J* **2010,** *432*, 565-573.

(185) Selleck, C.; Larrabee, J. A.; Harmer, J.; Guddat, L. W.; Mitić, N.; Helweh, W.; Ollis, D. L.; Craig, W. R.; Tierney, D. L.; Monteiro Pedroso, M., et al., Aim-1: An Antibiotic-Degrading Metallohydrolase That Displays Mechanistic Flexibility. *Chem. Eur. J.* **2016,** *22*, 17704-17714.

(186) Hadler, K. S.; Mitić, N.; Yip, S. H.-C.; Gahan, L. R.; Ollis, D. L.; Schenk, G.; Larrabee, J. A., Electronic Structure Analysis of the Dinuclear Metal Center in the Bioremediator Glycerophosphodiesterase (Gpdq) from Enterobacter Aerogenes. *Inorg. Chem.* **2010,** *49*, 2727-2734.

(187) Daumann, L. J.; McCarthy, B. Y.; Hadler, K. S.; Murray, T. P.; Gahan, L. R.; Larrabee, J. A.; Ollis, D. L.; Schenk, G., Promiscuity Comes at a Price: Catalytic Versatility Vs Efficiency in Different Metal Ion Derivatives of the Potential Bioremediator Gpdq. *Biochim. Biophys. Acta, Proteins Proteomics* **2013,** *1834*, 425-432.

(188) Stroobants, K.; Absillis, G.; Moelants, E.; Proost, P.; Parac-Vogt, T. N., Regioselective Hydrolysis of Human Serum Albumin by Zriv-Substituted Polyoxotungstates at the Interface of Positively Charged Protein Surface Patches and Negatively Charged Amino Acid Residues. *Chem. - Eur. J.* **2014,** *20*, 3894-3897.

(189) Proust, A.; Thouvenot, R.; Gouzerh, P., Functionalization of Polyoxometalates: Towards Advanced Applications in Catalysis and Materials Science. *Chem. Commun.* **2008**, 1837-1852.

(190) Long, D.-L.; Tsunashima, R.; Cronin, L., Polyoxometalates: Building Blocks for Functional Nanoscale Systems. *Angew. Chem., Int. Ed.* **2010,** *49*, 1736-1758.

(191) Pope, M., *Heteropoly and Isopoly Oxometalates*. 1 ed.; Springer: Verlag Berlin Heidelberg, 1983.

(192) Pope, M. T.; Müller, A., Polyoxometalate Chemistry: An Old Field with New Dimensions in Several Disciplines. *Angew. Chem., Int. Ed.* **1991,** *30*, 34-48.

(193) Bard, A.; Stratmann, M.; Scholz, F.; Pickett, C., *Electrochemistry of Isopoly and Heteropoly Oxometalates*. Wiley: In Encyclopedia of Electrochemistry, 2006; Vol. 7.

(194) Baker, L. C. W.; Glick, D. C., Present General Status of Understanding of Heteropoly Electrolytes and a Tracing of Some Major Highlights in the History of Their Elucidation. *Chem. Rev.* **1998,** *98*, 3-50.

(195) Kozhevnikov, I. V., Catalysis by Heteropoly Acids and Multicomponent Polyoxometalates in Liquid-Phase Reactions. *Chem. Rev.* **1998,** *98*, 171-198.

(196) Zhang, G.; Yang, W.; Yao, J., Thermally Enhanced Visible-Light Photochromism of Phosphomolybdic Acid–Polyvinylpyrrolidone Hybrid Films. *Adv. Funct. Mat.* **2005,** *15*, 1255-1259.

(197) Zhang, G.; Chen, Z.; He, T.; Ke, H.; Ma, Y.; Shao, K.; Yang, W.; Yao, J., Construction of Self-Assembled Ultrathin Polyoxometalate/1,10-Decanediamine Photochromic Films. *J. Phys. Chem. B* **2004,** *108*, 6944-6948.

(198) Yamase, T., Photo- and Electrochromism of Polyoxometalates and Related Materials. *Chem. Rev.* **1998,** *98*, 307-326.

(199) Judd, D. A.; Nettles, J. H.; Nevins, N.; Snyder, J. P.; Liotta, D. C.; Tang, J.; Ermolieff, J.; Schinazi, R. F.; Hill, C. L., Polyoxometalate Hiv-1 Protease Inhibitors. A New Mode of Protease Inhibition. *J. Am. Chem. Soc.* **2001,** *123*, 886-897.

(200) Müller, C. E.; Iqbal, J.; Baqi, Y.; Zimmermann, H.; Röllich, A.; Stephan, H., Polyoxometalates—a New Class of Potent Ecto-Nucleoside Triphosphate Diphosphohydrolase (Ntpdase) Inhibitors. *Bioorg. & Med. Chem. Lett.* **2006,** *16*, 5943-5947.

(201) Sansom, F. M.; Riedmaier, P.; Newton, H. J.; Dunstone, M. A.; Müller, C. E.; Stephan, H.; Byres, E.; Beddoe, T.; Rossjohn, J.; Cowan, P. J., et al., Enzymatic Properties of an Ecto-Nucleoside Triphosphate Diphosphohydrolase from Legionella Pneumophila: Substrate Specificity and Requirement for Virulence. *J. Biol. Chem.* **2008,** *283*, 12909-12918.

(202) Zhang, Z.-M.; Duan, X.; Yao, S.; Wang, Z.; Lin, Z.; Li, Y.-G.; Long, L.-S.; Wang, E.-B.; Lin, W., Cation-Mediated Optical Resolution and Anticancer Activity of Chiral Polyoxometalates Built from Entirely Achiral Building Blocks. *Chem. Sci.* **2016,** *7*, 4220-4229.

(203) Janell, D.; Tocilj, A.; Koelin, I.; Schluenzen, F.; Gluehmann, M.; Hansen, H. A. S.; Harms, J.; Bashan, A.; Agmon, I.; Bartels, H., et al., *Polyoxometalate Chemistry*. Kluwer Academic Publishers: 2001.

(204) Sarafianos, S. G.; Kortz, U.; Pope, M. T.; Modak, M. J., Mechanism of Polyoxometalate-Mediated Inactivation of DNA Polymerases: An Analysis with Hiv-1 Reverse Transcriptase Indicates Specificity for the DNA-Binding Cleft. *Biochem. J* **1996,** *319*, 619-626.

(205) Stroobants, K.; Goovaerts, V.; Absillis, G.; Bruylants, G.; Moelants, E.; Proost, P.; Parac-Vogt, T. N., Molecular Origin of the Hydrolytic Activity and Fixed Regioselectivity of a Zriv-Substituted Polyoxotungstate as Artificial Protease. *Chem. - Eur. J.* **2014,** *20*, 9567-9577.

(206) Stroobants, K.; Moelants, E.; Ly, H. G. T.; Proost, P.; Bartik, K.; Parac-Vogt, T. N., Polyoxometalates as a Novel Class of Artificial Proteases: Selective Hydrolysis of Lysozyme under Physiological Ph and Temperature Promoted by a Cerium(Iv) Keggin-Type Polyoxometalate. *Chem. - Eur. J.* **2013,** *19*, 2848-2858.

(207) Geng, J.; Li, M.; Ren, J.; Wang, E.; Qu, X., Polyoxometalates as Inhibitors of the Aggregation of Amyloid Β Peptides Associated with Alzheimer's Disease. *Angew. Chem., Int. Ed.* **2011,** *50*, 4184-4188.

(208) Pu, F.; Wang, E.; Jiang, H.; Ren, J., Identification of Polyoxometalates as Inhibitors of Basic Fibroblast Growth Factor. *Mol. BioSyst.* **2013,** *9*, 113-120.

(209) Solé-Daura, A.; Goovaerts, V.; Stroobants, K.; Absillis, G.; Jiménez-Lozano, P.; Poblet, J. M.; Hirst, J. D.; Parac-Vogt, T. N.; Carbó, J. J., Probing Polyoxometalate–Protein Interactions Using Molecular Dynamics Simulations. *Chem. - Eur. J.* **2016,** *22*, 15280-15289.

(210) Zhang, T.; Li, H.-W.; Wu, Y.; Wang, Y.; Wu, L., The Two-Step Assemblies of Basic-Amino-Acid-Rich Peptide with a Highly Charged Polyoxometalate. *Chem. Eur. J.* **2015,** *21*, 9028-9033.

(211) Li, H.-W.; Wang, Y.; Zhang, T.; Wu, Y.; Wu, L., Selective Binding of Amino Acids on Europium-Substituted Polyoxometalates and the Interaction-Induced Luminescent Enhancement Effect. *ChemPlusChem* **2014,** *79*, 1208-1213.

(212) Zhou, Y.; Zheng, L.; Han, F.; Zhang, G.; Ma, Y.; Yao, J.; Keita, B.; de Oliveira, P.; Nadjo, L., Inhibition of Amyloid-Β Protein Fibrillization Upon Interaction with Polyoxometalates Nanoclusters. *Colloids Surf. A* **2011,** *375*, 97-101.

(213) Zhang, G.; Keita, B.; Craescu, C. T.; Miron, S.; de Oliveira, P.; Nadjo, L., Polyoxometalate Binding to Human Serum Albumin: A Thermodynamic and Spectroscopic Approach. *J. Phys. Chem. B* **2007,** *111*, 11253-11259.

(214) Zhang, G.; Keita, B.; Brochon, J.-C.; de Oliveira, P.; Nadjo, L.; Craescu, C. T.; Miron, S., Molecular Interaction and Energy Transfer between Human Serum Albumin and Polyoxometalates. *J. Phys. Chem. B* **2007,** *111*, 1809-1814.

(215) Baroni, S.; Mattu, M.; Vannini, A.; Cipollone, R.; Aime, S.; Ascenzi, P.; Fasano, M., Effect of Ibuprofen and Warfarin on the Allosteric Properties of Haem–Human Serum Albumin. *Eur. J. Biochem.* **2001,** *268*, 6214-6220.

(216) di Masi, A.; Gullotta, F.; Bolli, A.; Fanali, G.; Fasano, M.; Ascenzi, P., Ibuprofen Binding to Secondary Sites Allosterically Modulates the Spectroscopic and Catalytic Properties of Human Serum Heme–Albumin. *FEBS J.* **2011,** *278*, 654-662.

(217) Fanali, G.; Cao, Y.; Ascenzi, P.; Trezza, V.; Rubino, T.; Parolaro, D.; Fasano, M., Binding of Δ9-Tetrahydrocannabinol and Diazepam to Human Serum Albumin. *IUBMB Life* **2011,** *63*, 446-451.

(218) Fasano, M.; Curry, S.; Terreno, E.; Galliano, M.; Fanali, G.; Narciso, P.; Notari, S.; Ascenzi, P., The Extraordinary Ligand Binding Properties of Human Serum Albumin. *IUBMB Life* **2005,** *57*, 787-796.

(219) Sudlow, G.; Birkett, D. J.; Wade, D. N., The Characterization of Two Specific Drug Binding Sites on Human Serum Albumin. *Mol. Pharmacol.* **1975,** *11*, 824-832.

(220) Sudlow, G.; Birkett, D. J.; Wade, D. N., Further Characterization of Specific Drug Binding Sites on Human Serum Albumin. *Mol. Pharmacol.* **1976,** *12*, 1052-1061.

(221) Kim, J. H.; Britten, J.; Chin, J., Kinetics and Mechanism of a Cobalt(Iii) Complex Catalyzed Hydration of Nitriles. *J. Am. Chem. Soc.* **1993,** *115*, 3618-3622.

(222) Chin, J.; Zou, X., Relationship between Effective Nucleophilic Catalysis in the Hydrolysis of Esters with Poor Leaving Groups and the Lifetime of the Tetrahedral Intermediate. *J. Am. Chem. Soc.* **1984,** *106*, 3687-3688.

(223) Chei, W.; Ju, H.; Suh, J., New Chelating Ligands for Co(Iii)-Based Peptide-Cleaving Catalysts Selective for Pathogenic Proteins of Amyloidoses. *J. Biol. Inorg. Chem.* **2011,** *16*, 511-519.

(224) Lipscomb, W. N.; Sträter, N., Recent Advances in Zinc Enzymology. *Chem. Rev.* **1996,** *96*, 2375-2434.

(225) Christianson, D. W.; Lipscomb, W. N., Carboxypeptidase A. *Acc. Chem. Res.* **1989,** *22*, 62-69.

(226) Coleman, F.; Hynes, M. J.; Erxleben, A., Gaiii Complexes as Models for the Miii Site of Purple Acid Phosphatase: Ligand Effects on the Hydrolytic Reactivity toward Bis(2,4-Dinitrophenyl) Phosphate. *Inorg. Chem.* **2010,** *49*, 6725-6733.

(227) Pearson, R. G., Hard and Soft Acids and Bases, Hsab, Part I. **1968,** *45*, 581-587.

(228) Pearson, R. G., *Chemical Hardness*. Wiley-VCH: 1997.

(229) Breslow, R., *Artifical Enzymes*. Wiley-VCH: New York, 2005.

(230) Suh, J., Model Studies of Metalloenzymes Involving Metal Ions as Lewis Acid Catalysts. *Acc. Chem. Res.* **1992,** *25*, 273-278.

(231) Burgess, J., *Metal Ions in Solution* Halsted Press (Wiley): New York, 1978.

(232) Singhal, A.; Toth, L. M.; Lin, J. S.; Affholter, K., Zirconium(Iv) Tetramer/Octamer Hydrolysis Equilibrium in Aqueous Hydrochloric Acid Solution. *J. Am. Chem. Soc.* **1996,** *118*, 11529-11534.

(233) Erxleben, A., Interaction of Molybdocene Dichloride with Cysteine-Containing Peptides: Coordination, Regioselective Hydrolysis, and Intramolecular Aminolysis. *Inorg. Chem.* **2005,** *44*, 1082-1094.

(234) Bertini, I., Luchinat, C., Rosi, M., Sgamellotti, A., and Tarantelli, F., Pka of Zinc-Bound Water and Nucleophilicity of Hydroxo-Containing Species. Ab Initio Calculations on Models for Zinc Enzymes. *Inorg. Chem.* **1990,** *29*, 1460-1463.

(235) Toyofumi, I.; Yuki, F.; Toshiji, T.; Yuzo, Y.; Hiroyuki, H., Thermodynamic and Kinetic Studies of Zinc(Ii)–Triamine Complexes as Models of Ca and Ap. *Bull. Chem. Soc. Jap.* **1996,** *69*, 1265-1274.

(236) Itoh, T.; Hisada, H.; Usui, Y.; Fujii, Y., Hydrolysis of Phosphate Esters Catalyzed by Copper(Ii)-Triamine Complexes. The Effect of Triamine Ligands on the Reactivity of the Copper(Ii) Catalysts. *Inorganica Chim. Acta* **1998,** *283*, 51-60.

(237) Koike, T.; Kimura, E., Roles of Zinc(Ii) Ion in Phosphatases. A Model Study with Zinc(Ii)-Macrocyclic Polyamine Complexes. *J. Am. Chem. Soc.* **1991,** *113*, 8935-8941.

(238) Bonfá, L.; Gatos, M.; Mancin, F.; Tecilla, P.; Tonellato, U., The Ligand Effect on the Hydrolytic Reactivity of Zn(Ii) Complexes toward Phosphate Diesters. *Inorg. Chem.* **2003,** *42*, 3943-3949.

(239) Ly, H. G. T.; Absillis, G.; Parac-Vogt, T. N., Influence of the Amino Acid Side Chain on Peptide Bond Hydrolysis Catalyzed by a Dimeric Zr(Iv)-Substituted Keggin Type Polyoxometalate. *New J. Chem.* **2016,** *40*, 976-984.

(240) Fjell, C. D.; Hiss, J. A.; Hancock, R. E. W.; Schneider, G., Designing Antimicrobial Peptides: Form Follows Function. *Nat Rev Drug Discov.* **2011,** *11*, 37.

(241) Brogden, N. K.; Mehalick, L.; Fischer, C. L.; Wertz, P. W.; Brogden, K. A., The Emerging Role of Peptides and Lipids as Antimicrobial Epidermal Barriers and Modulators of Local Inflammation. *Skin Pharmacol Physiol.* **2012,** *25*, 167-181.

(242) Zasloff, M., Magainins, a Class of Antimicrobial Peptides from Xenopus Skin: Isolation, Characterization of Two Active Forms, and Partial Cdna Sequence of a Precursor. *PNAS* **1987,** *84*, 5449-5453.

(243) Jin, Y.; Lewis, M. A.; Gokhale, N. H.; Long, E. C.; Cowan, J. A., Influence of Stereochemistry and Redox Potentials on the Single- and Double-Strand DNA Cleavage Efficiency of Cu(Ii)· and Ni(Ii)·Lys-Gly-His-Derived Atcun Metallopeptides. *J. Am. Chem. Soc.* **2007,** *129*, 8353-8361.

(244) Uyterhoeven, E. T.; Butler, C. H.; Ko, D.; Elmore, D. E., Investigating the Nucleic Acid Interactions and Antimicrobial Mechanism of Buforin Ii. *FEBS Lett.* **2008,** *582*, 1715-1718.